FACULTY OF ENGINEERING AND ARCHITECTURE

Modeling of the Dirichlet-to-Neumann Operator in the Time Domain

Robin Wydaeghe
Student number: 01601706

Supervisors: Prof. dr. ir. Dries Vande Ginste, Prof. dr. ir. Hendrik Rogier
Counsellors: Dr. ir. Martijn Huynen, Ir. Pieter Decleer, Ir. Dries Bosman, Ir. Emile Vanderstraeten

Master's dissertation submitted in order to obtain the academic degree of
Master of Science in Engineering Physics

Academic year 2020-2021

GHENT UNIVERSITY

FACULTY OF ENGINEERING AND ARCHITECTURE

Modeling of the Dirichlet-to-Neumann Operator in the Time Domain

Robin Wydaeghe
Student number: 01601706

Supervisors: Prof. dr. ir. Dries Vande Ginste, Prof. dr. ir. Hendrik Rogier
Counsellors: Dr. ir. Martijn Huynen, Ir. Pieter Decleer, Ir. Dries Bosman, Ir. Emile Vanderstraeten

Master's dissertation submitted in order to obtain the academic degree of
Master of Science in Engineering Physics

Academic year 2020-2021

GHENT UNIVERSITY

Preface

A friend recently asked me how it is like to write a master's dissertation with the Electromagnetics group of Ghent University. Typical students would enjoy replying to this question with the most sensational stories of things going wrong, most often wildly exaggerated. However, I most definitely did not answer in this fashion. I responded that the experience I had in the last academic year was one any thesis student could only dream of. The level of professionalism, competence and communication was simply impeccable, for which I am very grateful. Therefore, I would like to thank some individuals. First, my promotors Dries Vande Ginste and Hendrik Rogier, both of whom I have much respect for. Many of of the core ideas in this thesis were provided by them. I also sincerely thank all of my supervisors, in no particular order, Martijn Huynen, Pieter Decleer, Dries Bosman and Emile Vanderstraeten. They were always present in our biweekly meetings to give me highly valuable feedback on my work. The diligent proof reading of this thesis in multiple versions was of great use to me. Without my supervisors and promotors, this master's thesis would not nearly be what it is now. They teached me valuable skills needed in research and beyond, for example, in communication and organization. Special thanks go to Domenico Spina who did all the vector fitting, a hugely important piece of the puzzle in this work. Although we thought only one model was necessary, the research lead us to require more. He was always willing to grant us yet another model when the previous one did not work, and answered numerous questions with a high level of expertise. Finally, I would like to thank my mother, father, sister and my girlfriend for reminding me to take breaks from working. They made the last year much more enjoyable, especially with the COVID-19 lockdowns. Their moral support is invaluable.

Robin Wydaeghe, June 2021

Admission to Loan

Robin Wydaeghe, June 2021

Modeling of the Dirichlet-to-Neumann Operator in the Time Domain

by

Robin Wydaeghe

Master's Dissertation submitted to obtain the academic degree of
Master of Science in Engineering Physics

Academic year 2020–2021

Promoters: Dries Vande Ginste and Prof. dr. ir. Hendrik Rogier
Supervisors: dr. ir. Martijn Huynen, ir. Pieter Decleer, ir. Dries Bosman and ir. Emile Vanderstraeten

Faculty of Engineering and Architecture
Ghent University

Department of Information Technology
Chairman: Prof. dr. ir. Bart Dhoedt

Summary

In this master's thesis, vector fitting is used to convert fitted Dirichlet-to-Neumann operators to a State-Space (SS) model. Subsequently, the model is discretized and interfaced with the Finite-Difference Time-Domain (FDTD) method or Fully Collocated Implicit FDTD (FCI-FDTD) method. Hence, an alternative simulation is obtained that replaces the material in a region of space while preserving its response. This replacement circumvents the simulation of the skin effect. Therefore, broadband modeling of good conductors becomes possible, in theory without any drawbacks. This is important for, e.g., signal integrity and electromagnetic comptability applications, as it can be applied in the time domain. Voltage controlled surface currents are easily added to commercial electronic computer-aided design codes. Thus, designers can much more efficiently optimize and validate state-of-the-art ICs.

This idea is explored with three distinct implementations on a series connection of transmission lines with voltage controlled current sources. The first is for a lossless leapfrog situation computed with FDTD. The second is similar but lossy. The third is again lossless but computed with FCI-FDTD. Results show intricate patterns in the measure of stability as a result of machine precision errors. When stable, very good accuracies can be obtained. The new SS-FCI-FDTD is the most performant method both in terms of stability and accuracy.

Keywords

Differential surface admittance operator, vector fitting, macromodeling, skin effect, fully collocated implicit, time domain

Modeling of the Dirichlet-to-Neumann Operator in the Time Domain

Robin Wydaeghe

Supervisor(s): Martijn Huynen, Pieter Decleer, Dries Bosman, Emile Vanderstraeten, Hendrik Rogier and Dries Vande Ginste

Abstract— **In this master's thesis, Vector Fitting (VF) was used to convert fitted Dirichlet-to-Neumann (DtN) operators to a State-Space (SS) model. Subsequently, the model was discretized and interfaced with the Finite-Difference Time-Domain (FDTD) method or Fully Collocated Implicit FDTD (FCI-FDTD) method. Hence, an alternative simulation is obtained that replaces the material in a region of space while preserving its response. This replacement circumvents the simulation of the skin effect. Therefore, broadband modeling of good conductors becomes possible, in theory without any drawbacks. The idea was explored with three distinct implementations on a series connection of transmission lines with Voltage Controlled Current Sources (VCCSs). Results show intricate patterns in the measure of stability as a result of machine precision errors. When stable, very good accuracies can be obtained. The new SS-FCI-FDTD method performs particularly well.**

Keywords— **Differential surface admittance operator, vector fitting, macromodeling, skin effect, fully collocated implicit, time domain**

I. Introduction

THE demand for high-performance Integrated Circuits (ICs) is high as new technologies in 5G, Internet of Things (IoT) and the automotive industry emerge. Electronic Computer-Aided Design (ECAD) is crucial to validate and optimize new electrically small ICs at high frequencies. Designers are facing problems with simulating good conductors in the time domain for Signal Integrity (SI) and Electromagnetic Comptability (EMC) applications. A prominent challenge here is the skin effect, where current crowds to the surface of good conductors at high frequencies.

A large number of approaches have been proposed in literature to mitigate the skin effect. None of them simultaneously combine simplicity, versatility, reliability and accuracy. This thesis proposes a new idea, using the DtN operator [1] in combination with a VF macromodeling approach [2], [3], [4], [5], [6]. By implementing the operator on a series connection of transmission lines, a proof-of-concept is given to apply the operator in two and three dimensions.

This extended abstract is structured as follows. First, three distinct numerical implementations are given of the operator in Section II. Second, results and discussions of each implementation are given in Section III. Finally, we conclude our findings together with future work in Section IV. Note that the thesis first provides an additional chapter discussing some preliminaries, which are not given here.

R. Wydaeghe is with the Engineering Physics Department, Ghent University (UGent), Ghent, Belgium. E-mail: Robin.Wydaeghe@UGent.be .

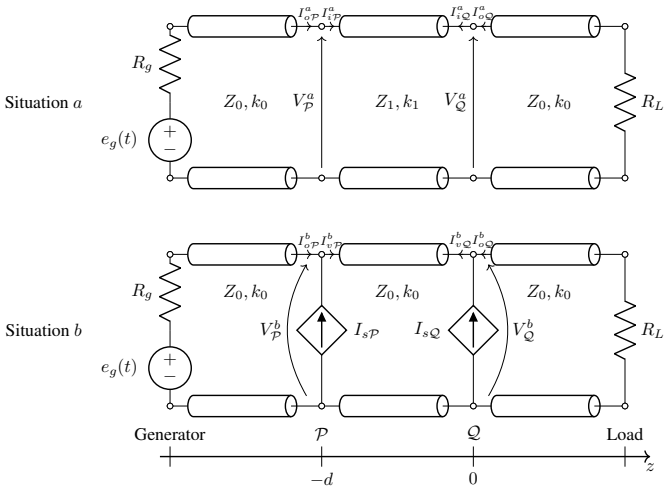

Fig. 1: *Situations* of the FET applied to three transmission lines. The subscript denotes inside (i), outside (o), virtual (v) or surface (s) fields in the FET. The central transmission line has length d.

II. Implementation of the DSA Operator on Transmission Lines

A. Introduction

Consider the series connection of three lossless transmission lines shown in Figure 1(a), named *situation* a. Only the central transmission line of situation a has different material parameters (subscript 1) compared to the surrounding transmission lines (subscript 0). Here, on the central line, the voltages and currents satisfy the general solution

$$\begin{aligned} \hat{v}^a(z) &= Ae^{-jk_1 z} + Be^{+jk_1 z}\,, \\ \hat{\imath}^a(z) &= \frac{1}{Z_1}\left(Ae^{-jk_1 z} - Be^{+jk_1 z}\right)\,. \end{aligned} \tag{1}$$

The voltage and current values on the nodes $\mathcal{P}$ and $\mathcal{Q}$ are

$$\begin{aligned} \hat{V}^a_{\mathcal{P}} &= \hat{v}^a(-d) = Ae^{+jk_1 d} + Be^{-jk_1 d}\,, \\ \hat{I}^a_{i\mathcal{P}} &= \hat{\imath}^a(-d) = \frac{1}{Z_1}\left(Ae^{+jk_1 d} - Be^{-jk_1 d}\right)\,, \\ \hat{V}^a_{\mathcal{Q}} &= \hat{v}^a(0) = A + B\,, \\ \hat{I}^a_{i\mathcal{Q}} &= -\hat{\imath}^a(0) = \frac{B - A}{Z_1}\,, \end{aligned} \tag{2}$$

taking into account the length d of this transmission line. As such, the relationship between current and voltage at the nodes

is given by:

$$\begin{bmatrix} \hat{I}^a_{i\mathcal{P}} \\ \hat{I}^a_{i\mathcal{Q}} \end{bmatrix} = \hat{\mathbf{Y}}^a \begin{bmatrix} \hat{V}^a_{\mathcal{P}} \\ \hat{V}^a_{\mathcal{Q}} \end{bmatrix} \quad \text{with} \quad \hat{\mathbf{Y}}^a = \tfrac{-j}{Z_1} \begin{bmatrix} \frac{1}{\tan k_1 d} & \frac{-1}{\sin k_1 d} \\ \frac{-1}{\sin k_1 d} & \frac{1}{\tan k_1 d} \end{bmatrix}. \tag{3}$$

Situation b is analogous except for the different material parameters of the central transmission line. The relationship between current and voltage is therefore given by:

$$\begin{bmatrix} \hat{I}^b_{v\mathcal{P}} \\ \hat{I}^b_{v\mathcal{Q}} \end{bmatrix} = \hat{\mathbf{Y}}^b \begin{bmatrix} \hat{V}^b_{\mathcal{P}} \\ \hat{V}^b_{\mathcal{P}} \end{bmatrix} \quad \text{with} \quad \hat{\mathbf{Y}}^b = \tfrac{-j}{Z_0} \begin{bmatrix} \frac{1}{\tan k_0 d} & \frac{-1}{\sin k_0 d} \\ \frac{-1}{\sin k_0 d} & \frac{1}{\tan k_0 d} \end{bmatrix}. \tag{4}$$

The Field Equivalence Theorem (FET) is applied to situation a to obtain situation b. This entails adding electric surface currents at the interfaces of the abstracted material. In circuit theory, this corresponds to two shunt VCCSs that feed into the interfacial nodes. Assuming identical voltages in situation a and b, we find

$$\begin{bmatrix} \hat{V}^a_{\mathcal{P}} \\ \hat{V}^a_{\mathcal{Q}} \end{bmatrix} = \begin{bmatrix} \hat{V}^b_{\mathcal{P}} \\ \hat{V}^b_{\mathcal{Q}} \end{bmatrix} \triangleq \begin{bmatrix} \hat{V}_{\mathcal{P}} \\ \hat{V}_{\mathcal{Q}} \end{bmatrix}. \tag{5}$$

Here we enforced the continuity of voltage across a node. The currents are also identical on the outside:

$$\begin{bmatrix} \hat{I}^a_{o\mathcal{P}} \\ \hat{I}^a_{o\mathcal{Q}} \end{bmatrix} = \begin{bmatrix} \hat{I}^b_{o\mathcal{P}} \\ \hat{I}^b_{o\mathcal{Q}} \end{bmatrix}. \tag{6}$$

For the currents in situation b we also apply KCL on the interfacial nodes:

$$\begin{bmatrix} \hat{I}_{s\mathcal{P}} \\ \hat{I}_{s\mathcal{Q}} \end{bmatrix} = \begin{bmatrix} \hat{I}^b_{v\mathcal{P}} \\ \hat{I}^b_{v\mathcal{Q}} \end{bmatrix} - \begin{bmatrix} \hat{I}^b_{o\mathcal{P}} \\ \hat{I}^b_{o\mathcal{Q}} \end{bmatrix}. \tag{7}$$

All the above conclusions yield an expression for the VCCSs:

$$\begin{aligned} \begin{bmatrix} \hat{I}_{s\mathcal{P}} \\ \hat{I}_{s\mathcal{Q}} \end{bmatrix} &= \hat{\mathbf{Y}}^b \begin{bmatrix} \hat{V}^b_{\mathcal{P}} \\ \hat{V}^b_{\mathcal{Q}} \end{bmatrix} - \hat{\mathbf{Y}}^a \begin{bmatrix} \hat{V}^a_{\mathcal{P}} \\ \hat{V}^a_{\mathcal{Q}} \end{bmatrix} \\ &= \left(\hat{\mathbf{Y}}^b - \hat{\mathbf{Y}}^a\right) \begin{bmatrix} \hat{V}_{\mathcal{P}} \\ \hat{V}_{\mathcal{Q}} \end{bmatrix} = \hat{\mathbf{Y}} \begin{bmatrix} \hat{V}_{\mathcal{P}} \\ \hat{V}_{\mathcal{Q}} \end{bmatrix}. \end{aligned} \tag{8}$$

With this procedure, identical currents are obtained in situation a and b on the left and right transmission lines. The discrete Differential Surface Admittance (DSA) operator[1] $\hat{\mathbf{Y}}$ is accurately macromodeled with VF:

$$\hat{\mathbf{Y}}(s) \approx \widetilde{\mathbf{Y}}(s) = \hat{\mathbf{R}}_0 + \sum_{i=1}^{N_p} \frac{\hat{\mathbf{R}}_i}{s - p_i}, \tag{9}$$

where passivity of the operator is enforced. From the poles and residues of (9), a SS representation

$$\frac{\mathrm{d}}{\mathrm{d}t}\boldsymbol{X}(t) = \mathbf{A}\boldsymbol{X}(t) + \mathbf{B}\boldsymbol{V}_s(t), \tag{10a}$$

$$\boldsymbol{I}_s(t) = \mathbf{C}\boldsymbol{X}(t) + \mathbf{D}\boldsymbol{V}_s(t), \tag{10b}$$

can be obtained where the input and output are given in the time domain. The voltages are found either by leapfrog FDTD or FCI-FDTD, but will also depend on the current sources it outputs.

[1] This operator is strongly related to the DtN operator.

B. Lossless Leapfrog

We see two ways to incorporate impressed VCCSs currents into a one-dimensional leapfrog FDTD scheme. The first is by attaching them on half-integer locations, i.e., where the currents are discretized. In this case, the surface voltages $\boldsymbol{V}_s(t)$ needs to be averaged over the interface. The second is by attaching them on integer locations, i.e., where the voltages are discretized. Here, no averaging is necessary. This constitutes a first free choice. The evaluation points of (10a) and (10b) can be different. Within the time interval of one FDTD iteration, this can be either on integer or half-integer time steps (m and $m+1/2$, respectively). This corresponds to another free choice. The time derivative appearing in (10a) can be discretized either throught the Backward Euler (BE) method or the Trapezoidal Rule (TR) method. This is the final free choice. Deriving a discretization of (10) cannot be done in general. Each combination of choices is derived in Appendix B. Sometimes, future voltages are necessary inside one iteration which is not directly available. However, by adding the VCCSs terms to the voltage update equation after the updating of the SS scheme, this can be achieved. The combined update scheme for one iteration is (in order)

$$\begin{aligned} I^{m+\frac{1}{2}}_{n+\frac{1}{2}} &= I^{m-\frac{1}{2}}_{n+\frac{1}{2}} + \alpha_{L,n+\frac{1}{2}} \left(V^m_n - V^m_{n+1}\right), \\ V^{m+1,\mathrm{yee}}_n &= V^m_n + \alpha_{C,n} \left(I^{m+\frac{1}{2}}_{n-\frac{1}{2}} - I^{m+\frac{1}{2}}_{n+\frac{1}{2}}\right), \\ \boldsymbol{V}^{m+1}_s &= \frac{1}{2}\left(C \begin{bmatrix} V^m_P \\ V^m_Q \end{bmatrix} + (2-C) \begin{bmatrix} V^m_{P-1} \\ V^m_{Q+1} \end{bmatrix}\right), \\ \boldsymbol{V}^{m+1,\mathrm{yee}}_s &= \frac{1}{2}\left(C \begin{bmatrix} V^{m+1,\mathrm{yee}}_P \\ V^{m+1,\mathrm{yee}}_Q \end{bmatrix} + (2-C) \begin{bmatrix} V^{m+1,\mathrm{yee}}_{P-1} \\ V^{m+1,\mathrm{yee}}_{Q+1} \end{bmatrix}\right), \\ \boldsymbol{X}^{\mathrm{new}} &= \mathbf{M}_{11}\boldsymbol{X}^{\mathrm{prev}} + \mathbf{M}_{12}\boldsymbol{I}^{m-\frac{1}{2}}_s + \mathbf{M}_{13}\boldsymbol{V}^m_s + \mathbf{M}_{14}\boldsymbol{V}^{m+1,\mathrm{yee}}_s, \\ \boldsymbol{I}^{m+\frac{1}{2}}_s &= \mathbf{M}_{21}\boldsymbol{X}^{\mathrm{prev}} + \mathbf{M}_{22}\boldsymbol{I}^{m-\frac{1}{2}}_s + \mathbf{M}_{23}\boldsymbol{V}^m_s + \mathbf{M}_{24}\boldsymbol{V}^{m+1,\mathrm{yee}}_s, \\ V^{m+1}_n &= V^{m+1,\mathrm{yee}}_n + \delta_{n,P}\alpha_{C,n} I^{m+\frac{1}{2}}_{s\mathcal{P}} + \delta_{n,Q}\alpha_{C,n} I^{m+\frac{1}{2}}_{s\mathcal{Q}}, \end{aligned} \tag{11}$$

where we used the notation

$$\begin{aligned} \alpha_{C,n} &\triangleq \frac{\Delta t}{C_n \Delta z}, \\ \alpha_{L,n+\frac{1}{2}} &\triangleq \frac{\Delta t}{L_{n+\frac{1}{2}} \Delta z}, \end{aligned} \tag{12}$$

with discretized per-unit-of-length parameters L and C. When the VCCSs' inputs are averaged over the interface, $C = 1$. When this is not the case, $C = 2$. The subscripts P and Q denote the integer positions where the material parameters first become those of the central transmission line. The $\mathbf{M}$ matrices denote in general terms an explicit update scheme for the SS. Update equations for the terminal networks have been left out for clarity.

C. Lossy Leapfrog

To ensure passivity of the SS model, the real part of the DSA operator should have strictly positive eigenvalues [5]. While this was guaranteed in the lossless case, Z_1 and k_1 are now complex, such that $\mathrm{Re}\{\widetilde{\mathbf{Y}}\}$ will not necessarily be zero. Fortunately, the problem can be solved. It is clear that the individual Surface

Admittance (SA) operators are passive as long as a physically passive medium is modeled. Each SA operator (3) and (4) can be individually Vector Fitted to a SS representation as in (10). Both SS models are computed independently from each other at each time step. They each model a current $\boldsymbol{i}_s^a(t)$ and $\boldsymbol{i}_s^b(t)$ for the SA operator of situation a and situation b, respectively. The final current is then given by

$$\boldsymbol{i}_s(t) = \boldsymbol{i}_s^b(t) - \boldsymbol{i}_s^a(t)\,. \tag{13}$$

However, this causes SS update equations (10) and (11) to fail when a VCCS current is required from the previous iteration. Therefore, only the evaluation points m and m can be used for the first and second equations, respectively. Furthermore, we also introduce *approximated schemes* based on the approximation

$$\boldsymbol{I}_s^{m+\frac{1}{2}} \approx \boldsymbol{I}_s^m\,, \tag{14}$$

for reason that will become clear in the results. Minor changes are required to incorporate losses into the update equations, as long as the resistance R and conductance G of the transmission lines are assumed non-dispersive.

D. Lossless FCI-FDTD

In this implementation, the transmission lines are again considered lossless. We employ the Fully Collocated Implicit (FCI) FDTD method [7], [8], which performs implicit time-stepping. We derive an adaptation of the method: in one dimension, with voltages and currents as field variables and with the correct boundary conditions at the terminal. We define the following matrices having nonzero elements on rows P and Q

$$\begin{aligned}
\mathbf{S}_1 &= \begin{matrix} P \\ Q \end{matrix}\!\!\begin{bmatrix} 1 & \\ & 1 \end{bmatrix} \in \mathbb{R}^{(N-1)\times 2}, \\
\mathbf{S}_L &= \begin{matrix} P \\ Q \end{matrix}\!\!\begin{bmatrix} L_{P+\frac{1}{2}} & \\ & L_{Q-\frac{1}{2}} \end{bmatrix} \in \mathbb{R}^{(N-1)\times 2}\,.
\end{aligned} \tag{15}$$

Using these in block matrices, the VCCSs terms can be added to the previously derived FCI-FDTD update scheme as follows:

$$\begin{aligned}
&\mathbf{A}_{\mathrm{FCI,IBC}} \begin{bmatrix} \boldsymbol{V}^{m+1} \\ \boldsymbol{I}^{m+1} \end{bmatrix} + \begin{bmatrix} \mathbf{0} & -\frac{\mathbf{S}_1}{2\Delta z} \\ \mathbf{0} & \frac{\mathbf{S}_L}{2\Delta t} \end{bmatrix} \begin{bmatrix} \boldsymbol{X}^{m+1} \\ \boldsymbol{I}_s^{m+1} \end{bmatrix} \\
&= \mathbf{B}_{\mathrm{FCI,IBC}} \begin{bmatrix} \boldsymbol{V}^{m} \\ \boldsymbol{I}^{m} \end{bmatrix} + \begin{bmatrix} \mathbf{0} & \frac{\mathbf{S}_1}{2\Delta z} \\ \mathbf{0} & \frac{\mathbf{S}_L}{2\Delta t} \end{bmatrix} \begin{bmatrix} \boldsymbol{X}^{m+1} \\ \boldsymbol{I}_s^{m+1} \end{bmatrix} \\
&\quad + \mathbf{C}_{\mathrm{FCI,IBC}} \begin{bmatrix} \mathbf{1}E_g^{m} \\ \mathbf{1}E_g^{m+1} \end{bmatrix}.
\end{aligned} \tag{16}$$

The FCI-FDTD method collocates variables in space and time, unlike leapfrog FDTD. Therefore, new SS discretizations are necessary. We limit ourselves to only one choice. In our State-Space Fully-Collocated Implicit FDTD (SS-FCI-FDTD) method, the state vector is extended with both $\boldsymbol{X}$ and $\boldsymbol{I}$ to obtain the following update scheme:

$$\begin{aligned}
&\left[\begin{array}{c|c} \mathbf{A}_{\mathrm{FCI,IBC}} & -\frac{\mathbf{S}_1}{2\Delta z} \\ \hline -\mathbf{B}\mathbf{S}_1^T & \frac{\mathbf{S}_L}{2\Delta t} \\ -\mathbf{D}\mathbf{S}_1^T & \mathbf{M}_1 \quad -\mathbf{C} \quad \mathbb{I}_2 \end{array}\right] \begin{bmatrix} \boldsymbol{V}^{m+1} \\ \boldsymbol{I}^{m+1} \\ \boldsymbol{X}^{m+1} \\ \boldsymbol{I}_s^{m+1} \end{bmatrix} = \left[\begin{array}{c|c} \mathbf{B}_{\mathrm{FCI,IBC}} & \frac{\mathbf{S}_1}{2\Delta z} \\ \hline & \mathbf{M}_2 \end{array}\right] \begin{bmatrix} \boldsymbol{V}^{m} \\ \boldsymbol{I}^{m} \\ \boldsymbol{X}^{m} \\ \boldsymbol{I}_s^{m} \end{bmatrix} \\
&\qquad + \left[\begin{array}{c|c} \mathbf{C}_{\mathrm{FCI,IBC}} & \\ \hline & \end{array}\right] \begin{bmatrix} \mathbf{1}E_g^{m} \\ \mathbf{1}E_g^{m+1} \\ \mathbf{0}_{n_x} \\ \mathbf{0}_2 \end{bmatrix},
\end{aligned} \tag{17}$$

where, again, the $\mathbf{M}$ matrices are specific to the SS discretization.

III. Results and Discussion

A. Methods

As all schemes are linear, there exists a constant amplification matrix $\mathbf{G}$ such that

$$\boldsymbol{U}^{m+1} = \mathbf{G}\boldsymbol{U}^m + \boldsymbol{S}^m\,, \tag{18}$$

where $\boldsymbol{S}^m$ is a column vector containing elements originating from the generator source. This LTI system is exponentially stable if and only if none of the eigenvalues of $\mathbf{G}$ lie outside the unit circle. The matrix $\mathbf{G}$ is extracted directly from the implementation using Van Londersele's approach [8, p. 132]. We derive the following expression

$$\xi \leq \frac{\ln(g)\Delta t}{t_{\mathrm{tot}}} = \xi_{\max}\,, \tag{19}$$

where ξ is the spectral radius minus one and g is the growth of entries in $\boldsymbol{U}$ after a time t_{tot} when the simulation is unstable. This provides us with a maximal value for $\xi_{\max}$ that produces acceptable late time unstable simulations. Simulations are *practically stable* when $\log(\xi) < -6$. This means no exponential growth will be noticeable in any of the performed simulations. However, simulations are still useable until approximately $\log(\xi) = -3.5$. We call the stability of simulations with $-6 < \log(\xi) < -3.5$ *limited*. Higher values yield unstable simulations.

The parameters for the lossless impementations are chosen arbitrarily. The parameters for the lossy implementation are taken from a real coaxial TSV [9]. The only exception is $d = 2\,\mathrm{cm}$ for all implementations to facilitate comparisons. In FDTD, we choose the size of the discretizations in space and time as

$$\begin{aligned}
\Delta z &= \left(\frac{1}{f_{\max \mathrm{N}_\lambda}}\right) v_{\min}\,, \\
\Delta t &= \left(\frac{\alpha_{\mathrm{Courant}}}{f_{\max \mathrm{N}_\lambda}}\right) \frac{v_{\min}}{v_{\max}}\,,
\end{aligned} \tag{20}$$

where N_λ is the number of cells per wavelength, f and v are the frequency and phase velocity of the signal excitations. We fix $f_{\max}$ and vary the free parameters in the range

$$\begin{aligned}
0 < \alpha_{\mathrm{Courant}} < 1\,, \\
N_\lambda > 10\,.
\end{aligned} \tag{21}$$

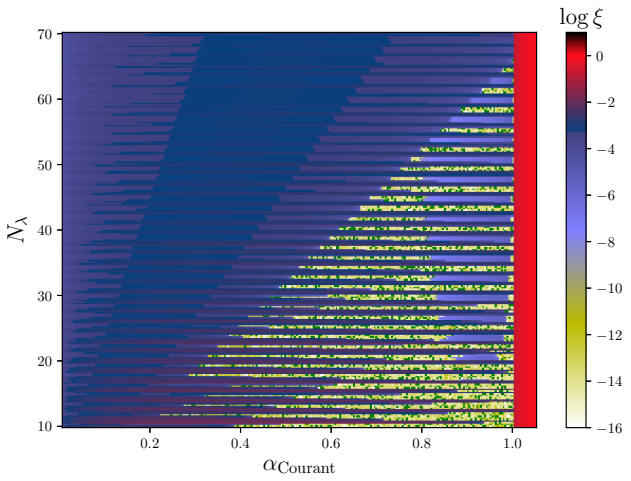

Fig. 2: An example of a choice where intricate patterns are seen that influence stability. The logarithm of the stability measure ξ is plotted in a contourplot as function of the free parameters α_{Courant} and N_λ. The VCCSs voltages are sampled by averaging over the interface. The evaluation points m and m are used with the BE method. The lossless DSA operator is used.

The general approach to examine results is through a series of experiments where the free choices and parameters are compared. Explanations are usually given a posteriori. One exception is a proof based on [10], for the stability of the scheme when the VCCSs do not feed into the computational domain.

B. Lossless Leapfrog

The lossless case causes eigenvalues of the SS scheme to either be on the unit circle when the BE method is used or potentially outside when the TR method is used. We explain this by machine precision errors, who also affect the stability of the full scheme. Poles λ_c of the continuous system $\mathbf{A}$ are mapped to eigenvalues λ_d of the discrete scheme as

$$\lambda_d = \frac{\frac{1}{\Delta t} + \frac{\lambda_c}{2}}{\frac{1}{\Delta t} - \frac{\lambda_c}{2}} \,. \tag{22}$$

One can show that $|\lambda_d| < 1$ if $\mathrm{Re}\{\lambda_c\} < 0$. We observe that computing (22) with double-precision floating-point numbers sometimes leads to $|\lambda_d| = 1 + 1.11 \times 10^{-16} > 1$, even though $\mathrm{Re}\{\lambda_c\} < 0$. This is not the case for the mapping corresponding to the BE method:

$$\lambda_d = \frac{\frac{1}{\Delta t}}{\frac{1}{\Delta t} - \lambda_c} \,, \tag{23}$$

As a result, the exact bounds on stability were intricate. The patterns varied by α_{Courant}, N_λ, the free choices and the operator used. An example for a specific set of choices is shown in Figure 2.

We then examined the error of our schemes for a specific stable simulation. In general, good to very good accuracies were found in the time domain. This is also the case in the frequency domain, as shown in Figure 3. Here, transfer functions of the voltage right of the central transmission lines with respect to the source are shown in a broad band. This is obtained as is usual with a modulated Gaussian pulse shifted in time. As with all results, the accuracy deteriorates at frequencies approximately 25% lower than the maximum fitted frequency of VF, which we did not expect.

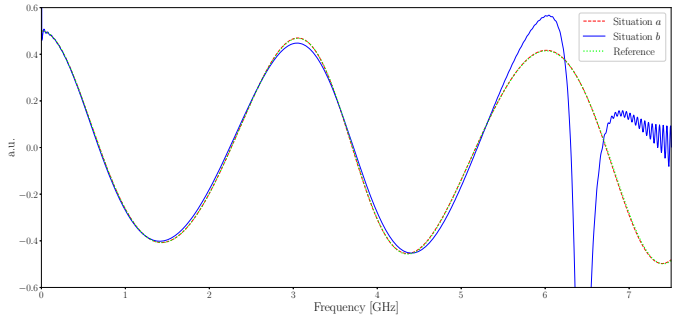

Fig. 3: Transfer functions from simulations of both situations. Situation a and b have free parameters $\alpha_{\text{Courant}} = 0.99$ and $N_\lambda = 64$. The reference simulation of situation a has parameters $\alpha_{\text{Courant}} = 0.99$ and $N_\lambda = 200$. The same choices as in Figure 2 are used.

C. Lossy Leapfrog

Introducing small losses was expected to attenuate instabilities and ease the VF procedure. Unfortunately, the stability was not improved. When simulations were stable, similar accuracies were observed. However, the stable configurations were rare and sometimes impossible to find. We resorted to the approximated scheme, alleviating the instability at the cost of a substantial decrease in accuracy. The influence on the accuracy is shown in Figure 4. For brevity, we do not show the reduced accuracy in this extended abstract.

We then observed the stability when *both* situations have a lossy SA operator, as the SS subsystem was still marginally stable. The eigenvalues of the SS scheme are then all inside the unit circle. However, the full system was still unstable. Remarkably, it therefore appears that the stability problems are caused by the coupling with FDTD, regardless of the eigenvalues of the SA operators. This hampered our ability to obtain stable and accurate results for more complex situations, such as when R and G of the transmission line are dispersive.

D. Lossless FCI-FDTD

The best results among all tested methods were found with the SS-FCI-FDTD method in terms of stability and accuracy. The former was significantly improved due to the greater flexibility in α_{Courant}, as shown in Figure 5. The latter was especially good when $\alpha_{\text{Courant}} = 1$, worsening for higher values. The transfer function is shown in Figure 6. The NRMSE[2] from DC to 5.5 GHz is 1.35%. The NRMSE from DC to 0.5 GHz is 0.15%.

[2]Normalized with the range of the spectra.

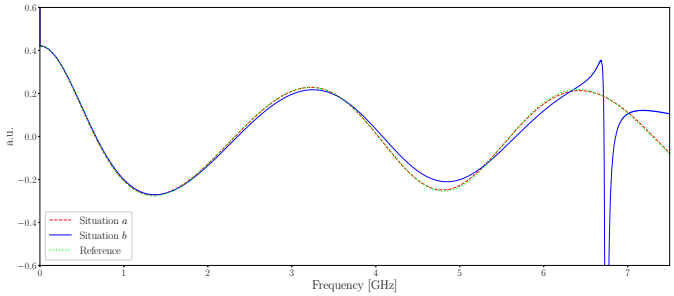

(a) Without the approximated scheme.

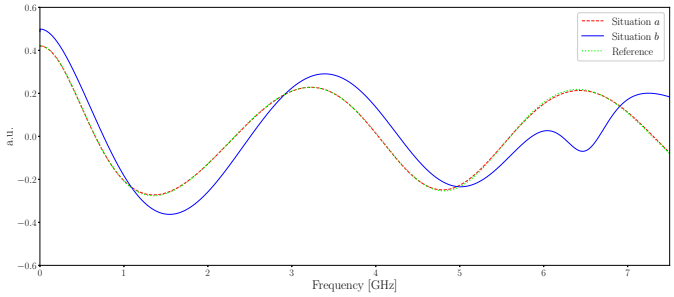

(b) With the approximated scheme.

Fig. 4: Transfer functions from simulations of both situations with and without the approximated scheme. Situation a and b have free parameters $\alpha_{\text{Courant}} = 0.8$ and $N_\lambda = 22.5$. The reference simulation of situation a has parameters $\alpha_{\text{Courant}} = 0.99$ and $N_\lambda = 200$. The VCCSs voltages are sampled on $z = P\Delta z$ and $z = Q\Delta z$. The evaluation points m and m are used with the BE method. The lossy non-dispersive SA operator of situation a is used.

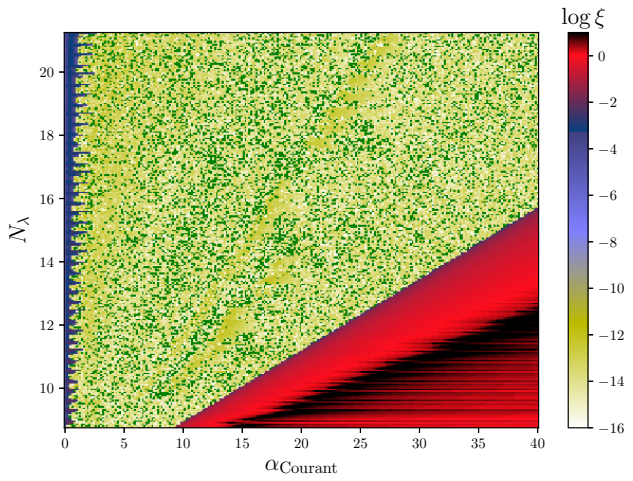

Fig. 5: A stability analysis for the lossless SS-FCI-FDTD full system. The logarithm of the stability measure ξ is plotted in a contourplot as function of the free parameters α_{Courant} and N_λ.

IV. Conclusions and Future Work

A new idea was explored to model the skin effect. For this VF was used to convert DtN operators to the time domain in a SS representation. Three distinct implementations were given, each with further free choices available. The stability was found to depend in a large part on machine precision errors. The accuracy is, in general, (very) good over a broad frequency range. The SS-FCI-FDTD is the most performant method both in terms of stability and accuracy.

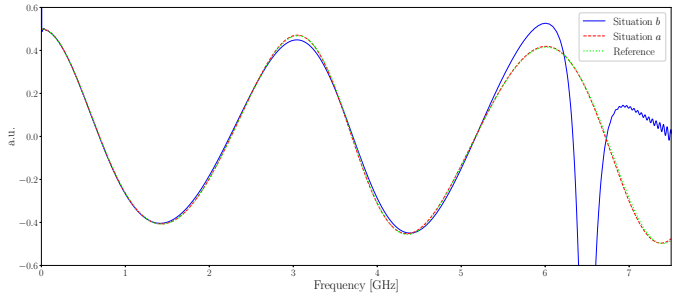

Fig. 6: Transfer functions from simulations of both situations when the SS-FCI-FDTD method is employed. Situation a and b have $N_\lambda = 64$. The reference simulation of situation a has $N_\lambda = 200$. The free parameter $\alpha_{\text{Courant}} = 1$. The lossless DSA operator is used.

The most natural continuation of this work is probably the derivation of more advanced SS-FCI-FDTD numerical schemes. For example, one could add passive SA operators to study the lossy systems, possibly for different free choices. Another approach is explaining observations in the present work with rigorously proven a priori theorems. Finally, the method can be generalized to higher dimensions while incorporating Maxwell's laws.

V. References

[1] Daniël De Zutter and Luc Knockaert, "Skin effect modeling based on a differential surface admittance operator," *IEEE Transactions on Microwave Theory and Techniques*, vol. 53, no. 8, pp. 2526–2538, aug 2005.

[2] B. Gustavsen and A. Semlyen, "Rational approximation of frequency domain responses by vector fitting," *IEEE Transactions on Power Delivery*, vol. 14, no. 3, pp. 1052–1061, 1999.

[3] B. Gustavsen, "Improving the pole relocating properties of vector fitting," *IEEE Transactions on Power Delivery*, vol. 21, no. 3, pp. 1587–1592, 2006.

[4] Dirk Deschrijver, Michal Mrozowski, Tom Dhaene, and Daniel De Zutter, "Macromodeling of multiport systems using a fast implementation of the vector fitting method," *IEEE Microwave and Wireless Components Letters*, vol. 18, no. 6, pp. 383–385, 2008.

[5] Adam Semlyen and Bjørn Gustavsen, "A half-size singularity test matrix for fast and reliable passivity assessment of rational models," *IEEE Transactions on Power Delivery*, vol. 24, no. 1, pp. 345–351, 2009.

[6] Bjørn Gustavsen, "Fast passivity enforcement for pole-residue models by perturbation of residue matrix eigenvalues," *IEEE Transactions on Power Delivery*, vol. 23, no. 4, pp. 2278–2285, 2008.

[7] Wouter Tierens and Daniël De Zutter, "An unconditionally stable time-domain discretization on cartesian meshes

for the simulation of nonuniform magnetized cold plasma," *Journal of Computational Physics*, vol. 231, no. 15, pp. 5144–5156, 2012.

[8] Arne Van Londersele, *Novel Finite-Difference Time-Domain Techniques to Model Multiscale Electromagnetic Problems*, Ph.D. thesis, Ghent University, 2018.

[9] Zheng Xu and Jian-Qiang Lu, "Three-dimensional coaxial through-silicon-via (tsv) design," *IEEE Electron Device Letters*, vol. 33, no. 10, pp. 1441–1443, 2012.

[10] Xinyue Zhang, Fadime Bekmambetova, and Piero Triverio, "A stable fdtd method with embedded reduced-order models," *IEEE Transactions on Antennas and Propagation*, vol. 66, no. 2, pp. 827–837, 2018.

Contents

List of Figures

List of Tables

Chapter 1

Introduction

1.1 Motivation

The global semiconductor industry market size is US$ 425 billion and projected to grow to US$ 803 billion in 2028 [1]. Demand for high performance integrated circuits (ICs) exceeds supply, as indicated by the recent semiconductor shortage. There is a need for state-of-the-art technologies that rely on high-performance ICs. For example, the emergence of 5G requires high data throughput and operates at high frequencies. Also, the Internet of Things (IoT) paradigm requires a large number of devices with increasingly miniaturized chips. Furthermore, an increasing number of industries rely on the use of high-speed electronics such as most recently the automotive industry.

One of the most crucial tools for designing this hardware is through Electronic Computer-Aided Design (ECAD), for example for the inexpensive optimization and validation of the devices. To obtain these high hardware performances, ICs are often stacked in three dimensions on electrically small Printed Circuit Boards (PCBs). Modeling the PCBs at high frequencies is best done using full-wave simulators. These do not just use circuit theory but rather directly incorporate Maxwell's laws of electromagnetism. A versatile, fast and accurate ECAD solver enables designers to more easily account for all the intricate effects at play in their devices. Distortion, ringing, dispersion, signal attenuation, skin effect and crosstalk are examples of an important set of effects we focus on. These influence the Signal Integrity (SI) and Electromagnetic Compatibility (EMC) of the electronic device [2]. A time domain simulator is needed which is performant under high frequencies and small lengths. The most popular time domain simulation tool to study SI and EMC is the Finite-Difference Time-Domain (FDTD) method. This mature simulation method has a large number of advantages. Examples include the immediate broadband modeling with one simulation, a well-understood and generally good accuracy and stability, a high degree of versatility and simplicity. Its most important drawback is the Courant limit, which imposes a maximal time step with which the simulation marches on in time.

One particularly difficult phenomenon to model in FDTD is the skin effect. At high frequencies,

currents crowd to the outer layer of good conductors. Correctly modeling these current layers is crucial for the accuracy at larger scales. Therefore, the skin depth imposes a minimal size on the spatial discretizations of the simulation grid. The depth of this layer is usually orders of magnitudes smaller than the smallest component of the device. If a uniform grid is used, the majority of the simulation space is more resolved than necessary. Moreover, the Courant limit will proportionally decrease the maximal time step. Both of these cause the computation to become orders of magnitudes longer and more inefficient, to the detriment of the design process.

1.2 Situation and Objective

Accurately and efficiently modeling the skin effect has been the subject of a large body of research in the electromagnetic modeling literature. A multitude of different solutions can be found within a number of subfields of this literature. We give a non-exhaustive overview of the general approaches in these subfields. A historical and simple solution was to make abstraction of the skin effect itself and represent it by a surface impedance. The standard FDTD method is conserved with the addition of simple boundary conditions at the outside of conductors. This approach fails when considering the skin effect at the edges of, e.g., rectangular conductors. Here, the field distribution changes, which is not easily accounted for by a surface impedance. In addition, the method fails at the high frequency limit [3]. Another popular method is Boundary Integral Equations (BIEs). In this method, the surface of the conductor is meshed. Each element radiates with a certain Green's function. In the Poggio-Miller-Chang-Harrington-Wu-Tsai (PMCHWT) method this is applied for Maxwell's laws in the frequency domain [4]. The approach can also be used in the time domain [5, 6]. Many integrals must be computed, often containing singularities that are not always easily solved. In addition, FDTD is a more accurate time domain method. Another family of subfields use non-uniform grids that resolve only the skin effect in greater detail. In subgridding, a fine grid to resolve the skin effect in greater detail is embedded inside a coarse grid. A major problem in this subfield is guaranteeing the stability of the simulations. This is often caused by the explicit nature of the update equations in FDTD. Implicit time-marching schemes have been developed with unconditional stability [7, 8]. However, this comes at the cost of increased computational costs required to solve matrix systems at each time step. Hybrid Implicit-Explicit (HIE) methods that conserve the explicit nature in one dimension can be used [9]. This method works well if one direction can be chosen perpendicular to all the conductor surfaces. A final approach we discuss is the use of so-called macromodels in conjunction with FDTD. Briefly put, a macromodel expresses a complex system in a reduced form at the cost of a (minor) decrease in accuracy. A popular approach is the use of Model Order Reduction (MOR) to reduce the complexity of a subgridded conductor surface [10–12]. These techniques also suffer from stability problems.

None of the above approaches simultaneously combine simplicity, versatility, reliability and accuracy. The broadband modeling of good conductors up to high frequencies is however needed without any drawbacks. The method proposed in this thesis aims to achieve this. Our method

lies at the intersection of macromodeling in FDTD and the use of the Dirichlet-to-Neumann (DtN) operator, or closely related, the Differential Surface Operator (DSA). The DSA operator has been proposed to circumvent the skin effect [13] in the frequency domain. Based on the Field Equivalence Theorem (FET), equivalent electric currents are placed on the surface to make abstraction of the conductive material causing the skin effect. The operator gives an expression for these currents in the frequency domain. As explained above, a time domain method is preferred for the study of many important effects. The macromodeling approach Vector Fitting (VF) is employed to cast the operator to the time domain, while also reducing its complexity in an accurate manner. We implemented this approach in one dimension. The DtN operator is used to abstract a transmission line in the longitudinal direction. As a result, a proof-of-concept is provided to apply the operator in higher dimensions for skin effects appearing in full-wave simulations.

1.3 Outline

The purpose of Chapter 2 is twofold. First and foremost, it provides a background on a number of established methods or concepts our research builds on. It is not intended to explain fundamentals expected from a graduate level electrical engineering or engineering physics student. Introductory books and sources will be referenced if this is not the case. More advanced topics are briefly explained. Here, we emphasise parts that have the most important consequences for this work. Citations will be provided for further reading. Second, it introduces the notation and scope for the subsequent chapters.

Chapter 3 starts with formulating the goal by combining the highlighted ideas of Chapter 2. Implementations of the DSA operator are explained in general terms. This includes three variations on the same topology of transmission lines. Each implementation requires a simulation method that is fundamentally different. Each method has a number of options available that are slightly different.

Chapter 4 covers the results and discussion. First, a number of methods to efficiently process and represent results of a large set of choices is given. Second, the most relevant results are reported and explained where possible. This is done for each implementation. Here, the need for each of them will become clearer.

Finally, Chapter 5 briefly concludes our implementations and findings. Here we also provide some interesting paths for future work.

Chapter 2

Preliminaries

2.1 Notation and Maxwell's Equations

Throughout this thesis, a consistent notation is used for electromagnetic fields and circuit quantities. Frequency domain variables are given a hat. Discrete samples in space or time of continuous fields are capitalized. Collections of these in the form of vectors of matrices are marked bold. Additionally, the former is italicized. The notation and units of basic electromagnetic quantities are introduced in Table 2.1. We present the well-known Maxwell equations as a starting point, including magnetic charges with Weber's convention. The curl equations are

$$\begin{cases} \frac{\partial}{\partial t}\boldsymbol{b}(\mathbf{r},t) &= -\nabla\times\boldsymbol{e}(\mathbf{r},t) - \boldsymbol{k}_{\text{total}}(\mathbf{r},t) \\ \frac{\partial}{\partial t}\boldsymbol{d}(\mathbf{r},t) &= \nabla\times\boldsymbol{h}(\mathbf{r},t) - \boldsymbol{j}_{\text{total}}(\mathbf{r},t) \end{cases} \overset{e^{j\omega t}}{\longrightarrow} \begin{cases} j\omega\hat{\boldsymbol{b}}(\mathbf{r}) &= -\nabla\times\hat{\boldsymbol{e}}(\mathbf{r}) - \hat{\boldsymbol{k}}_{\text{total}}(\mathbf{r})\,, \\ j\omega\hat{\boldsymbol{d}}(\mathbf{r}) &= \nabla\times\hat{\boldsymbol{h}}(\mathbf{r}) - \hat{\boldsymbol{j}}_{\text{total}}(\mathbf{r})\,, \end{cases} \tag{2.1}$$

where the arrow expresses the transformation to the frequency domain employing the $e^{j\omega t}$-dependence. Magnetic charges do not exist (or at least have not been observed). However, magnetic currents appear in Love's field equivalence principle. Furthermore, these currents have a simple circuit theory interpretation as impressed voltage sources [14]. This can be anticipated from the boundary conditions associated to (2.1):

$$\begin{cases} \vec{n}\times(\boldsymbol{e}_2-\boldsymbol{e}_1) &= -\boldsymbol{k}_{\text{s}} \\ \vec{n}\times(\boldsymbol{h}_2-\boldsymbol{h}_1) &= \boldsymbol{j}_{\text{s}} \end{cases} \longrightarrow \begin{cases} \vec{n}\times(\hat{\boldsymbol{e}}_2-\hat{\boldsymbol{e}}_1) &= -\hat{\boldsymbol{k}}_{\text{s}}\,, \\ \vec{n}\times(\hat{\boldsymbol{h}}_2-\hat{\boldsymbol{h}}_1) &= \hat{\boldsymbol{j}}_{\text{s}}\,, \end{cases} \tag{2.2}$$

where $\vec{n}$ is the normal outward vector from medium 1 to medium 2. Note that the units of the electric and magnetic surface current densities $\hat{\boldsymbol{j}}_{\text{s}}$ and $\hat{\boldsymbol{k}}_{\text{s}}$ are A/m and V/m, respectively. Only linear isotropic nondispersive materials are treated in this thesis. We can use (2.1) in a macroscopic sense if we define constitutive equations

$$\begin{cases} \boldsymbol{d}(\mathbf{r}) = \varepsilon(\mathbf{r})\boldsymbol{e}(\mathbf{r}) \\ \boldsymbol{b}(\mathbf{r}) = \mu(\mathbf{r})\boldsymbol{h}(\mathbf{r}) \end{cases} \longrightarrow \begin{cases} \hat{\boldsymbol{d}}(\mathbf{r}) = \varepsilon(\mathbf{r})\hat{\boldsymbol{e}}(\mathbf{r})\,, \\ \hat{\boldsymbol{b}}(\mathbf{r}) = \mu(\mathbf{r})\hat{\boldsymbol{h}}(\mathbf{r})\,, \end{cases} \tag{2.3}$$

where $\varepsilon(\mathbf{r})$ and $\mu(\mathbf{r})$ can assume different values than those of vaccuum. In the frequency domain, complex permittivities are written as $\varepsilon = \varepsilon' - j\varepsilon''$.

Name	Symbol	Units
Electric field	$\boldsymbol{e}$	V/m
Electric flux density	$\boldsymbol{d}$	C/m^2
Magnetic field	$\boldsymbol{h}$	A/m
Magnetic flux density	$\boldsymbol{b}$	Wb/m^2
Electric current density	$\boldsymbol{j}$	A/m^2
Magnetic current density	$\boldsymbol{k}$	V/m^2
Electric surface current density	$\boldsymbol{j}_s$	A/m
Magnetic surface current density	$\boldsymbol{k}_s$	V/m
Electric permittivity	ε	F/m
Magnetic permeability	μ	H/m
Electric conductivity	σ	S/m
Magnetic conductivity	σ^*	Ω/m

Table 2.1: The name, symbol and units of the quantities introduced in this section.

In the time domain, we incorporate ohmic losses by splitting the currents in external and internal sources, with the latter obeying Ohm's law such that

$$\begin{aligned} \boldsymbol{j}_{\text{total}} &= \boldsymbol{j} + \sigma \boldsymbol{e}\,, \\ \boldsymbol{k}_{\text{total}} &= \boldsymbol{k} + \sigma^* \boldsymbol{h}\,. \end{aligned} \tag{2.4}$$

$\boldsymbol{j}$ and $\boldsymbol{k}$ are independent sources, i.e., those that provide external energy to the fields.

2.2 Field Equivalence Theorem and Differential Surface Admittance Operator

The Field Equivalence Theorem (FET) is a well-known fundamental theorem of electromagnetism. Love's form of the principle [15] will be repeated here. The reader is invited to consult [16, 17] for a more elaborate explanation of this section. Consider an arbitrary subdivision of two-dimensional (2-D) or three-dimensional (3-D) space by a fictitious, closed and bounded surface S. The normal vector $\vec{n}$ is directed outward from the interior region (named region I) to the exterior region (named region II). With this construction, we will consider two different electromagnetic configurations, named *situation a* and *situation b*, which are shown in Figure 2.1. We start by describing situation a. The interior region can contain arbitrary, possibly anisotropic or inhomogeneous materials. The exterior region is homogeneous, source-free and assumed to be free-space for simplicity. A set of impressed sources, denoted $(\hat{\boldsymbol{j}}, \hat{\boldsymbol{k}})$, are located within region I. They produce the electromagnetic fields $(\hat{\boldsymbol{e}}_i, \hat{\boldsymbol{h}}_i)$ in region I and $(\hat{\boldsymbol{e}}_o, \hat{\boldsymbol{h}}_o)$ in region II. In situation b, the sources in region I are replaced by surface currents, distributed on the surface S. These are given by

$$\begin{aligned} \hat{\boldsymbol{j}}_s &= \vec{n} \times \hat{\boldsymbol{h}}_o\,, \\ \hat{\boldsymbol{k}}_s &= -\vec{n} \times \hat{\boldsymbol{e}}_o\,, \end{aligned} \tag{2.5}$$

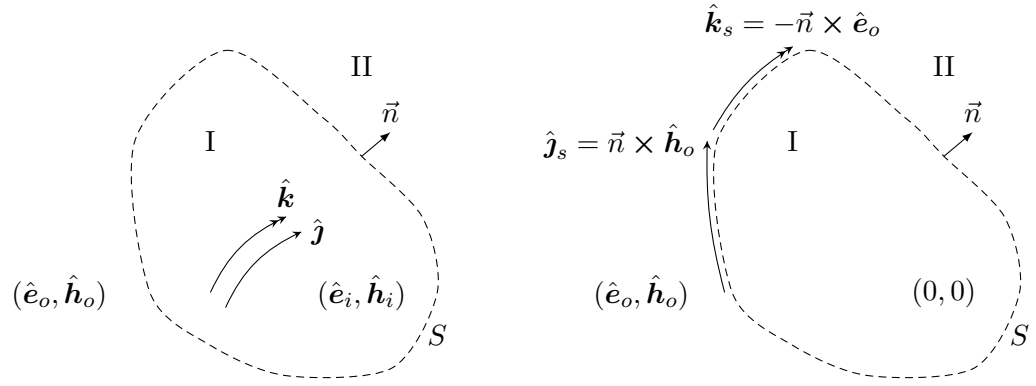

(a) *Situation a* or the original situation. (b) *Situation b* or the equivalent situation.

Figure 2.1: An illustration of Love's form of the FET for a fictitious surface S. Situation a represents the scattering of impressed current sources $(\hat{\boldsymbol{j}}, \hat{\boldsymbol{k}})$ within S. They produce fields inside (subscript i) and outside (subscript o), denoted as regions I and II, respectively. In situation b, these sources are removed and replaced by an impressed surface current density $(\hat{\boldsymbol{j}}_s, \hat{\boldsymbol{k}}_s)$ on S. This results in null-fields $(0, 0)$ inside S and identical fields outside S.

where $\hat{\boldsymbol{e}}_o$ and $\hat{\boldsymbol{h}}_o$ are evaluated on the location of the surface current densities. Love's form of the FET now states that the electromagnetic fields in region I are null everywhere. A rigorous proof is provided in [18] and its non-intuitive nature is discussed in [19]. As this formalism is based on the uniqueness theorem, a unique solution is found unless resonant solutions are present in S. By assuming vanishingly small losses inside S, the solution is unique. As a consequence, the materials of region I can be replaced by free-space without influencing the outside field distribution.

A single source variation of Love's FET[1] can be formulated [20]. The equivalence is shown in Figure 2.2. In this formulation, no magnetic surface currents are impressed on S. This reduced degree of freedom results in an arbitrary field distribution $(\hat{\boldsymbol{e}}_v, \hat{\boldsymbol{h}}_v)$ in region I of situation b. They do not carry any physical meaning or useful information about the original fields $(\hat{\boldsymbol{e}}_i, \hat{\boldsymbol{h}}_i)$ inside the volume. Therefore they are named *virtual* fields. Furthermore, the boundary condition

$$\vec{n} \times \hat{\boldsymbol{e}}_o = \vec{n} \times \hat{\boldsymbol{e}}_v \,, \tag{2.6}$$

is imposed and the electric surface current now becomes

$$\hat{\boldsymbol{j}}_s = \vec{n} \times (\hat{\boldsymbol{h}}_o - \hat{\boldsymbol{h}}_v) \,. \tag{2.7}$$

The materials in region I can still be replaced by the background medium.

The skin effect problem does not appear if the conductive material can be replaced by the background medium. Hybrid methods combining FDTD with other methods modeling the equivalent currents were developed with this goal in mind. We cite for example [21] in the time domain and [22] in the frequency domain. De Zutter and Knockaert first used the above formulation [13] with

[1] henceforth shortened to 'the FET'

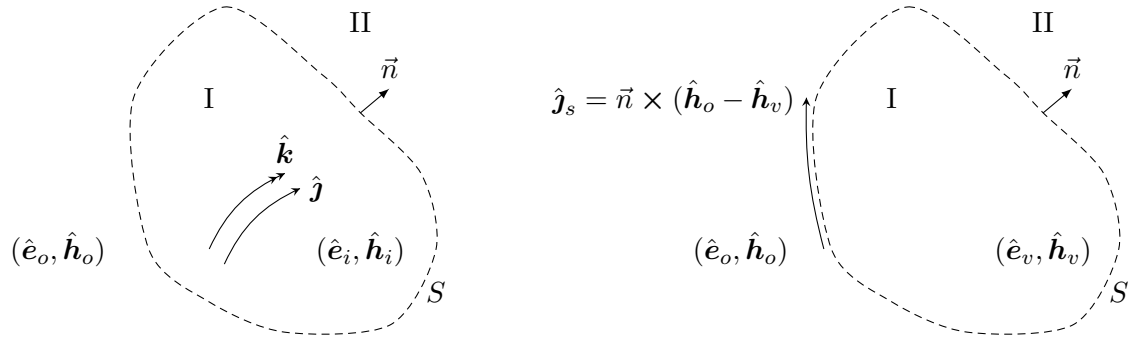

(a) *Situation a* or the original situation. (b) *Situation b* or the equivalent situation.

Figure 2.2: An illustration of the single source variation on Love's FET for a fictitious surface S. Situation a represents the scattering of impressed current sources $(\hat{\boldsymbol{j}}, \hat{\boldsymbol{k}})$ within S. They produce fields inside (subscript i) and outside (subscript o), denoted as regions I and II, respectively. In situation b, these sources are removed and replaced by impressed electric surface current densities $\hat{\boldsymbol{j}}_s$ on S. This results in virtual fields (subscript v) inside S and identical fields outside S.

a Differential Surface Admittance (DSA) operator in 2005. Once determined, it is applicable to the entire simulation, or any simulation for that matter, using the same abstracted material. The problem was initially considered in the frequency domain in 2-D and was subsequently generalized to the 3-D case [2]. Knowledge of the unknown surface currents is required to model the electromagnetic problem. If we define the Surface Admittance (SA) operators $\mathcal{Y}_a$, $\mathcal{Y}_b$ by

$$\begin{aligned} \hat{\boldsymbol{h}}_o &= \mathcal{Y}_a \hat{\boldsymbol{e}}_o \,, \\ \hat{\boldsymbol{h}}_v &= \mathcal{Y}_b \hat{\boldsymbol{e}}_v \,, \end{aligned} \tag{2.8}$$

the DSA operator $\mathcal{Y}$ can be constructed as

$$\hat{\boldsymbol{j}}_s = (\mathcal{Y}_a - \mathcal{Y}_b)(\vec{n} \times \hat{\boldsymbol{e}}_o) = \mathcal{Y}(\vec{n} \times \hat{\boldsymbol{e}}_o) \,, \tag{2.9}$$

where the boundary condition (2.6) was used. These equations only hold for fields on S in two ($D = 2$) or three ($D = 3$) dimensions. Consider a sampling of $\hat{\boldsymbol{j}}_s$ and $(\vec{n} \times \hat{\boldsymbol{e}}_o)$ on this surface in N points. All components are collected in the vectors $\hat{\boldsymbol{J}}_s$ and $\hat{\boldsymbol{E}}_s$ of size DN, respectively. As a result, the discretized DSA operator $\hat{\mathbf{Y}}$ becomes a matrix with dimensions $DN \times DN$:

$$\hat{\boldsymbol{J}}_s = \hat{\mathbf{Y}} \hat{\boldsymbol{E}}_s \,. \tag{2.10}$$

We will use both the DSA and the SA operators. A Dirichlet-to-Neumann (DtN) operator $\hat{\mathcal{D}}_i$ is defined as

$$\hat{\mathbf{Y}}_k = \frac{1}{j\omega\mu_0} \hat{\mathcal{D}}_k \,, \tag{2.11}$$

for any (differential) SA operator $\hat{\mathbf{Y}}_k$. The DSA operator and its implementation are provided in the frequency domain as this is the most natural way of characterizing the DSA. This is usually done by an expansion in eigenfunctions of the cross-section. Sometimes, analytical expressions are available for simple geometries, as is the case for this thesis. To interface the DSA operator with FDTD, (2.10) needs to be converted into a time-marching scheme.

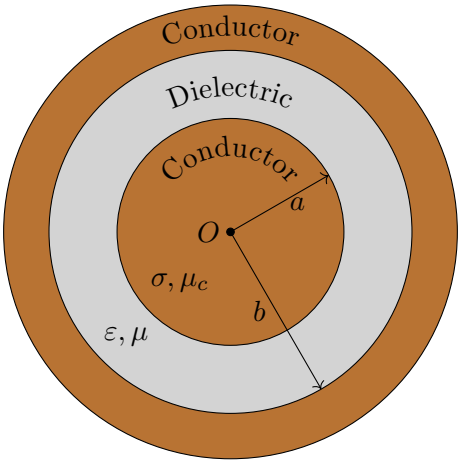

Figure 2.3: The geometry of the cross-section of a coaxial cable. Copper colored regions represent good conductors. The grey region represents the insulating dielectric. Radii of the circular regions are denoted a and b from the center O. The outer conductor is grounded.

2.3 Transmission Lines

Single electrical transmission lines for wired communication purposes are used throughout this thesis. The geometry of the invariant cross-section is that of a coaxial cable or coaxial TSV. This is represented in Figure 2.3. The core is a good conductor with a conductivity σ and permeability μ_c. It is surrounded by a dielectric insulator characterized by the constitutive parameters $\varepsilon = \varepsilon' - j\varepsilon''$ and μ. Their radii are denoted by a and b, respectively. The outer conductor is a grounded good conductor. An overview of multiconductor transmission line theory is provided in [23]. The size of the transverse section is electrically small with respect to the minimal wavelength of the waveforms $\lambda_{\min}$:

$$2\pi(a+b) \ll \frac{\lambda_{\min}}{2}\,.$$

If this condition is fulfilled, the transmission line can be described from a circuit theory point of view. Otherwise, higher order modes are present and a full-wave analysis is necessary. This analysis leads to the telegrapher's equation in the frequency domain:

$$\frac{\mathrm{d}\hat{v}(z)}{\mathrm{d}z} = -(R + j\omega L)\hat{\imath}(z)\,, \tag{2.12a}$$

$$\frac{\mathrm{d}\hat{\imath}(z)}{\mathrm{d}z} = -(G + j\omega C)\hat{v}(z)\,, \tag{2.12b}$$

The per-unit-of-length (p.u.l.) distributed parameters R, L, G, C are given by [24]

$$R = \frac{1}{2\pi\delta\sigma}\left(\frac{1}{a}+\frac{1}{b}\right), \tag{2.13a}$$

$$L = \frac{\mu}{2\pi}\ln\frac{b}{a}, \tag{2.13b}$$

$$G = \frac{2\pi\omega\varepsilon''}{\ln\frac{b}{a}}, \tag{2.13c}$$

$$C = \frac{2\pi\varepsilon'}{\ln\frac{b}{a}}. \tag{2.13d}$$

The skin depth arises in the expression for R and is equal to

$$\delta = \sqrt{\frac{2}{\omega\mu_c\sigma}}. \tag{2.14}$$

We want to model transmission lines in the time domain. If the materials can be assumed lossless, the resistive parameters R and G vanish. The remaining parameters L and C are frequency-independent, thus allowing a trivial conversion to the time domain:

$$\frac{\partial v(z,t)}{\partial z} = -L\frac{\partial i(z,t)}{\partial t}, \tag{2.15a}$$

$$\frac{\partial i(z,t)}{\partial z} = -C\frac{\partial v(z,t)}{\partial t}. \tag{2.15b}$$

The resistive parameters can be evaluated in a specific frequency ω' to obtain $R_{\omega'} = R(\omega = \omega')$ and $G_{\omega'} = G(\omega = \omega')$. This approximation holds insofar as the simulated signals have their spectral content near this frequency. Incorporating these in the conversion to the time domain yields

$$\frac{\partial v(z,t)}{\partial z} = -R_{\omega'}i(z,t) - L\frac{\partial i(z,t)}{\partial t}, \tag{2.16a}$$

$$\frac{\partial i(z,t)}{\partial z} = -G_{\omega'}v(z,t) - C\frac{\partial v(z,t)}{\partial t}. \tag{2.16b}$$

We now consider the general lossy case with frequency dependent R and G parameters. The p.u.l. resistance (2.13a) is usually written as

$$R = A + B\sqrt{s}, \tag{2.17}$$

where s is the Laplace variable [25]. This expression is approximated in the high-frequency limit such that $R \approx B\sqrt{s}$. Furthermore, the conductance G is approximated to be negligible compared to the $j\omega C$ term. Hence, this model is named *partially* dispersive. This approximation is justified in the majority of real transmission lines. According to [23] the time domain telegrapher's equations become

$$\frac{\partial v(z,t)}{\partial z} = -\frac{1}{\sqrt{\pi}}B\left[\int_0^t \frac{1}{\sqrt{\tau}}\frac{\partial}{\partial(t-\tau)}\hat{\imath}(z,t-\tau)d\tau\right] - L\frac{\partial i(z,t)}{\partial t}, \tag{2.18a}$$

$$\frac{\partial i(z,t)}{\partial z} = -C\frac{\partial v(z,t)}{\partial t}. \tag{2.18b}$$

When frequency dependent dielectric losses are nonetheless taken into account, we obtain the *fully* dispersive model. We write (2.13c) as

$$G = Ds\,, \tag{2.19}$$

resulting in time domain telegrapher's equations

$$\frac{\partial v(z,t)}{\partial z} = -\frac{1}{\sqrt{\pi}} B \left[\int_0^t \frac{1}{\sqrt{\tau}} \frac{\partial}{\partial(t-\tau)} \hat{\imath}(z, t-\tau) d\tau \right] - L \frac{\partial i(z,t)}{\partial t}\,, \tag{2.20a}$$

$$\frac{\partial i(z,t)}{\partial z} = -D \frac{\partial i(z,t)}{\partial t} - C \frac{\partial v(z,t)}{\partial t}\,. \tag{2.20b}$$

For all of the above models, the general solution in the Laplace domain is

$$\hat{v}(z,s) = \hat{v}^+(s) e^{-jk(s)z} + \hat{v}^-(s) e^{jk(s)z}\,, \tag{2.21a}$$

$$\hat{\imath}(z,s) = \frac{1}{Z(s)} \left[\hat{\imath}^+(s) e^{-jk(s)z} - \hat{\imath}^-(s) e^{jk(s)z} \right]\,, \tag{2.21b}$$

with characteristic impedance

$$Z(s) = \sqrt{\frac{R+sL}{G+sC}}\,, \tag{2.22}$$

and wave number

$$k(s) = \sqrt{-(R+sL)(G+sC)}\,. \tag{2.23}$$

2.4 Simulation Methods

The FDTD method was first introduced by Kane Yee in 1966 [26]. It is considered a mature modeling technique and is explained in standard textbooks [27, 28]. These references also contain more elaborate discussion on all advantages and disadvantages. As mentioned in Section 1.1, the FDTD method is particularly useful for SI and EMC applications. This is because transient phenomena and non-linear materials are accounted for naturally. We also stressed the need for broadband modeling of good conductors without any drawbacks. By correctly post-processing a single run with appropriate sources, this is easily achieved in FDTD. The most important drawback is the significantly higher computational requirements to simulate current crowding in a thin layer.

To illustrate this, consider a typical simulation involving heterogeneous dielectrics with relative permittivities $\varepsilon_r(\mathbf{r})$ and good conductors operating at high frequencies. Most of the source's spectral content is contained in a broad band having a supremum $f_{\max}$. The time step is Δt. The simulation space[2] is tessellated with Yee-cells. Their size Δz is chosen proportional to the smallest wavelength that needs to be resolved $\lambda_{\min}$:

$$\Delta z = \frac{\lambda_{\min}}{N_\lambda} = \frac{v_{\min}}{f_{\max} N_\lambda}\,, \tag{2.24}$$

[2] taken as one-dimensional purely for illustration purposes

where N_λ is the number of cells per wavelength. A value of 30 is more than enough to mitigate numerical dispersion [29]. When a uniform grid is used, second-order accuracy in space is achieved. For dielectrics we have $v_{\min} = c/\sqrt{\max(\varepsilon_r(\mathbf{r}))}$. However, the resulting Δz is unable to resolve the skin depth in, e.g., copper by multiple orders of magnitude [30]. Moreover, reducing Δz additionally impacts the computational cost through a reduction of the time step. This is clear by the Courant–Friedrichs–Lewy (CFL) stability condition [31, 32]:

$$\Delta t < \frac{\Delta z}{v_{\max}} \,. \tag{2.25}$$

The Fully-Collocated Implicit (FCI) FDTD method is an implicit method first introduced by Tierens in 2012 [7] and improved by Van Londersele [8]. The method is unconditionally stable, while standard FDTD imposes a maximal time step. The fully-collocated grid guarantees the continuity of both the electric and the magnetic field. This is in contrast with standard FDTD only guaranteeing the continuity of one field quantity. The FCI-FDTD method is also second-order accurate in space.

2.5 Macromodeling

We consider general Multiple Input Multiple Output (MIMO) Linear Time Invariant (LTI) systems. Their transfer function $\hat{\mathbf{H}}(s)$ relates the input $\hat{\boldsymbol{U}}(s)$ and output $\hat{\boldsymbol{Y}}(s)$ signals in the Laplace domain by

$$\hat{\boldsymbol{Y}}(s) = \hat{\mathbf{H}}(s)\hat{\boldsymbol{U}}(s) \,. \tag{2.26}$$

A macromodel is an approximation of any LTI model or device as a less complex system description. While macromodeling has been around for a long time, the Vector Fitting (VF) algorithm developed by Gustavsen and Semlyen [33–37] in the late 1990's greatly advanced the field due to its simplicity, accuracy and robustness. In this procedure, $\hat{\mathbf{H}}(s)$ is approximated by a rational fit:

$$\hat{\mathbf{H}}(s) \approx \widetilde{\mathbf{H}}(s) = \hat{\mathbf{R}}_0 + \sum_{i=1}^{N_p} \frac{\hat{\mathbf{R}}_i}{s - p_i} \,. \tag{2.27}$$

The poles p_i and residues $\hat{\mathbf{R}}_i$ are chosen such that the error between $\widetilde{\mathbf{H}}(s)$ and $\hat{\mathbf{H}}(s)$ is minimized. Higher model orders N_p will in general increase accuracy. These poles and residues enable the expression of $\widetilde{\mathbf{H}}(s)$ as a generalized State-Space (SS) representation:

$$\begin{aligned} \mathbf{E}\frac{\mathrm{d}}{\mathrm{d}t}\boldsymbol{X}(t) &= \mathbf{A}\boldsymbol{X}(t) + \mathbf{B}\boldsymbol{U}(t) \,, \\ \boldsymbol{Y}(t) &= \mathbf{C}\boldsymbol{X}(t) + \mathbf{D}\boldsymbol{U}(t) \,. \end{aligned} \tag{2.28}$$

Only regular SS systems are treated in this thesis, i.e., $\hat{\mathbf{E}}$ is full rank. In this case, the most general form is

$$\begin{aligned} \frac{\mathrm{d}}{\mathrm{d}t}\boldsymbol{X}(t) &= \mathbf{A}\boldsymbol{X}(t) + \mathbf{B}\boldsymbol{U}(t) \,, \\ \boldsymbol{Y}(t) &= \mathbf{C}\boldsymbol{X}(t) + \mathbf{D}\boldsymbol{U}(t) \,. \end{aligned} \tag{2.29}$$

In the above, $\boldsymbol{U}(t) \in \mathbb{R}^{n_u}$ and $\boldsymbol{Y}(t) \in \mathbb{R}^{n_y}$ are the continuous time domain counterparts of $\hat{\boldsymbol{U}}(s)$ and $\hat{\boldsymbol{Y}}(s)$. The vector $\boldsymbol{X}(t) \in \mathbb{R}^{n_x}$ collects the time varying state variables.

Only a subset of all accurate macromodels are actually useful to utilize in numerical time domain simulations. Besides basic criteria such as stability and causality, the most important required property is passivity of the system. We refer to the book by Grivet-Talocia and Gustavsen [38] for a thorough explanation of passive macromodeling with the VF algorithm. The general SS system (2.29) is strictly passive if

$$\hat{\boldsymbol{\Psi}}(j\omega) = \widetilde{\mathbf{H}}(j\omega) + \widetilde{\mathbf{H}}^{\top}(-j\omega) > 0\,, \quad \forall\omega. \tag{2.30}$$

For this test, the Popov function $\hat{\boldsymbol{\Psi}}$ can be sampled for all frequencies, or non-passive bands can be delimited by generalized eigenvalues of an extended Hamiltonian pencil [38]. Passivity implies causality, and Bounded-Input, Bounded-Output (BIBO) stability if the system $\widetilde{\mathbf{H}}(s)$ has no singularities on the imaginary axis [39]. In this thesis, we will only encounter admittance matrices $\widetilde{\mathbf{H}}(s)$ that satisfy the symmetry and conjugacy properties. As a result, (2.30) can be simplified to

$$\mathrm{Re}\{\widetilde{\mathbf{H}}(j\omega)\} > 0\,, \tag{2.31}$$

or in other words, all eigenvalues of $\mathrm{Re}\{\widetilde{\mathbf{H}}(j\omega)\}$ are positive [36]. When the original system $\hat{\mathbf{H}}(s)$ is not passive in a wide band, vector fitting the model while enforcing passivity will be unacceptably inaccurate or simply impossible.

Transfer functions $\hat{\mathbf{H}}$ relating the terminal ports of long transmission lines are highly dynamic. Vector fitting of a large amount of resonance peaks leads to difficulties in obtaining accurate models, unless a high number of poles N_p is used. Delayed Vector Fitting (DVF) is a more efficient technique to model transmission lines of large electrical length [38, Sec. 12]. Briefly put, multiple propagation delays are formally incorporated in (2.27). However, these delays translate to a more complex formulation of (2.29). Naturally, the incorporation of such SS schemes into a FDTD is more complex. Therefore, we will not consider this method. The applicability of this work is for short transmission lines at high frequencies that can be expected in, e.g., integrated circuits. Another macromodeling approach is Model Order Reduction (MOR) [38, Sec. 5]. Here, the starting point is not (2.26), but a SS representation relating time domain inputs to outputs. In FDTD, electric fields can be related to magnetic fields on the surface of a subgridded region by directly deriving a SS system from the update equations [10, 12]. The exceedingly large size of the state vector is significantly reduced by MOR. The resulting discrete SS system is easily simulated. The embedding of this system into a FDTD grid and its stability have been researched. While we will not use this method, the general approach and SS embedding into FDTD is similar. The literature of this field provides points of attention for this work. First, the combined MOR-FDTD system is not necessarily stable if the macromodel is passive [11, 40]. However, a modular approach exists with formally proven stability [40]. Second, the interpolation rule at the macromodel boundary is important to ensure stability of the combined system [41]. Finally, introducing (small) losses will ease the passivity enforcement of lossless macromodels [11]. This work is original in the following ways. First, the powerful DSA is used

to convert any model defined in the frequency domain to the time domain. Besides the skin effect, this can include more complex physics that are not trivial to simulate in the time domain. Second, VF is the favored macromodeling approach for its simplicity, accuracy and robustness.

Chapter 3

Implementation of the DSA Operator on Transmission Lines

3.1 Introduction

Now that the preliminaries have been covered, the goal can be clearly stated. The discrete DSA operator appearing in (2.10) is accurately macromodeled:

$$\hat{\mathbf{Y}}(s) \approx \widetilde{\mathbf{Y}}(s) = \hat{\mathbf{R}}_0 + \sum_{i=1}^{N_p} \frac{\hat{\mathbf{R}}_i}{s - p_i} \,. \tag{3.1}$$

This causal, stable and passive model is constructed with VF. A SS representation as in (2.29) is obtained where the input and output are the time domain equivalent of $\hat{\boldsymbol{E}}_o$ and $\hat{\boldsymbol{J}}_s$, respectively. The former is found through either leapfrog FDTD or FCI-FDTD, but will also depend on the current sources it outputs. Therefore, time-marching schemes that integrate the vector fitted SS model into FDTD simulation methods are proposed in this thesis. The skin effect disappears when replacing region I in Figure 2.2 by vacuum. As a result, one of the greatest challenges of leapfrog FDTD is circumvented, allowing accurate broadband modeling of good conductors in region II.

This chapter specifies our implementations of this unexplored approach. Its scope is defined in the following. First, the problem is considered in one dimension, such that the boundary of S consists of two points. This reduces the complexity of the VF procedure and the spatial discretization of the combined scheme. Second, region I and II are chosen to be transmission lines. The well-known and tractable physics allow for a closed analytical form of the DSA operator.

In a first step, the lossless case is considered. This instructive example constitutes an edge case when it comes to guaranteeing the stability of the combined scheme. Leapfrog FDTD is used as the modeling technique. A second implementation introduces losses in the central transmission line, which contributes to the intended engineering goal of this thesis. This implementation is reasonably realistic and will suffer from less stability problems. A final implementation is again

lossless but uses FCI-FDTD as the modeling technique.

Both situation a and b are depicted in Figure 3.1. They consist of a series connection of three lossless transmission lines of the type described in Section 2.3. Only the central transmission line of situation a has different material parameters (subscript 1) compared to the surrounding transmission lines (subscript 0), taking the role of the background material. The interfaces of the central line with the others are situated at nodes $\mathcal{P}$ and $\mathcal{Q}$ to the left and right, respectively. Their position will depend on the grid of each implementation. A voltage source $e_g(t)$ is added in series with a resistor R_g at the generator side. A resistor R_L is inserted at the load side.

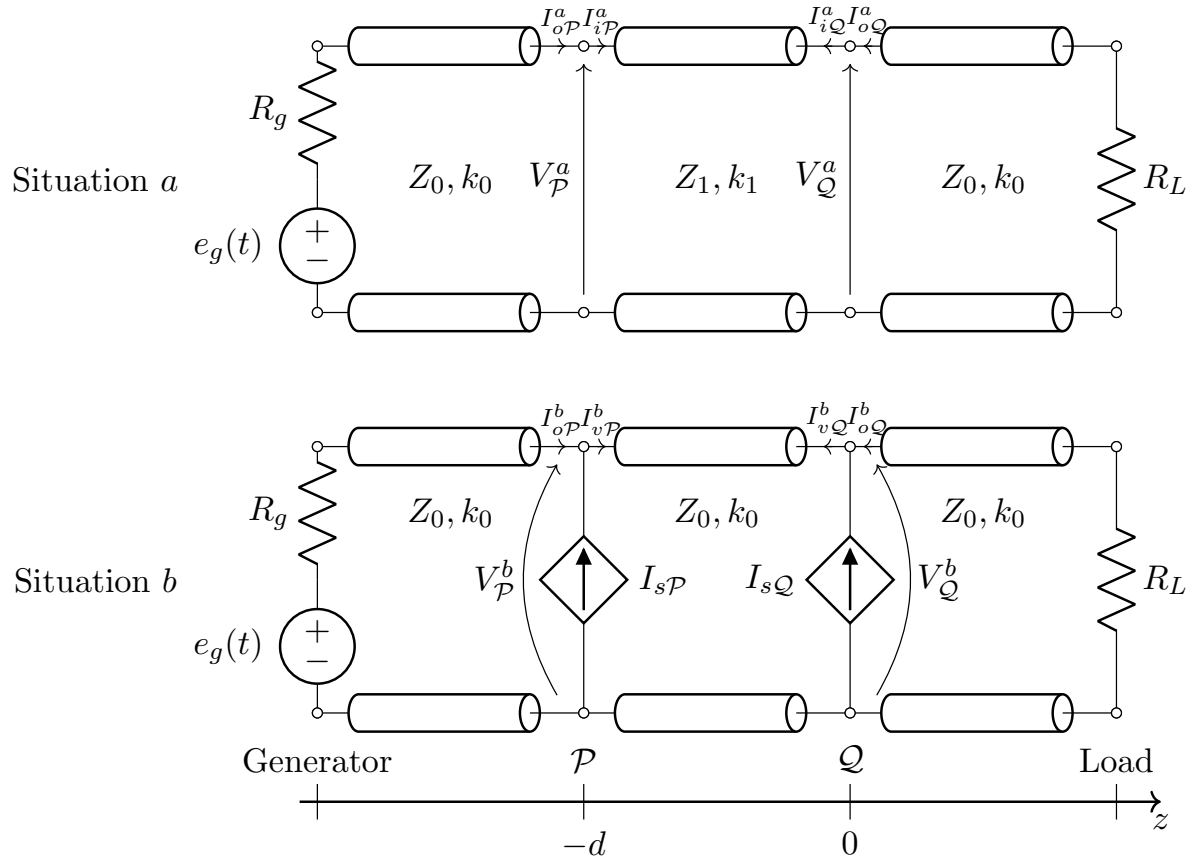

Figure 3.1: Situations of the FET applied to three transmission lines. The single-conductor transmission lines are depicted by two cylinders, the bottom one grounded. The transmission lines are in direct electrical contact at interfacial nodes $\mathcal{P}$ and $\mathcal{Q}$. Currents around these nodes have a superscript denoting the corresponding situation. The subscript denotes if they correspond to inside (i), outside (o), virtual (v) or surface (s) currents in the FET. The central transmission line has length d.

3.2 Lossless Leapfrog

3.2.1 DSA Operator Construction

The background parameters of the central transmission line are chosen as lossless

$$\begin{aligned} Z_1 &= \sqrt{\frac{j\omega L}{j\omega C}}\,, \\ k_1 &= \sqrt{-j\omega L j\omega C}\,, \end{aligned} \tag{3.2}$$

and are therefore real numbers. The voltages and currents satisfy the general solution (2.21). In situation a on the central line we have

$$\begin{aligned} \hat{v}^a(z) &= Ae^{-jk_1 z} + Be^{+jk_1 z}\,, \\ \hat{\imath}^a(z) &= \frac{1}{Z_1}\left(Ae^{-jk_1 z} - Be^{+jk_1 z}\right)\,. \end{aligned} \tag{3.3}$$

The voltage and current values on the nodes $\mathcal{P}$ and $\mathcal{Q}$ are

$$\begin{aligned} \hat{V}^a_{\mathcal{P}} &= \hat{v}^a(-d) = Ae^{+jk_1 d} + Be^{-jk_1 d}\,, \\ \hat{I}^a_{i\mathcal{P}} &= \hat{\imath}^a(-d) = \frac{1}{Z_1}\left(Ae^{+jk_1 d} - Be^{-jk_1 d}\right)\,, \\ \hat{V}^a_{\mathcal{Q}} &= \hat{v}^a(0) = A + B\,, \\ \hat{I}^a_{i\mathcal{Q}} &= -\hat{\imath}^a(0) = \frac{B - A}{Z_1}\,, \end{aligned} \tag{3.4}$$

taking into account the length d of this transmission line. As such, the relationship between current and voltage at the nodes is given by:

$$\begin{bmatrix} \hat{I}^a_{i\mathcal{P}} \\ \hat{I}^a_{i\mathcal{Q}} \end{bmatrix} = \widetilde{\mathbf{Y}}^a \begin{bmatrix} \hat{V}^a_{\mathcal{P}} \\ \hat{V}^a_{\mathcal{Q}} \end{bmatrix} \quad \text{with} \quad \widetilde{\mathbf{Y}}^a = \frac{-j}{Z_1} \begin{bmatrix} \frac{1}{\tan k_1 d} & \frac{-1}{\sin k_1 d} \\ \frac{-1}{\sin k_1 d} & \frac{1}{\tan k_1 d} \end{bmatrix}\,. \tag{3.5}$$

Note that infinite currents are obtained when $\sin k_1 d$ is zero. This occurs when $k_1 d = n\pi$ with $n = 0, 1, 2, \ldots$ Situation b is analogous except for the different material parameters of the central transmission line. The relationship between current and voltage is therefore given by:

$$\begin{bmatrix} \hat{I}^b_{v\mathcal{P}} \\ \hat{I}^b_{v\mathcal{Q}} \end{bmatrix} = \widetilde{\mathbf{Y}}^b \begin{bmatrix} \hat{V}^b_{\mathcal{P}} \\ \hat{V}^b_{\mathcal{P}} \end{bmatrix} \quad \text{with} \quad \widetilde{\mathbf{Y}}^b = \frac{-j}{Z_0} \begin{bmatrix} \frac{1}{\tan k_0 d} & \frac{-1}{\sin k_0 d} \\ \frac{-1}{\sin k_0 d} & \frac{1}{\tan k_0 d} \end{bmatrix}\,. \tag{3.6}$$

Here, infinite currents appear for $k_0 d = n\pi$ with $n = 0, 1, 2, \ldots$

While a description has been given of both situations, nothing has been said about their relationship to the FET. This theorem is stated in 2-D or 3-D using electromagnetic fields. It can be shown that under the assumptions of Section 2.3, circuit equivalents of $\hat{\boldsymbol{e}}$ and $\hat{\boldsymbol{h}}$ as voltages and currents can be used, respectively. Enforcing (2.6) in situation b then entails the infinitesimal continuity of voltage across a node. The electric surface currents become two shunt Voltage Controlled Current Sources (VCCSs) that feed into the interfacial nodes. Assume for now in this

one-dimensional (1-D) circuit variation of the FET that the outside fields are in fact identical. For the voltages we have

$$\begin{bmatrix} \hat{V}^a_{\mathcal{P}} \\ \hat{V}^a_{\mathcal{Q}} \end{bmatrix} = \begin{bmatrix} \hat{V}^b_{\mathcal{P}} \\ \hat{V}^b_{\mathcal{Q}} \end{bmatrix} \triangleq \begin{bmatrix} \hat{V}_{\mathcal{P}} \\ \hat{V}_{\mathcal{Q}} \end{bmatrix}. \tag{3.7}$$

Here we enforced the continuity of voltage across a node. The currents are also identical on the outside:

$$\begin{bmatrix} \hat{I}^a_{o\mathcal{P}} \\ \hat{I}^a_{o\mathcal{Q}} \end{bmatrix} = \begin{bmatrix} \hat{I}^b_{o\mathcal{P}} \\ \hat{I}^b_{o\mathcal{Q}} \end{bmatrix}. \tag{3.8}$$

For the currents in situation a we apply Kirchoff's Current Law (KCL) on the interfacial nodes:

$$\begin{bmatrix} \hat{I}^a_{o\mathcal{P}} \\ \hat{I}^a_{o\mathcal{Q}} \end{bmatrix} = \begin{bmatrix} \hat{I}^a_{i\mathcal{P}} \\ \hat{I}^a_{i\mathcal{Q}} \end{bmatrix}. \tag{3.9}$$

For the currents in situation b we also apply KCL on the interfacial nodes:

$$\begin{bmatrix} \hat{I}_{s\mathcal{P}} \\ \hat{I}_{s\mathcal{Q}} \end{bmatrix} = \begin{bmatrix} \hat{I}^b_{v\mathcal{P}} \\ \hat{I}^b_{v\mathcal{Q}} \end{bmatrix} - \begin{bmatrix} \hat{I}^b_{o\mathcal{P}} \\ \hat{I}^b_{o\mathcal{Q}} \end{bmatrix}. \tag{3.10}$$

This is the equivalent of the expression for the electric surface currents of the FET (2.7). All the above conclusions yield an expression for the VCCSs:

$$\begin{aligned} \begin{bmatrix} \hat{I}_{s\mathcal{P}} \\ \hat{I}_{s\mathcal{Q}} \end{bmatrix} &= \widetilde{\mathbf{Y}}^b \begin{bmatrix} \hat{V}^b_{\mathcal{P}} \\ \hat{V}^b_{\mathcal{Q}} \end{bmatrix} - \widetilde{\mathbf{Y}}^a \begin{bmatrix} \hat{V}^a_{\mathcal{P}} \\ \hat{V}^a_{\mathcal{Q}} \end{bmatrix} \\ &= \left(\widetilde{\mathbf{Y}}^b - \widetilde{\mathbf{Y}}^a\right) \begin{bmatrix} \hat{V}_{\mathcal{P}} \\ \hat{V}_{\mathcal{Q}} \end{bmatrix} = \widetilde{\mathbf{Y}} \begin{bmatrix} \hat{V}_{\mathcal{P}} \\ \hat{V}_{\mathcal{Q}} \end{bmatrix}. \end{aligned} \tag{3.11}$$

One can show that assuming identical outside fields is indeed correct when the above expression is used for the VCCSs. The analogous procedure to the FET provides credibility to this assumption.

Only the real part of

$$\widetilde{\mathbf{Y}} = \frac{-j}{Z_0} \begin{bmatrix} \frac{1}{\tan k_0 d} & \frac{-1}{\sin k_0 d} \\ \frac{-1}{\sin k_0 d} & \frac{1}{\tan k_0 d} \end{bmatrix} - \frac{-j}{Z_1} \begin{bmatrix} \frac{1}{\tan k_1 d} & \frac{-1}{\sin k_1 d} \\ \frac{-1}{\sin k_1 d} & \frac{1}{\tan k_1 d} \end{bmatrix}. \tag{3.12}$$

appears in condition (2.31). As Z and k are real, $\mathrm{Re}\{\widetilde{\mathbf{Y}}\} = 0$ and all its eigenvalues are zero. This can be interpreted as an ideal lossless system being marginally passive: no net energy is absorbed or created. Passivity can nonetheless be guaranteed by requiring the eigenvalues to be strictly positive. In practice, this comes at the cost of a reduction in accuracy, especially when the original model is highly dynamic. To achieve this, however, the fitted model becomes poorly conditioned.

3.2.2 FDTD Implementation

In the following, the z-axis points toward the load side and has its origin at the generator side. The continuous voltages $v(z,t)$ and material parameters $L(z)$ and $C(z)$ are discretized on

steps $z = n\Delta z$ with $n = 0, \ldots, N$. The continuous currents $i(z,t)$ are discretized on steps $(n + 1/2)\Delta z$ with $n = 0, \ldots, N-1$. When solving (2.15), this particular choice forces the averaging of $L(z)$ onto half-integer locations. Here the harmonic mean $L_{n+1/2} = 2\left(1/L_n + 1/L_{n+1}\right)^{-1}$ is used. This approximates the location of both interfaces to lie at the center of the cells, but conformal methods can be used to improve this [27, 28]. The currents and voltages are discretized in time in a leapfrog fashion with time index m. With second-order accurate finite differences, the following leapfrog FDTD is obtained:

$$\begin{aligned} I_{n+\frac{1}{2}}^{m+\frac{1}{2}} &= I_{n+\frac{1}{2}}^{m-\frac{1}{2}} + \alpha_{L,n+\frac{1}{2}} \left(V_n^m - V_{n+1}^m\right) , \\ V_n^{m+1} &= V_n^m + \alpha_{C,n} \left(I_{n-\frac{1}{2}}^{m+\frac{1}{2}} - I_{n+\frac{1}{2}}^{m+\frac{1}{2}}\right) , \end{aligned} \tag{3.13}$$

where the notation

$$\begin{aligned} \alpha_{C,n} &\triangleq \frac{\Delta t}{C_n \Delta z} , \\ \alpha_{L,n+\frac{1}{2}} &\triangleq \frac{\Delta t}{L_{n+\frac{1}{2}} \Delta z} , \end{aligned} \tag{3.14}$$

was employed. For these terminal networks, it can be shown that the boundary update equations are given by [28]

$$\begin{aligned} V_0^{m+1} &= K_g V_0^m - 2\kappa_g R_g I_{\frac{1}{2}}^{m+\frac{1}{2}} + 2\kappa_g E_g^{m+\frac{1}{2}} , \\ V_N^{m+1} &= K_L V_N^m + 2\kappa_L R_L I_{N-\frac{1}{2}}^{m+\frac{1}{2}} , \end{aligned} \tag{3.15}$$

with

$$\begin{aligned} K_g &= \frac{R_g - \alpha_{C,0}}{R_g + \alpha_{C,0}} , \quad K_L &&= \frac{R_L - \alpha_{C,N}}{R_L + \alpha_{C,N}} , \\ \kappa_g &= \frac{\alpha_{C,0}}{R_g + \alpha_{C,0}} , \quad \kappa_L &&= \frac{\alpha_{C,N}}{R_L + \alpha_{C,N}} . \end{aligned} \tag{3.16}$$

To incorporate the VCCSs of the SS model, KCL has to be applied at the interfaces between the TLs. We examine the material interface to the left side, with the right side being analogous. The material parameters C_P and L_P belong to the central transmission line, while C_{P-1} and L_{P-1} belong to the left transmission line. The exact position of the interface on the discretized grid is ambiguous. One possibility is to consider it on the half-integer location $z = (P-1/2)\Delta z$, because $L_{P-1/2}$ is determined by both L_{P-1} and L_P. Note that this is atypical compared to full-wave simulations. In those cases, the currents appearing in (2.1) are naturally discretized on integer locations. This suggests another possibility, that the interface is best modeled at the integer location P. While this choice has a negligibly small impact in the continuous limit of standard Yee-FDTD simulations, its influence on the SS is unknown. Moreover, the embedding of MOR systems into FDTD has a stability that depends on the interpolation used at the macromodel boundary [41]. For this reason, results will be given for both possibilities. In the first possibility, the node $\mathcal{P}$ is positioned at $z = (P-1/2)\Delta z$[1]. The outside and virtual currents are infinitesimally adjacent to this half-integer center. They are the discretized time domain counterparts of $\hat{I}_{o\mathcal{P}}^b$ and $\hat{I}_{v\mathcal{P}}^b$, denoted by $I_{(P-1/2)^-}^{m+1/2}$ and $I_{(P-1/2)^+}^{m+1/2}$, respectively. The discretized

[1] This interfacial node $\mathcal{Q}$ is positioned at $z = (Q+1/2)\Delta z$.

time domain counterparts of $\hat{V}_{\mathcal{P}}$ and $\hat{I}_{s\mathcal{P}}$ are denoted by $V_{\mathcal{P}}^m$ and $I_{s\mathcal{P}}^{m+1/2}$, respectively. Update equations for these currents are constructed using forward and backward differences instead of central differences. They are given by

$$\begin{aligned} I_{(P-\frac{1}{2})^-}^{m+\frac{1}{2}} &= I_{(P-\frac{1}{2})^-}^{m-\frac{1}{2}} + 2\alpha_{L,P-\frac{1}{2}} \left(V_{P-1}^m - V_{\mathcal{P}}^m\right) , \\ I_{(P-\frac{1}{2})^+}^{m+\frac{1}{2}} &= I_{(P-\frac{1}{2})^+}^{m-\frac{1}{2}} + 2\alpha_{L,P-\frac{1}{2}} \left(V_{\mathcal{P}}^m - V_P^m\right) , \end{aligned} \tag{3.17}$$

where the continuity of $v(z,t)$ and $L(z)$ has been used. The update equations of the integer step voltages around the node become

$$\begin{aligned} V_P^{m+1} &= V_P^m + \alpha_{C,P} \left(I_{(P-\frac{1}{2})^+}^{m+\frac{1}{2}} - I_{P+\frac{1}{2}}^{m+\frac{1}{2}} \right) , \\ V_{P-1}^{m+1} &= V_{P-1}^m + \alpha_{C,P-1} \left(I_{P-\frac{3}{2}}^{m+\frac{1}{2}} - I_{(P-\frac{1}{2})^-}^{m+\frac{1}{2}} \right) . \end{aligned} \tag{3.18}$$

One simple way to find the unknown half-integer voltage $V_{\mathcal{P}}^m$ is through averaging of the neighboring integer nodes:

$$V_{\mathcal{P}}^m = \frac{V_{P-1}^m + V_P^m}{2} . \tag{3.19}$$

The continuity of $v^b(z,t)$ guarantees the convergence of the above expression in the continuous limit. However, the error introduced by this approximation is significantly higher than in a homogeneous medium. This is because two different slopes of $\hat{v}^b(z)$ are expected to the left and right of the interfacial node. This error propagates to the current sources, as they are controlled by these voltages. Furthermore, KCL in the node (3.10) yields

$$I_{(P-\frac{1}{2})^+}^{m+\frac{1}{2}} = I_{s\mathcal{P}}^{m+\frac{1}{2}} + I_{(P-\frac{1}{2})^-}^{m+\frac{1}{2}} . \tag{3.20}$$

This equation substitutes the $I_{(P-1/2)^+}^{m+1/2}$ currents. It also forms the update equation for $I_{(P-1/2)^+}^{m+1/2}$. By introducing the notation $I_{(P-1/2)^-} \triangleq I_{P-1/2}$ we can conveniently rewrite (3.17) and (3.18) as

$$\begin{aligned} I_{P-\frac{1}{2}}^{m+\frac{1}{2}} &= I_{P-\frac{1}{2}}^{m-\frac{1}{2}} + \alpha_{L,P-\frac{1}{2}} \left(V_{P-1}^m - V_P^m\right) , \\ V_P^{m+1} &= V_P^m + \alpha_{C,P} \left(I_{P-\frac{1}{2}}^{m+\frac{1}{2}} - I_{P+\frac{1}{2}}^{m+\frac{1}{2}} \right) + \alpha_{C,P} I_{s\mathcal{P}}^{m+\frac{1}{2}} , \\ V_{P-1}^{m+1} &= V_{P-1}^m \alpha_{C,P-1} \left(I_{P-\frac{3}{2}}^{m+\frac{1}{2}} - I_{P-\frac{1}{2}}^{m+\frac{1}{2}} \right) . \end{aligned} \tag{3.21}$$

In conclusion, the update equations can be preserved with the addition of an impressed source term $\alpha_{C,P} I_{s\mathcal{P}}^{m+\frac{1}{2}}$ for V_P^{m+1} when the VCCSs attach on half-integer locations $P-1/2$ and $Q+1/2$. With a similar derivation one can show that the same conclusion holds when the VCCSs attach on integer locations P and Q. In this case, however, the VCCSs are controlled by the voltages on these integer locations. Therefore, no averaging in space as in (3.19) is required:

$$V_{\mathcal{P}}^m = V_P^m . \tag{3.22}$$

The final leapfrog FDTD incorporating the VCCSs as source terms is:

$$I_{n+\frac{1}{2}}^{m+\frac{1}{2}} = I_{n+\frac{1}{2}}^{m-\frac{1}{2}} + \alpha_{L,n+\frac{1}{2}} \left(V_n^m - V_{n+1}^m \right) , \tag{3.23a}$$

$$V_0^{m+1} = K_g V_0^m - 2\kappa_g R_g I_{\frac{1}{2}}^{m+\frac{1}{2}} + 2\kappa_g E_g^{m+1/2} \tag{3.23b}$$

$$V_N^{m+1} = K_L V_N^m + 2\kappa_L R_L I_{N-\frac{1}{2}}^{m+\frac{1}{2}} , \tag{3.23c}$$

$$V_n^{m+1} = V_n^m + \alpha_{C,n} \left(I_{n-\frac{1}{2}}^{m+\frac{1}{2}} - I_{n+\frac{1}{2}}^{m+\frac{1}{2}} \right) \tag{3.23d}$$

$$+ \delta_{n,P} \alpha_{C,n} I_{s\mathcal{P}}^{m+\frac{1}{2}} + \delta_{n,Q} \alpha_{C,n} I_{s\mathcal{Q}}^{m+\frac{1}{2}} \quad , \quad n \neq 0, n \neq N . \tag{3.23e}$$

3.2.3 State-Space Discretization Scheme

As explained in Section 2.5, vector fitting of (3.11) results in a SS representation

$$\frac{\mathrm{d}}{\mathrm{d}t} \boldsymbol{X}(t) = \mathbf{A}\boldsymbol{X}(t) + \mathbf{B}\boldsymbol{V}_s(t) , \tag{3.24a}$$

$$\boldsymbol{I}_s(t) = \mathbf{C}\boldsymbol{X}(t) + \mathbf{D}\boldsymbol{V}_s(t) , \tag{3.24b}$$

with the continuous time domain counterparts of $\begin{bmatrix} \hat{V}_{\mathcal{P}} \\ \hat{V}_{\mathcal{Q}} \end{bmatrix}$ and $\begin{bmatrix} \hat{I}_{s\mathcal{P}} \\ \hat{I}_{s\mathcal{Q}} \end{bmatrix}$ as inputs and outputs, respectively. For the former, either (3.19) or (3.22) is applied depending on which possibility is chosen for the location of the interface. We now consider the discretization in time of the SS equations (3.24) and the SS variables $\boldsymbol{V}_s(t)$, $\boldsymbol{X}(t)$, $\boldsymbol{I}_s(t)$. We will consider evaluation points on half-integer or integer time steps. In the continuous limit the differences in evaluation points become negligible. This causes no initial restrictions on the choice among the resulting combinations. However, the stability and rate of convergence may be different among these choices, which is why several possibilities are tested here. Note that the evaluation point of (3.24a) is not necessarily the same as the evaluation point of (3.24b). A large number of approaches arise, of which only a subset are viable, for various reasons.

First, the choice of both evaluation points influences the choice of discretization in time of the SS variables. Averaging a SS variable in time can be leveraged in this procedure:

$$\boldsymbol{X}(t)|_{t=t_0} \approx \frac{\boldsymbol{X}(t_0 + \Delta t/2) + \boldsymbol{X}(t_0 - \Delta t/2)}{2} . \tag{3.25}$$

It introduces half-integer time step variables when integer time step evaluation points are used, and vice versa.

Second, we wish to preserve the explicit nature of the leapfrog FDTD scheme when combining it with the SS scheme. We independently update the field variables as in (3.23). This operation defines one *iteration*. Its update equations were obtained by central differences of (2.15) in a time interval $[(m-1/2)\Delta t, (m+1)\Delta t]$. They provide $\boldsymbol{V}_s(t)$ on integer time steps and

require $\boldsymbol{I}_s(t)$ on half-integer time steps. Therefore, the SS scheme must independently output $\boldsymbol{I}_s^{m+1/2}$ using the input $\boldsymbol{V}_s^m$ or $\boldsymbol{V}_s^{m+1}$ of the FDTD scheme. Averaging in time will again prove useful to accomplish this. The SS scheme is evaluated within the same time interval during which a FDTD iteration is performed, excluding the limits. As a result, only the evaluation points m and $m + 1/2$ remain possibilities.

Third, the averaging in time of $\boldsymbol{V}_s^{m+1/2}$ produces $\boldsymbol{V}_s^{m+1}$. This input variable depends on the unknown output $\boldsymbol{I}_s^{m+1/2}$. The problem is resolved by introducing the following definitions:

$$\begin{aligned} V_n^{m+1,\text{yee}} &\triangleq V_n^m + \alpha_{C,n}\left(I_{n-\frac{1}{2}}^{m+\frac{1}{2}} - I_{n+\frac{1}{2}}^{m+\frac{1}{2}}\right), \\ \boldsymbol{\alpha}_{C,s} &\triangleq \begin{bmatrix} \alpha_{C,P} & 0 \\ 0 & \alpha_{C,Q} \end{bmatrix} \end{aligned} \tag{3.26}$$

The free choice regarding the sampling of $\boldsymbol{V}_s(t)$ (the *sampling choice*), is determined by the coefficient $\mathcal{C}$. When the VCCSs' inputs are averaged over the interface as in (3.19), $\mathcal{C} = 1$. When this is not the case as in (3.22), $\mathcal{C} = 2$. The vector $\boldsymbol{V}_s^{m+1,\text{yee}}$ spatially samples the VCCS inputs in the same way as $\boldsymbol{V}_s^{m+1}$. This can be written as follows using the coefficient $\mathcal{C}$:

$$\begin{aligned} \boldsymbol{V}_s^{m+1} &= \frac{1}{2}\left(\mathcal{C}\begin{bmatrix} V_P^m \\ V_Q^m \end{bmatrix} + (2-\mathcal{C})\begin{bmatrix} V_{P-1}^m \\ V_{Q+1}^m \end{bmatrix}\right), \\ \boldsymbol{V}_s^{m+1,\text{yee}} &= \frac{1}{2}\left(\mathcal{C}\begin{bmatrix} V_P^{m+1,\text{yee}} \\ V_Q^{m+1,\text{yee}} \end{bmatrix} + (2-\mathcal{C})\begin{bmatrix} V_{P-1}^{m+1,\text{yee}} \\ V_{Q+1}^{m+1,\text{yee}} \end{bmatrix}\right). \end{aligned} \tag{3.27}$$

We can now write (3.23d) in matrix form

$$\boldsymbol{V}_s^{m+1} = \boldsymbol{V}_s^{m+1,\text{yee}} + \frac{\mathcal{C}}{4}\boldsymbol{\alpha}_{C,s}\boldsymbol{I}_s^{m+1/2}. \tag{3.28}$$

Finally, nothing has been said on how the time derivative appearing in (3.24a) is discretized. We consider a finite difference time interval of Δt. When the eigenvalues of $\mathbf{A}$ all have a strictly negative real part, the Ordinary Differential Equation (ODE) (3.24a) has exponentially stable solutions. The stability of the numeric scheme is then guaranteed when using an A-stable method [42]. An example is the trapezoidal rule (TR):

$$\left.\frac{\mathrm{d}}{\mathrm{d}t}\boldsymbol{X}(t)\right|_{t=t_0} \approx \frac{\boldsymbol{X}(t_0 + \Delta t/2) - \boldsymbol{X}(t_0 - \Delta t/2)}{\Delta t}. \tag{3.29}$$

It is second-order accurate in time. Instead of using the TR method, an L-stable method can be used. In this case, solutions damp to zero as time goes to infinity. An example is the Backward Euler (BE) method:

$$\left.\frac{\mathrm{d}}{\mathrm{d}t}\boldsymbol{X}(t)\right|_{t=t_0} \approx \frac{\boldsymbol{X}(t_0) - \boldsymbol{X}(t_0 - \Delta t)}{\Delta t}. \tag{3.30}$$

The advantage of this method is explained in Section 4.2. The disadvantage of the BE method is its first-order accuracy in time.

The above remarks give both instructions for the construction of SS schemes and the available free choices taken in these constructions. A list of viable SS schemes is compiled in Appendix B. All SS schemes can be generalized as

$$\begin{aligned} \boldsymbol{X}^{\text{new}} &= \mathbf{M}_{11}\boldsymbol{X}^{\text{prev}} + \mathbf{M}_{12}\boldsymbol{I}_s^{m-\frac{1}{2}} + \mathbf{M}_{13}\boldsymbol{V}_s^{m} + \mathbf{M}_{14}\boldsymbol{V}_s^{m+1,\text{yee}}\,, \\ \boldsymbol{I}_s^{m+\frac{1}{2}} &= \mathbf{M}_{21}\boldsymbol{X}^{\text{prev}} + \mathbf{M}_{22}\boldsymbol{I}_s^{m-\frac{1}{2}} + \mathbf{M}_{23}\boldsymbol{V}_s^{m} + \mathbf{M}_{24}\boldsymbol{V}_s^{m+1,\text{yee}}\,. \end{aligned} \tag{3.31}$$

The $\mathbf{M}$ matrices have a number of rows equal to the vector on the left-hand side of these equations. Their number of columns is equal to the size of the vector they premultiply. Note that some of these matrices may depend on $\mathcal{C}$. The superscripts new and prev denote any discretization of $\boldsymbol{X}(t)$ in time but with the former on a later time than the latter.

3.2.4 Combined Update Scheme

Time stepping is performed in previously defined iterations. All variables are updated using variables of the current or previous iteration[2]. As shown in Appendix B, this is not always the case for every SS scheme. The problem was resolved by defining $\boldsymbol{V}_s^{m+1,\text{yee}}$. This intermediate field variable simplifies the notation of the SS update equations in matrix form. It can also be procured during the implementation. To this end, the right-hand side of (3.23d) is split into $\boldsymbol{V}_s^{m+1,\text{yee}}$ and the unknown terms from the VCCSs. The latter are added in an additional update equation, performed after the SS update equations, such that $\boldsymbol{I}_s^{m+1/2}$ is available. The following combined SS-FDTD scheme is obtained for one full iteration:

$$I_{n+\frac{1}{2}}^{m+\frac{1}{2}} = I_{n+\frac{1}{2}}^{m-\frac{1}{2}} + \alpha_{L,n+\frac{1}{2}}\left(V_n^m - V_{n+1}^m\right)\,, \tag{3.32a}$$

$$V_0^{m+1} = K_g V_0^m - 2\kappa_g R_g I_{\frac{1}{2}}^{m+\frac{1}{2}} + 2\kappa_g E_g^{m+1/2} \tag{3.32b}$$

$$V_N^{m+1} = K_L V_N^m + 2\kappa_L R_L I_{N-\frac{1}{2}}^{m+\frac{1}{2}}\,, \tag{3.32c}$$

$$V_n^{m+1,\text{yee}} = V_n^m + \alpha_{C,n}\left(I_{n-\frac{1}{2}}^{m+\frac{1}{2}} - I_{n+\frac{1}{2}}^{m+\frac{1}{2}}\right) \quad , \quad n \neq 0, n \neq N\,, \tag{3.32d}$$

$$\boldsymbol{V}_s^{m+1} = \frac{1}{2}\left(\mathcal{C}\begin{bmatrix} V_P^m \\ V_Q^m \end{bmatrix} + (2-\mathcal{C})\begin{bmatrix} V_{P-1}^m \\ V_{Q+1}^m \end{bmatrix}\right)\,, \tag{3.32e}$$

$$\boldsymbol{V}_s^{m+1,\text{yee}} = \frac{1}{2}\left(\mathcal{C}\begin{bmatrix} V_P^{m+1,\text{yee}} \\ V_Q^{m+1,\text{yee}} \end{bmatrix} + (2-\mathcal{C})\begin{bmatrix} V_{P-1}^{m+1,\text{yee}} \\ V_{Q+1}^{m+1,\text{yee}} \end{bmatrix}\right)\,, \tag{3.32f}$$

$$\boldsymbol{X}^{\text{new}} = \mathbf{M}_{11}\boldsymbol{X}^{\text{prev}} + \mathbf{M}_{12}\boldsymbol{I}_s^{m-\frac{1}{2}} + \mathbf{M}_{13}\boldsymbol{V}_s^{m} + \mathbf{M}_{14}\boldsymbol{V}_s^{m+1,\text{yee}}\,, \tag{3.32g}$$

$$\boldsymbol{I}_s^{m+\frac{1}{2}} = \mathbf{M}_{21}\boldsymbol{X}^{\text{prev}} + \mathbf{M}_{22}\boldsymbol{I}_s^{m-\frac{1}{2}} + \mathbf{M}_{23}\boldsymbol{V}_s^{m} + \mathbf{M}_{24}\boldsymbol{V}_s^{m+1,\text{yee}}\,, \tag{3.32h}$$

$$V_n^{m+1} = V_n^{m+1,\text{yee}} + \delta_{n,P}\alpha_{C,n} I_{s\mathcal{P}}^{m+\frac{1}{2}} + \delta_{n,Q}\alpha_{C,n} I_{s\mathcal{Q}}^{m+\frac{1}{2}} \quad , \quad n \neq 0, n \neq N\,. \tag{3.32i}$$

The suggested order in which these equations are written corresponds to an order in which they can be executed. However, this is not unique as some update equations may be performed earlier or later inside one iteration.

[2]Therefore the memory usage does not scale with the total number of time steps.

3.3 Lossy Leapfrog

3.3.1 DSA Operator Construction

As explained in Section 2.3, losses introduce frequency dependent parameters in the telegrapher's equations (2.12). However, the general solution (2.21) is of the same form. This means that the construction of the DSA operator is entirely analogous to the lossless case. The only difference is that $Z(\omega)$ and $k(\omega)$ are now complex when $R(\omega)$ or $G(\omega)$ are nonzero. This is the case for the central transmission line of situation a. All other lines, including those of situation b, are considered lossless without loss of generality.

To ensure passivity of the SS model, the real part of (3.12) should again have strictly positive eigenvalues. As Z_1 and k_1 are complex, $\mathrm{Re}\{\widetilde{\mathbf{Y}}\}$ will not necessarily be zero. We cannot assume in general that the condition will hold for all frequencies. An example of a simple DSA operator that is not passive is provided in Appendix A. Fortunately, the problem can be solved. It is clear that the individual Surface Admittance (SA) operators comply with (2.31) as long as a physically passive medium is modeled. Each SA operator (3.5) and (3.6) can be individually Vector Fitted to a SS representation as in (3.24). Both SS models are computed independently from each other at each time step. They each model a current $\boldsymbol{i}_s^a(t)$ and $\boldsymbol{i}_s^b(t)$ for the SA operator of situation a and situation b, respectively. The final current is then given by

$$\boldsymbol{i}_s(t) = \boldsymbol{i}_s^b(t) - \boldsymbol{i}_s^a(t)\,. \tag{3.33}$$

3.3.2 FDTD Implementation

Time-marching schemes exist for both the non-dispersive equations (2.16) and partially dispersive equations (2.18). The former has the same form as a z-directed polarized TEM wave in a sourceless lossy medium, which can be modeled by the Yee algorithm [26, 27]. The latter can also be cast into a time-marchine scheme [23], using a trick proposed by [43] to efficiently handle the convolution integral. To the best of the author's knowledge, no scheme has been developed for the fully dispersive equations (2.20). The purpose of simulating situation a is to compare with situation b and validate our results. This is possible as long as the underlying DSA operator is constructed with the same approximations. Therefore, comparisons will only be performed on a non-dispersive model, as the implementation is less complicated. The method is then sufficiently validated on the lossless and non-dispersive lossy models. The DSA operator can easily be constructed for a fully dispersive model with frequency dependent $R(\omega)$ and $G(\omega)$. It produces waveforms in situation b for which no other time-domain implementation exists to obtain them.

The harmonic mean is also used for $R_{n+\frac{1}{2}}$. The update equations are

$$\begin{aligned} I_{n+\frac{1}{2}}^{m+\frac{1}{2}} &= s_{n+\frac{1}{2}}^{i} I_{n+\frac{1}{2}}^{m-\frac{1}{2}} + c_{n+\frac{1}{2}}^{i} \left(V_n^m - V_{n+1}^m\right)\,, \\ V_n^{m+1} &= s_n^v V_n^m + c_n^v \left(I_{n-\frac{1}{2}}^{m+\frac{1}{2}} - I_{n+\frac{1}{2}}^{m+\frac{1}{2}}\right)\,, \end{aligned} \tag{3.34}$$

where the notation

$$\begin{aligned} s^i_{n+\frac{1}{2}} &= \frac{L_{n+\frac{1}{2}}/\Delta t - R_{n+\frac{1}{2}}/2}{L_{n+\frac{1}{2}}/\Delta t + G_n/2}\,, \\ c^i_{n+\frac{1}{2}} &= \frac{1/\Delta z}{L_{n+\frac{1}{2}}/\Delta t + R_{n+\frac{1}{2}}/2}\,, \\ s^v_n &= \frac{C_n/\Delta t - G_n/2}{C_n/\Delta t + G_n/2}\,, \\ c^v_n &= \frac{1/\Delta z}{C_n/\Delta t + G_n/2}\,, \end{aligned} \tag{3.35}$$

was employed. The terminal boundary conditions remain identical as the outside lines are lossless. The additional source term of, e.g., the VCCS feeding into $\mathcal{P}$ now scales with a factor c^v_P instead of $\alpha_{C,P}$.

3.3.3 State-Space Discretization Scheme

This paragraph considers quantities belonging to either SA operator (with the exception of $\boldsymbol{V}_s$), leaving out cumbersome notation to denote them. The two SS models described in 3.3.1 need to be modeled independently from each other. While this poses no problem from a theoretical viewpoint, implementations in their current form will fail. This is because the *total* VCCSs currents appearing in (3.28) no longer match the outputs of the individual SS schemes. The consequence is that there is no straightforward method to obtain $\boldsymbol{V}_s^{m+1}$, and therefore also $\boldsymbol{V}_s^{m+1/2}$. As a consequence we will limit ourselves to evaluation points on time steps m for both equations of (3.24). Results in Section 4.3 will show poor stability with both the BE and TR method. Therefore, we introduce the following approximation:

$$\boldsymbol{I}_s^{m+\frac{1}{2}} \approx \boldsymbol{I}_s^m\,, \tag{3.36}$$

With the TR method, the explicit form of the SS discretization scheme is

$$\begin{aligned} \boldsymbol{X}^{m+\frac{1}{2}} &= \left(\frac{\mathbb{I}_{n_x}}{\Delta t} - \frac{\mathbf{A}}{2}\right)^{-1} \left(\frac{\mathbb{I}_{n_x}}{\Delta t} + \frac{\mathbf{A}}{2}\right) \boldsymbol{X}^{m-\frac{1}{2}} + \mathbf{B}\boldsymbol{V}_s^m\,, \\ \boldsymbol{I}_s^{m+\frac{1}{2}} &= \frac{1}{2}\mathbf{C}\boldsymbol{X}^{m+\frac{1}{2}} + \frac{1}{2}\mathbf{C}\boldsymbol{X}^{m-\frac{1}{2}} + \mathbf{D}\boldsymbol{V}_s^m\,, \end{aligned} \tag{3.37}$$

where $\mathbb{I}_{n_x}$ denotes the unit matrix of size n_x. With the BE method, we find

$$\begin{aligned} \boldsymbol{X}^m &= \left(\frac{\mathbb{I}_{n_x}}{\Delta t} - \mathbf{A}\right)^{-1} \frac{1}{\Delta t}\boldsymbol{X}^{m-1} + \mathbf{B}\boldsymbol{V}_s^m\,, \\ \boldsymbol{I}_s^{m+\frac{1}{2}} &= \mathbf{C}\boldsymbol{X}^m + \mathbf{D}\boldsymbol{V}_s^m\,. \end{aligned} \tag{3.38}$$

When a choice has been made regarding the sampling of $\boldsymbol{V}_s(t)$ or the discretization method for the time derivative, this is applied to the SS schemes of both SA operators.

3.3.4 Combined Update Scheme

The combined update scheme in the lossy case is similar to that of the lossless case. A first difference is the use of c^v instead of α_C in the FDTD update equations. A second difference

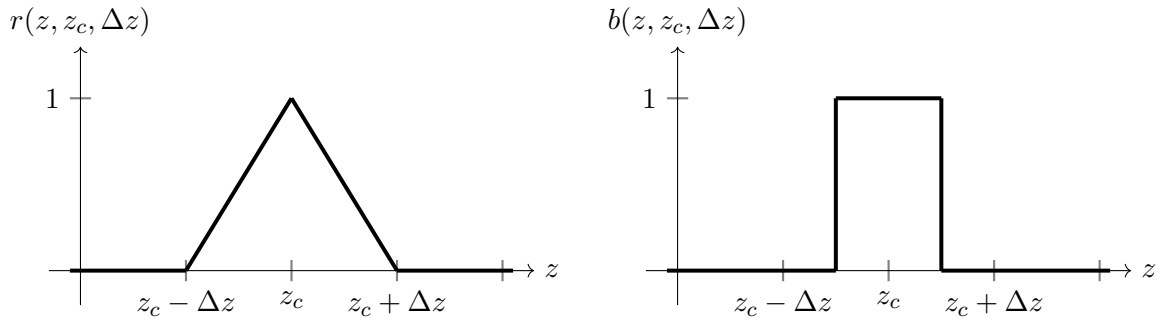

(a) The rooftop function.

(b) The pulse function.

Figure 3.2: The rooftop and pulse functions appearing in the basis- and test-functions, respectively. These are used to the derive the 1-D FCI-FDTD method. The function's first argument denotes the label of the horizontal axis. The second argument denotes the label of the central horizontal tick. The final argument denotes the distance between the ticks.

is that (3.32g) and (3.32h) are replaced by the update equations of both SA operators, e.g., in parallel. While they share the same input voltages, the output currents belong to each individual SA operator. In a following step, their difference computes the total VCCSs currents:

$$\boldsymbol{I}_s^{m+1/2} = \boldsymbol{I}_s^{m+1/2,\mathrm{b}} - \boldsymbol{I}_s^{m+1/2,\mathrm{a}} \,. \tag{3.39}$$

3.4 Lossless FCI-FDTD

3.4.1 Derivation

We apply the method using discrete zero-forms (scalars) by Tierens [7] on a 1-D region. Our starting point will be the lossless telegrapher's equations (2.15). Both currents and voltages are discretized on a uniform spatial grid with collocation in both space and time. As a result, we only need to derive a scheme for the first equation of (2.15). The approach for the second equation is entirely analogous. Consider the rooftop function

$$r\left(z, z_c, \Delta z\right) = \begin{cases} \frac{z - z_c}{\Delta z} + 1 & , \; z \in [z_c - \Delta z, z_c] \,, \\ 1 - \frac{z - z_c}{\Delta z} & , \; z \in [z_c, z_c + \Delta z] \,, \\ 0 & , \; \text{elsewhere,} \end{cases} \tag{3.40}$$

as shown in Figure 3.2a. The voltages and currents are expanded into these basis-functions of space and time. They are centered on a set of nodes of the space-time grid (z_n, t_m):

$$\begin{aligned} v(z,t) &= \sum_{m,n} V_n^m r(z, z_n, \Delta z) r(t, t_m, \Delta t) \,, \\ i(z,t) &= \sum_{m,n} I_n^m r(z, z_n, \Delta z) r(t, t_m, \Delta t) \,. \end{aligned} \tag{3.41}$$

The summations extend over all space and time coordinates. V_n^m and I_n^m are the grid voltages and grid currents, respectively. Consider now the pulse function

$$b\left(z, z_c, \Delta z\right) = \begin{cases} 1 & , \ z \in [z_c - \Delta z/2, z_c + \Delta z/2] \ , \\ 0 & , \ \text{elsewhere,} \end{cases} \tag{3.42}$$

as shown in Figure 3.2b. The expansions (3.41) are substituted in (2.15) and tested with pulse functions centered on another set of nodes of the space-time grid (z_k, t_l):

$$\begin{aligned} &\sum_{m,n} V_n^m \int \frac{\mathrm{d}}{\mathrm{d}z}\left[r(z, z_n, \Delta z)\right] b\left(z, z_k + \frac{\Delta z}{2}, \Delta z\right) \mathrm{d}z \int r(t, t_m, \Delta t) b\left(t, t_l + \frac{\Delta t}{2}, \Delta t\right) \mathrm{d}t \\ &= -\sum_{m,n} I_n^m \int L(z) r(z, z_n, \Delta z) b\left(z, z_k + \frac{\Delta z}{2}, \Delta z\right) \mathrm{d}z \int \frac{\mathrm{d}}{\mathrm{d}t}\left[r(t, t_m, \Delta t] \, b\left(t, t_l + \frac{\Delta t}{2}, \Delta t\right) \mathrm{d}t \, . \right. \end{aligned} \tag{3.43}$$

The integrals extend over all space or over all time. We now use the fact that

$$\frac{\mathrm{d}}{\mathrm{d}z} r(z, z_n, \Delta z) = \frac{1}{\Delta z}\left(b\left(z, z_n - \frac{\Delta z}{2}, \Delta z\right) - b\left(z, z_n + \frac{\Delta z}{2}, \Delta z\right)\right) , \tag{3.44}$$

to calculate the different integrals that appear in (3.43). These give rise to Kronecker delta terms in both space and time. They will eliminate the summations in space and time, respectively. What remains is a scheme that holds for all coordinates (z_k, t_l):

$$\begin{aligned} \frac{C_{n+\frac{1}{2}}\left(V_{n+1}^{m+1} + V_n^{m+1}\right)}{2\Delta t} + \frac{I_{n+1}^{m+1} - I_n^{m+1}}{2\Delta z} &= \frac{C_{n+\frac{1}{2}}\left(V_{n+1}^{m} + V_n^{m}\right)}{2\Delta t} - \frac{I_{n+1}^{m} - I_n^{m}}{2\Delta z} \, , \\ \frac{L_{n+\frac{1}{2}}\left(I_{n+1}^{m+1} + I_n^{m+1}\right)}{2\Delta t} + \frac{V_{n+1}^{m+1} - V_n^{m+1}}{2\Delta z} &= \frac{L_{n+\frac{1}{2}}\left(I_{n+1}^{m} + I_n^{m}\right)}{2\Delta t} - \frac{V_{n+1}^{m} - V_n^{m}}{2\Delta z} \, , \end{aligned} \tag{3.45}$$

where the second equation can be derived by analogy. In the above we made use of the regular averaging of the material parameters onto half-integer locations:

$$\begin{aligned} C_{n+\frac{1}{2}} &= \frac{C_n + C_{n+1}}{2} \, , \\ L_{n+\frac{1}{2}} &= \frac{L_n + L_{n+1}}{2} \, . \end{aligned} \tag{3.46}$$

It is clear that (3.45) is an implicit scheme, requiring us to solve a set of linear equations at each time step. We define

$$\boldsymbol{\alpha}_C^{\circ} = \begin{bmatrix} \alpha_{C,\frac{1}{2}} & \alpha_{C,\frac{1}{2}} & \cdots & \alpha_{C,\frac{1}{2}} \\ \alpha_{C,\frac{3}{2}} & \alpha_{C,\frac{3}{2}} & \cdots & \alpha_{C,\frac{3}{2}} \\ \vdots & \vdots & & \vdots \\ \alpha_{C,N-\frac{1}{2}} & \alpha_{C,N-\frac{1}{2}} & \cdots & \alpha_{C,N-\frac{1}{2}} \end{bmatrix}_{N\times N} \quad \text{and} \quad \boldsymbol{\alpha}_L^{\circ} = \begin{bmatrix} \alpha_{L,\frac{1}{2}} & \alpha_{L,\frac{1}{2}} & \cdots & \alpha_{L,\frac{1}{2}} \\ \alpha_{L,\frac{3}{2}} & \alpha_{L,\frac{3}{2}} & \cdots & \alpha_{L,\frac{3}{2}} \\ \vdots & \vdots & & \vdots \\ \alpha_{L,N-\frac{1}{2}} & \alpha_{L,N-\frac{1}{2}} & \cdots & \alpha_{L,N-\frac{1}{2}} \end{bmatrix}_{N\times N} . \tag{3.47}$$

We also define 1-D circulant averaging and difference incidence matrices as in [7, 8]. These are given by:

$$\mathbf{A}^{\circ} = \frac{1}{2}\begin{bmatrix} 1 & 1 & & & \\ & 1 & 1 & & \\ & & \ddots & & \\ & & & 1 & 1 \\ 1 & & & & 1 \end{bmatrix}_{N\times N} \quad \text{and} \quad \mathbf{D}^{\circ} = \begin{bmatrix} -1 & 1 & & & \\ & -1 & 1 & & \\ & & \ddots & & \\ & & & -1 & 1 \\ 1 & & & & -1 \end{bmatrix}_{N\times N} , \tag{3.48}$$

respectively. For each time step, the unknown variables V_n^m, I_n^m are collected across space in their respective column vectors, which we mark in italicized bold. The most natural terminal boundary conditions to implement are periodic boundary conditions (PBC). In this case (3.45) can be written as

$$\underbrace{\begin{bmatrix} \mathbf{A}^\circ & \frac{1}{2}\mathbf{D}^\circ \odot \boldsymbol{\alpha}_C^\circ \\ \frac{1}{2}\mathbf{D}^\circ \odot \boldsymbol{\alpha}_L^\circ & \mathbf{A}^\circ \end{bmatrix}}_{\mathbf{A}_{\mathrm{FCI,PBC}}} \begin{bmatrix} \boldsymbol{V}^{m+1} \\ \boldsymbol{I}^{m+1} \end{bmatrix} = \underbrace{\begin{bmatrix} \mathbf{A}^\circ & -\frac{1}{2}\mathbf{D}^\circ \odot \boldsymbol{\alpha}_C^\circ \\ -\frac{1}{2}\mathbf{D}^\circ \odot \boldsymbol{\alpha}_L^\circ & \mathbf{A}^\circ \end{bmatrix}}_{\mathbf{B}_{\mathrm{FCI,PBC}}} \begin{bmatrix} \boldsymbol{V}^{m} \\ \boldsymbol{I}^{m} \end{bmatrix}, \tag{3.49}$$

where $\odot$ denotes the Hadamard product. We now incorporate boundary conditions for the generator and load terminal networks described in Section 3.2.2. At each boundary we must enforce

$$I_0^m = \frac{E_g^m - V_0^m}{R_g} \quad \text{and} \quad I_N^m = \frac{V_N^m}{R_L}. \tag{3.50}$$

The currents are substituted in the update equations (3.45) at the terminals. Thereafter, they are not included in the column vector $\boldsymbol{I}^m$, reducing its size by two. In the following expressions, the superscript $^\square$ denotes the corresponding matrix with a superscript $\circ$ but with its last row omitted. The superscript $^\diamond$ denotes the corresponding matrix with a superscript $\circ$ but with the last row, the first column and the last column omitted. We define

$$\mathbf{L}^\square = \begin{bmatrix} 1 & 0 & & & \\ & 0 & & & \\ & & \ddots & & 0 \\ & & & 0 & 0 \end{bmatrix}_{(N-1)\times N} \quad \text{and} \quad \mathbf{R}^\square = \begin{bmatrix} 0 & 0 & & & \\ & 0 & & & \\ & & \ddots & & 0 \\ & & & 0 & 1 \end{bmatrix}_{(N-1)\times N}. \tag{3.51}$$

We also define $\mathbf{1}$ to be a column vector of all ones and size N. One can show that the equivalent of (3.49) for these terminal Impedance Boundary Conditions (IBC) is

$$\begin{aligned} \underbrace{\begin{bmatrix} \mathbf{A}^\square + \mathbf{L}^\square \frac{\alpha_{C,\frac{1}{2}}}{2R_g} + \mathbf{R}^\square \frac{\alpha_{C,N-\frac{1}{2}}}{2R_L} & \frac{1}{2}\mathbf{D}^\diamond \odot \boldsymbol{\alpha}_C^\diamond \\ \frac{1}{2}\mathbf{D}^\square \odot \boldsymbol{\alpha}_L^\square - \mathbf{L}^\square \frac{1}{2R_g} + \mathbf{R}^\square \frac{1}{2R_L} & \mathbf{A}^\diamond \end{bmatrix}}_{\mathbf{A}_{\mathrm{FCI,IBC}}} \begin{bmatrix} \boldsymbol{V}^{m+1} \\ \boldsymbol{I}^{m+1} \end{bmatrix} \\ = \underbrace{\begin{bmatrix} \mathbf{A}^\square - \mathbf{L}^\square \frac{\alpha_{C,\frac{1}{2}}}{2R_g} - \mathbf{R}^\square \frac{\alpha_{C,N-\frac{1}{2}}}{2R_L} & -\frac{1}{2}\mathbf{D}^\diamond \odot \boldsymbol{\alpha}_C^\diamond \\ -\frac{1}{2}\mathbf{D}^\square \odot \boldsymbol{\alpha}_L^\square - \mathbf{L}^\square \frac{1}{2R_g} + \mathbf{R}^\square \frac{1}{2R_L} & \mathbf{A}^\diamond \end{bmatrix}}_{\mathbf{B}_{\mathrm{FCI,IBC}}} \begin{bmatrix} \boldsymbol{V}^{m} \\ \boldsymbol{I}^{m} \end{bmatrix} \\ + \underbrace{\begin{bmatrix} \frac{\alpha_{C,\frac{1}{2}}}{2R_g}\mathbf{L}^\square & \frac{\alpha_{C,\frac{1}{2}}}{2R_g}\mathbf{L}^\square \\ \frac{1}{2R_g}\mathbf{L}^\square & -\frac{1}{2R_g}\mathbf{L}^\square \end{bmatrix}}_{\mathbf{C}_{\mathrm{FCI,IBC}}} \begin{bmatrix} \mathbf{1}E_g^m \\ \mathbf{1}E_g^{m+1} \end{bmatrix}. \end{aligned} \tag{3.52}$$

Given the update scheme (3.45), we now implement VCCSs feeding into the interfacial nodes of situation b. We will again only examine the behaviour at node $\mathcal{P}$. The exact position of the interface is also ambiguous. We will only examine the arbitrary choice of attaching the VCCS at the integer location $z = P\Delta z$. All material parameters belong to the central transmission line at this grid location. Similar notation is used as in Section 3.2.2. No averaging of the neighboring

nodes is necessary for the determination of $V_{\mathcal{P}}^m$. It is given by V_P^m. We rewrite (3.45) using spatial derivatives incorporating the correct infinitesimally adjacent currents. For $n = P-1$ we have:

$$\begin{aligned}
\frac{C_{P-\frac{1}{2}}\left(V_P^{m+1}+V_{P-1}^{m+1}\right)}{2\Delta t}+\frac{I_{P^-}^{m+1}-I_{P-1}^{m+1}}{2\Delta z}&=\frac{C_{P-\frac{1}{2}}\left(V_P^{m}+V_{P-1}^{m}\right)}{2\Delta t}-\frac{I_{P^-}^{m}-I_{P-1}^{m}}{2\Delta z}\,,\\
\frac{L_{P-\frac{1}{2}}\left(I_{P^-}^{m+1}+I_{P-1}^{m+1}\right)}{2\Delta t}+\frac{V_P^{m+1}-V_{P-1}^{m+1}}{2\Delta z}&=\frac{L_{P-\frac{1}{2}}\left(I_{P^-}^{m}+I_{P-1}^{m}\right)}{2\Delta t}-\frac{V_P^{m}-V_{P-1}^{m}}{2\Delta z}\,.
\end{aligned} \tag{3.53}$$

while for $n = P$ we have

$$\begin{aligned}
\frac{C_{P+\frac{1}{2}}\left(V_{P+1}^{m+1}+V_P^{m+1}\right)}{2\Delta t}+\frac{I_{P+1}^{m+1}-I_{P^+}^{m+1}}{2\Delta z}&=\frac{C_{P+\frac{1}{2}}\left(V_{P+1}^{m}+V_P^{m}\right)}{2\Delta t}-\frac{I_{P+1}^{m}-I_{P^+}^{m}}{2\Delta z}\,,\\
\frac{L_{P+\frac{1}{2}}\left(I_{P+1}^{m+1}+I_{P^+}^{m+1}\right)}{2\Delta t}+\frac{V_{P+1}^{m+1}-V_P^{m+1}}{2\Delta z}&=\frac{L_{P+\frac{1}{2}}\left(I_{P+1}^{m}+I_{P^+}^{m}\right)}{2\Delta t}-\frac{V_{P+1}^{m}-V_P^{m}}{2\Delta z}\,.
\end{aligned} \tag{3.54}$$

Enforcing KCL in the node (3.10) yields

$$I_{P^+}^m = I_{s\mathcal{P}}^m + I_{P^-}^m\,. \tag{3.55}$$

Similarly, we introduce the notation $I_{P^-} \triangleq I_P$. As a result, only the update equations (3.54) will be altered:

$$\begin{aligned}
\frac{C_{P+\frac{1}{2}}\left(V_{P+1}^{m+1}+V_P^{m+1}\right)}{2\Delta t}+\frac{I_{P+1}^{m+1}-I_P^{m+1}}{2\Delta z}-\frac{1}{2\Delta z}I_{s\mathcal{P}}^{m+1}&=\frac{C_{P+\frac{1}{2}}\left(V_{P+1}^{m}+V_P^{m}\right)}{2\Delta t}-\frac{I_{P+1}^{m}-I_P^{m}}{2\Delta z}+\frac{1}{2\Delta z}I_{s\mathcal{P}}^{m}\,,\\
\frac{L_{P+\frac{1}{2}}\left(I_{P+1}^{m+1}+I_P^{m+1}\right)}{2\Delta t}+\frac{V_{P+1}^{m+1}-V_P^{m+1}}{2\Delta z}+\frac{L_{P+\frac{1}{2}}}{2\Delta t}I_{s\mathcal{P}}^{m+1}&=\frac{L_{P+\frac{1}{2}}\left(I_{P+1}^{m}+I_P^{m}\right)}{2\Delta t}-\frac{V_{P+1}^{m}-V_P^{m}}{2\Delta z}+\frac{L_{P+\frac{1}{2}}}{2\Delta t}I_{s\mathcal{P}}^{m}\,.
\end{aligned} \tag{3.56}$$

Unlike the generator source, the VCCSs currents also depend on the voltages. Furthermore, these currents need to be known at time steps m and $m+1$ to compute the voltages. Therefore, the FCI-FDTD and SS scheme cannot be computed independently one after the other as in leapfrog FDTD. As a first approximation, we approximate $I_{s\mathcal{P}}^{m+1}$ by $I_{s\mathcal{P}}^m$. As such, the SS and FCI subsystems are updated one after the other as in Section 3.2.4. However, because this can reduce the accuracy significantly, we propose a solution without any approximations in the next section.

3.4.2 The State-Space Fully-Collocated Implicit FDTD Method

The State-Space Fully-Collocated Implicit FDTD (SS-FCI-FDTD) method performs implicit time-stepping as a combination of both schemes. We define the following matrices having nonzero elements on rows P and Q

$$\mathbf{S}_1 = \begin{matrix} \\ P \\ Q \end{matrix}\!\!\begin{bmatrix} 1 & \\ & \\ & 1 \end{bmatrix} \in \mathbb{R}^{(N-1)\times 2} \quad \text{and} \quad \mathbf{S}_L = \begin{matrix} \\ P \\ Q \end{matrix}\!\!\begin{bmatrix} L_{P+\frac{1}{2}} & \\ & \\ & L_{Q-\frac{1}{2}} \end{bmatrix} \in \mathbb{R}^{(N-1)\times 2}\,. \tag{3.57}$$

Using these in block matrices, the VCCSs terms appearing in (3.56) can be added to (3.52):

$$\begin{aligned}\mathbf{A}_{\text{FCI,IBC}} \begin{bmatrix} \boldsymbol{V}^{m+1} \\ \boldsymbol{I}^{m+1} \end{bmatrix} + \begin{bmatrix} \mathbf{0} & -\frac{\mathbf{S}_1}{2\Delta z} \\ \mathbf{0} & \frac{\mathbf{S}_L}{2\Delta t} \end{bmatrix} \begin{bmatrix} \boldsymbol{X}^{m+1} \\ \boldsymbol{I}_s^{m+1} \end{bmatrix} \\ = \mathbf{B}_{\text{FCI,IBC}} \begin{bmatrix} \boldsymbol{V}^{m} \\ \boldsymbol{I}^{m} \end{bmatrix} + \begin{bmatrix} \mathbf{0} & \frac{\mathbf{S}_1}{2\Delta z} \\ \mathbf{0} & \frac{\mathbf{S}_L}{2\Delta t} \end{bmatrix} \begin{bmatrix} \boldsymbol{X}^{m+1} \\ \boldsymbol{I}_s^{m+1} \end{bmatrix} + \mathbf{C}_{\text{FCI,IBC}} \begin{bmatrix} \mathbf{1}E_g^{m} \\ \mathbf{1}E_g^{m+1} \end{bmatrix}.\end{aligned} \tag{3.58}$$

Unlike previous SS implementations, the state-space scheme must output VCCSs currents at time steps $m+1$. Therefore, new state-space schemes must be derived for different evaluation points and discretizations of the time derivative. We will only consider the evaluation point $m+1$ for both equations of (3.24) and use the BE method. This yields the following SS scheme:

$$\begin{aligned}\mathbf{M}_1 \boldsymbol{X}^{m+1} &= \mathbf{M}_2 \boldsymbol{X}^{m} + \mathbf{B}\boldsymbol{V}_s^{m+1}, \\ \boldsymbol{I}_s^{m+1} &= \mathbf{C}\boldsymbol{X}^{m+1} + \mathbf{D}\boldsymbol{V}_s^{m+1},\end{aligned} \tag{3.59}$$

where we defined

$$\begin{aligned}\mathbf{M}_1 &= \left(\frac{1}{\Delta t}\mathbb{I}_{n_x} - \mathbf{A}\right), \\ \mathbf{M}_2 &= \frac{1}{\Delta t}\mathbb{I}_{n_x}.\end{aligned} \tag{3.60}$$

The voltages controlling the VCCSs can be extracted from the vector containing all grid voltages:

$$\boldsymbol{V}_s^{m+1} = \mathbf{S}_1^T \boldsymbol{V}^{m+1}. \tag{3.61}$$

We can rewrite (3.59) by using this relation and reordering terms:

$$\begin{aligned}-\mathbf{B}\mathbf{S}_1^T \boldsymbol{V}^{m+1} - \mathbf{M}_1 \boldsymbol{X}^{m+1} &= \mathbf{M}_2 \boldsymbol{X}^{m}, \\ -\mathbf{D}\mathbf{S}_1^T \boldsymbol{V}^{m+1} - \mathbf{C}\boldsymbol{X}^{m+1} + \boldsymbol{I}_s^{m+1} &= \mathbf{0}_2.\end{aligned} \tag{3.62}$$

In the above we used the definition for $\mathbf{0}_n$: an all zero column vector of size n. When juxtaposing (3.62) with (3.58), a fully implicit scheme incorporating the SS and FCI scheme can clearly be constructed using a state-vector containing all variables:

$$\begin{aligned}\left[\begin{array}{c|cc} \mathbf{A}_{\text{FCI,IBC}} & -\frac{\mathbf{S}_1}{2\Delta z} & \\ & \frac{\mathbf{S}_L}{2\Delta t} & \\ \hline -\mathbf{B}\mathbf{S}_1^T & \mathbf{M}_1 & \\ -\mathbf{D}\mathbf{S}_1^T & -\mathbf{C} & \mathbb{I}_2 \end{array}\right] \begin{bmatrix} \boldsymbol{V}^{m+1} \\ \boldsymbol{I}^{m+1} \\ \boldsymbol{X}^{m+1} \\ \boldsymbol{I}_s^{m+1} \end{bmatrix} = \left[\begin{array}{c|c} \mathbf{B}_{\text{FCI,IBC}} & \frac{\mathbf{S}_1}{2\Delta z} \\ & \frac{\mathbf{S}_L}{2\Delta t} \\ \hline & \mathbf{M}_2 \end{array}\right] \begin{bmatrix} \boldsymbol{V}^{m} \\ \boldsymbol{I}^{m} \\ \boldsymbol{X}^{m} \\ \boldsymbol{I}_s^{m} \end{bmatrix} \\ + \left[\begin{array}{c|c} \mathbf{C}_{\text{FCI,IBC}} & \\ & \\ \hline & \end{array}\right] \begin{bmatrix} \mathbf{1}E_g^{m} \\ \mathbf{1}E_g^{m+1} \\ \mathbf{0}_{n_x} \\ \mathbf{0}_2 \end{bmatrix}.\end{aligned} \tag{3.63}$$

In the above block matrices, empty entries are appropriately sized all zero matrices.

Chapter 4

Results and Discussion

4.1 Methods

4.1.1 Stability

Every proposed scheme in this thesis steps through time in iterations. In each iteration, the number of unknowns does not change. The unknowns in the m^{th} iteration are collected in a column vector $\boldsymbol{U}^m$. As all schemes are linear, there exists a constant amplification matrix $\mathbf{G}$ such that

$$\boldsymbol{U}^{m+1} = \mathbf{G}\boldsymbol{U}^m + \boldsymbol{S}^m \,, \tag{4.1}$$

where $\boldsymbol{S}^m$ is a column vector containing elements originating from the generator source. This LTI system is exponentially stable if and only if none of the eigenvalues of $\mathbf{G}$ lie outside the unit circle. The matrix $\mathbf{G}$ is extracted directly from the implementation using Van Londersele's approach [8, p. 132]. Here, each column of $\mathbf{G}$ is populated by the unknowns produced after an iteration (such as, e.g., (3.32)), when only one unknown element is set to one. Note that $\mathbf{G}$ can also directly be constructed from the mathematical update equations in an iteration. However, this method is more prone to oversight during the derivations. Also, it may not capture the machine precision errors made during the updating, which need to be taken into account. We can study the stability of the SS scheme independently by only including $\boldsymbol{X}^{\text{prev}}$ and $\boldsymbol{I}_s^{\text{prev}}$ in $\boldsymbol{U}^m$. The associated ampliciation matrix is denoted $\mathbf{G}_{SS}$.

An eigenvalue λ with the largest complex modulus $|\lambda| = \rho$ (the spectral radius) determines the stability of the scheme. For an associated eigenvector $\boldsymbol{P}^m$ we have

$$\mathbf{G}\boldsymbol{P}^m = \lambda \boldsymbol{P}^m \,. \tag{4.2}$$

The source term $\boldsymbol{S}^m$ can be ignored without loss of generality. Using (4.1) we find

$$\boldsymbol{P}^{m+1} = \lambda \boldsymbol{P}^m \,. \tag{4.3}$$

The case of maximal growth is obtained when $\boldsymbol{P}^{m+1}$ belongs to the same eigenspace as $\boldsymbol{P}^m$. In this case, the modulus of the entries grow as ρ^M, where M is the number of iterations. Results

suggest it is safe to assume $\boldsymbol{P}^m$ is excited at least at one point during the simulation. Moreover, it constitutes a worse-case scenario. When $\rho > 1$, entries of $\boldsymbol{P}^m$ will dominate those of $\boldsymbol{U}^m$ as m goes to infinity. Let $t_{\text{tot}} = M\Delta t$ be the total simulation time. In this time, entries of $\boldsymbol{U}^m$ have a growth g that is bounded by

$$g \geq (1+\xi)^{t_{\text{tot}}/\Delta t} \,, \tag{4.4}$$

where we introduced $\xi = \rho - 1$. Assuming $g > 0$, (4.4) can be rewritten as

$$t_{\text{tot}} \leq \frac{\ln(g)\Delta t}{\ln(1+\xi)} \approx \frac{\ln(g)\Delta t}{\xi} \,. \tag{4.5}$$

Assuming ξ is small, a first-order series expansion can be used to obtain

$$\xi \leq \frac{\ln(g)\Delta t}{t_{\text{tot}}} = \xi_{\max} \,. \tag{4.6}$$

This provides us with a maximal value for $\xi_{\max}$ that produces acceptable late time unstable simulations. The influence of Δt and t_{tot} is much larger than of the maximally acceptable growth[1]. The former two vary by application area and type of simulation. For our simulations, the smallest Δt and largest t_{tot} are in the order of $10^{-13}\,\text{s}$ and $10^{-7}\,\text{s}$, respectively. Therefore, we call simulations *practically stable* when $\log(\xi) < -6$ in this text. This means no exponential growth will be noticeable in any of the performed simulations. In general, M is much smaller than reported above. Thus, simulations are still useable until approximately $\log(\xi) = -3.5$. We call the stability of simulations with $-6 < \log(\xi) < -3.5$ *limited*. Many applications post-process time domain signals to the frequency domain. Here, it is favorable to require the signals to taper to zero. Exponential growth over multiple orders of magnitude is then acceptable. This is because the signal can be cut off when the instability becomes comparable to the signal maximum. Some applications may require t_{tot} to be long. For example, as Chilton and Lee note: "a large cavity with two resonant modes closely spaced in frequency would need a long true-time response to distinguish the two modes in the frequency domain" [44, p. 8]. Other applications may require a significantly smaller time step, although the number of time steps is the limiting parameter.

4.1.2 Parametrization

For the implementations with lossless leapfrog and FCI-FDTD, the material parameters of the central transmission line of situation a are arbitrarily chosen as

$$Z_1 = 100\,\Omega \quad , \quad k_1 = \sqrt{4.2}\,\frac{\omega}{c} \,, \tag{4.7}$$

For the implementation with lossy leapfrog, the material parameters are chosen more realistically from a coaxial TSV described by Xu and Lu [24]. We highlight their use of copper with $\sigma = 5.9 \times 10^7\,\text{S}\,\text{m}^{-1}$ as conductive core. Among the parameters is also the loss tangent of the dielectric, which was assumed frequency independent. Note that a realistic loss tangent changes significantly with frequency [45, 46]. As explained in Section 2.3, parameters for a

[1] Larger growths g are acceptable if the signals are zero to machine precision or close to it in the late time.

non-dispersive model are sampled on a specific frequency ω' from the dispersive counterpart. We choose $\omega' = 4.571\,\mathrm{GHz}$, as it provides the best fit of the DSA operator with respect to the dispersive model in the range [0 Hz, 7.5 GHz] (see below). For all implementations, the material parameters of the other transmission lines are chosen as

$$Z_0 = 50\,\Omega \quad , \quad k_0 = \frac{\omega}{c}\,. \tag{4.8}$$

The (differential) SA operator(s) can now be parametrized based on the above wavenumbers. As explained in Section 2.5, we focus on short transmission lines. We always vector fit in a frequency range from DC to the lossless resonant frequency corresponding to $k_0 d = \pi$. This range includes the lossless resonant frequency corresponding to $k_1 d = \pi$. We choose d equal for all simulations, enabling a better comparison between the different implementations. A value of 2 cm sets the limit on the frequency range to 7.5 GHz. This limit allows us to easily probe results of models beyond the maximal fitted frequency. Note that transmission lines used in integrated circuits are orders of magnitudes smaller, resulting in orders of magnitudes higher achievable frequencies[2]. On the contrary, the necessarily smaller Δt reduces $\log(\xi_{\max})$, for constant t_{tot}.

We continue with the remaining parameters outside the central transmission line. The lengths of the left and right transmission lines are chosen to be 5 cm and 7 cm, respectively. The generator and load resistors R_g and R_L are matched to their adjacent transmission line, i.e., they are both $50\,\Omega$. As no reflections occur at the load, $B = 0$ in (3.3). Therefore, $\hat{v}(z)$ and $\hat{\imath}(z)$ are identical up to a factor, as are their time domain counterparts. For the right transmission line, only the voltages are studied as a function of time for this reason. We limit ourselves to an analysis as a function of time on a position 1 cm to the right of $\mathcal{Q}$ (the *recorder* position).

The FDTD discussion of Section 2.4 can be summarized by the following formulae:

$$\begin{aligned} \Delta z &= \left(\frac{1}{f_{\max} N_\lambda}\right) v_{\min}\,, \\ \Delta t &= \left(\frac{\alpha_{\mathrm{Courant}}}{f_{\max} N_\lambda}\right) \frac{v_{\min}}{v_{\max}}\,. \end{aligned} \tag{4.9}$$

The variables appearing in parentheses constitute choices that are free within a given range:

$$\begin{aligned} 0 < \alpha_{\mathrm{Courant}} &< 1\,, \\ f_{\max} &\gtrsim 7.5\,\mathrm{GHz}\,, \\ N_\lambda &\gtrsim 10\,. \end{aligned} \tag{4.10}$$

The symbol $\gtrsim$ indicates the parameter is ideally chosen higher than its lower bound. Throughout this chapter, we provide a stability analysis as a function of possible choices. However, good

[2] It is required to model frequencies up to 100 GHz to take into account the harmonics appearing in ICs with clock speeds of several gigahertz.

choices follow from the source's maximal frequency and required accuracy [27, 28] of the specific application, along with the available computational budget. As the influence of $f_{\max}$ and N_λ is clearly identical, we will only vary N_λ and α_{Courant}. No application should require $f_{\max}$ higher than the BW of VF, as the accuracy becomes poor. Therefore, $f_{\max}$ is set conservatively to $f_{\max} = 10\,\text{GHz}$, sufficient for any source. This parameter is maintained for every simulation in this chapter.

Colored contour plots are shown in multiple figures of this chapter. The stability measure $\log(\xi)$ is computed for different amplification matrices. These depend on different free choices and free parameters. Free choices are the nature of the (sub)system being analyzed or the choices taken to construct the SS scheme. These are specified in the figure caption. Free parameters are α_{Courant} and N_λ. These are specified by the center of the colored square in the plot. The former is placed on the horizontal axis, the latter on the vertical axis. From (4.9), we find that horizontal lines represent simulations of constant Δz. Furthermore, diagonal lines through the origin represent simulations of constant Δt. When $\xi < 0$, the system is exponentially stable. These points are represented in green. When $\xi = 0$, the system is not necessarily Lyapunov stable. See [8, p. 68] and [47] for more information. These points are represented in white. Yellow and light blue colors denote practically stable simulations until $\log(\xi) = -6$. A discontinuous change in color from light to dark blue indicates the limit $\log(\xi) = -3.5$. Beyond these values, the instability grows too fast to extract any useful results. This is shown by dark blue, red or black colors. Note that while this classification is presented as discrete, the measure of (in)stability is a continuous parameter.

4.1.3 Computational Methods

As all the obtained VF models have a low n_x (48 is the largest among all models), expressions involving matrices $\mathbf{A}$, $\mathbf{B}$, $\mathbf{C}$ $\mathbf{D}$, $\mathbb{I}_{n_x}$ and $\mathbb{I}_2$ can be inverted with negligibly small computational costs. Therefore, matrix inversions are used, which were not singular in any of the schemes employed in this chapter. When a matrix system involves $\mathbf{A}_{\text{FCI,IBC}}$ and $\mathbf{B}_{\text{FCI,IBC}}$, using matrix inversion is not appropriate. The number of nonzero entries, the number of entries and their quotient are in the order of 10^4, 10^6 and 1%, respectively. Therefore, a sparse solver is more efficient in computing solutions for these matrix systems. The number of unknowns is low enough to use a direct solver. Iterative solvers would be more suited if this is not the case, e.g., if the problem is considered in a large 2-D or 3-D simulation space. The former guarantees a solution accurate within machine precision, while the latter does not. This improves our ability to study the influence of machine precision rounding on stability. Late-time instabilities in time domain methods can occur as a consequence of rounding errors of both direct and iterative solvers [44, 48]. A LU factorization is used as preconditioner immediately after the initialization of these larger matrices, improving the efficiency of the calculations during updating.

Simulations were performed on a 64-bit Windows machine using the Intel Core i5-6200U CPU at 2.3 GHz and 16 GB of installed RAM. The time spent on operations relevant to the SS model is negligible with respect to the time spent on FDTD or FCI-FDTD operations. A well-

developed skin effect is never created in this work to the extent that the simulation a becomes computationally expensive. The majority of simulations did not exceed a total run-time of 3 min. As a result, we do not extensively report on the computational costs. We do however note the generally faster execution of the simulation pertaining to situation b. This is due to the increased $v_{\min}$ when the material of situation a is abstracted.

4.1.4 Error metrics

Consider two simulation labeled 1 and 2. Quantities with these subscripts indicate the corresponding simulation they belong to. We want to express the error between the transients $V^m_{R_1,1}$ and $V^m_{R_2,2}$ at the same recorder position $z \approx R_1\Delta z_1 \approx R_2\Delta z_2$. Let $M = \min(M_1, M_2)$. We define:

$$\begin{aligned} v_1(t) &= \sum_{m=0}^{M} V^m_{R_1,1} r(t, m\Delta t_1, \Delta t_1)\,, \\ v_2(t) &= \sum_{m=0}^{M} V^m_{R_2,2} r(t, m\Delta t_2, \Delta t_2)\,. \end{aligned} \tag{4.11}$$

For these transients, we define the following error metric up to the total simulation time $t_{\max}$:

$$\mathrm{SRMSE}_{t_{\max}} = \frac{\sqrt{\int_0^{t_{\max}} \left(v_1(t) - v_2(t)\right)^2 \mathrm{d}t}}{\sqrt{\int_0^{t_{\max}} v_1(t)^2 \mathrm{d}t}}\,, \tag{4.12}$$

which is easily interpretable, not directly dependent on M or $t_{\max}$ and punishes outliers. The mean value theorem for definite integrals reveals that (4.12) corresponds to the Root Mean Squared Error (RMSE) normalized with the Root Mean Square (RMS)[3] of the reference signal. This justifies our denomination Scaled RMSE (SRMSE).

We will also compare the real parts of transfer functions of both situations. These signals $\hat{t}_1(f)$ and $\hat{t}_2(f)$ are similarly interpolated in the frequency domain as in (4.11). A more interpretable normalization is through the range of the reference signal, as the amplitude of $\hat{v}_1(f)$ weakly depends on frequency. This error metric carries the name Normalized RMSE (NRMSE). In the bandwidth of interest BW, it equals

$$\mathrm{NRMSE}_{\mathrm{BW}} = \frac{\sqrt{\int_{\mathrm{BW}} \left(\hat{t}_1(f) - \hat{t}_2(f)\right)^2 \mathrm{d}f}}{\max\left(\hat{v}_1(f \in \mathrm{BW})\right) - \min\left(\hat{v}_1(f \in \mathrm{BW})\right)}\,, \tag{4.13}$$

We want to quantify the error between the fitted and analytical (differential) SA operator(s). A high dynamic range as function of frequency is observed in the operators' entries, resulting from their resonance peaks. Therefore, expressing their error as one number is not informative.

[3] This coincides with the standard deviation as the mean of $v_1(t)$ is approximately zero in all our results.

Instead, the Frobenius Mean (FM) of the analytical and vector fitted (differential) SA operator(s)

$$\mathrm{FM}_{\hat{\mathbf{Y}}}(f) = \frac{1}{\sqrt{4}} \left\| \hat{\mathbf{Y}}(f) \right\|_F \quad \text{and} \quad \mathrm{FM}_{\widetilde{\mathbf{Y}}}(f) = \frac{1}{\sqrt{4}} \left\| \widetilde{\mathbf{Y}}(f) \right\|_F , \tag{4.14}$$

are plotted as a function of frequency. $\|\cdot\|_F$ denotes the Frobenius norm. The factor $\frac{1}{\sqrt{4}}$ normalizes the norm with respect to the number of entries. Hence, the FM of a matrix is easily interpreted as an average absolute value of the matrix entries skewed towards the larger entries. The Relative Frobenius Error (RFE)

$$\mathrm{RFE}(f) = \frac{\left\| \hat{\mathbf{Y}}(f) - \widetilde{\mathbf{Y}}(f) \right\|_F}{\left\| \hat{\mathbf{Y}}(f) \right\|_F} , \tag{4.15}$$

is superimposed on these plots. The numerator expresses error as is usual in the literature [49, 50] and takes phase differences into account. The Frobenius norm causes the denominator to rarely be zero.

4.1.5 General Approach

The number of free choices (including free parameters) is too large to allow for a full multivariate analysis. Therefore, we will often limit ourselves to a comprehensive walk through the various possibilities. Explanations are provided when possible for the observations. Conclusions of these guide the discussion towards interesting choices. They will also justify the introduction of the different implementations in Chapter 3. The optimal methods to represent conclusions will evolve as we learn more and more funded hypotheses. These methods include

- analyses of the VF error,
- stability analyses of different subsystems for a range of free parameters,
- accuracies of the results in the time and frequency domain.

We are driven by the goal to obtain both stable and accurate simulations while also proving practical relevance by realistic examples. The results are concluded together with the impementations in Chapter 5. In general, an expert cannot immediately create a VF model while guaranteeing low errors and passivity. Therefore, observing results across a set of, e.g., 1000 different VF models is not feasible. Such an analysis could, e.g., indicate the importance of the VF error with respect to inaccuracies produced by the schemes themselves.

4.2 Lossless Leapfrog

The lossless leapfrog implementation employs the DSA operator of a lossless situation a and b. As explained, the VF procedure experienced difficulties in imposing passivity on a marginally passive system. First, this manifests itself in a reduced accuracy in highly dynamic regions, as shown in Figure 4.1. The RFE is 95% near 7.3 GHz. In less dynamic regions, the FRE is less than 3%. Second, while all poles p_i in (3.1) are located in the left half-plane, the pole closest

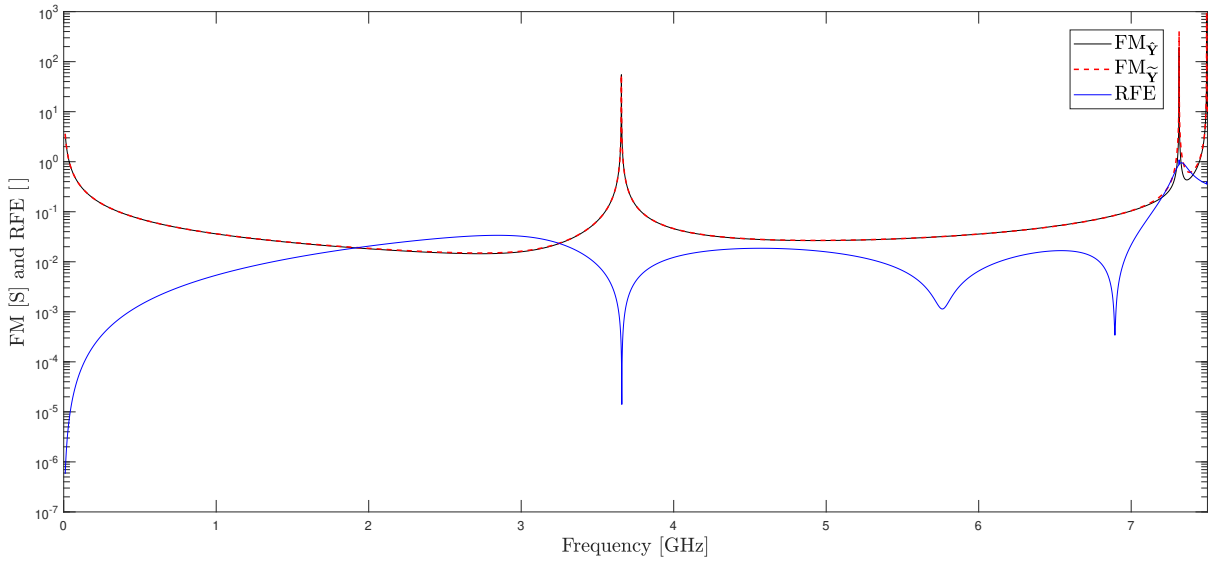

Figure 4.1: This plot shows the analytical DSA operator, its vector fitted counterpart and the error between them. Only the fitted range is shown, after which the accuracy becomes poor. The definition of the FM and FRE metrics are explained in Section 4.1.4.

to the imaginary axis equals -1.21×10^{-6}. Therefore, the condition number of $\mathbf{A}$ is 4×10^{20}, which is very high.

Seven SS discretization schemes were proposed in Appendix B. However, we limit ourselves to those that do not require inverting block matrices. Three schemes remain. The sampling choice causes the number of available schemes to multiply to six.

We examine the SS subsystem first. From a physical point of view, we expect $\xi = 0$. Therefore, the lossless case constitutes an edge case where guaranteeing stability is most precarious. Whenever the BE method is used, ξ is zero for all α_{Courant} and N_λ. Whenever the TR method is used, ξ is zero in the majority of simulations. Occasionally, we find $\xi = k\varepsilon$. Here, k is a small positive or negative integer and $\varepsilon = 1.11 \times 10^{-16}$, the machine epsilon value for double-precision floating-point numbers. There appears to be no meaningful pattern as a function of α_{Courant} and N_λ. An example of this behavior is shown in Figure 4.2. We provide the following hypothesis to explain this phenomenon. Consider the matrix appearing in the SS update equations (B.3) with the TR method:

$$\left(\frac{\mathbb{I}_{n_x}}{\Delta t} - \frac{\mathbf{A}}{2}\right)^{-1} \left(\frac{\mathbb{I}_{n_x}}{\Delta t} + \frac{\mathbf{A}}{2}\right) . \tag{4.16}$$

Poles λ_c of the continuous system $\mathbf{A}$ are mapped to eigenvalues λ_d of the discrete scheme as

$$\lambda_d = \frac{\frac{1}{\Delta t} + \frac{\lambda_c}{2}}{\frac{1}{\Delta t} - \frac{\lambda_c}{2}} . \tag{4.17}$$

One can show that $|\lambda_d| < 1$ if $\text{Re}\{\lambda_c\} < 0$. The irregular violations of this suggest that inexact arithmetic causes poles λ_c with a small real part to be mapped to just outside the unit circle.

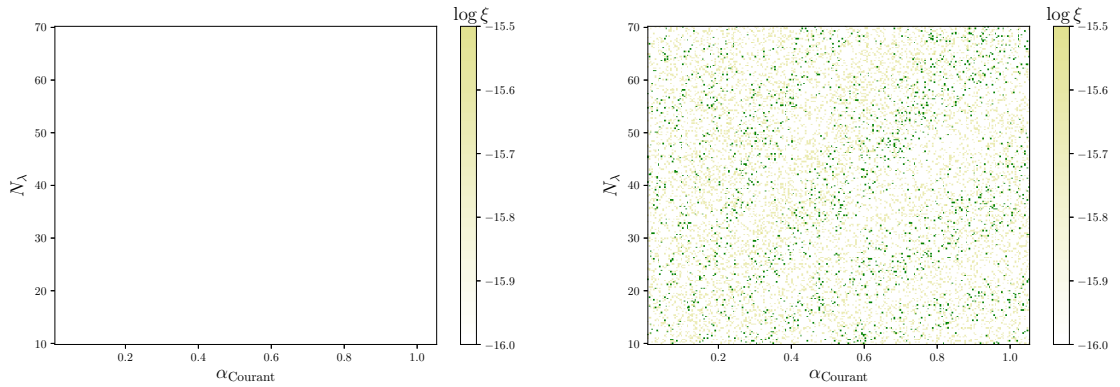

(a) The evaluation points m and m are used with the BE method.

(b) The evaluation points m and $m+1/2$ are used with the TR method.

Figure 4.2: Stability analysis of the lossless SS subsystem. The analysis is incomplete as only the BE and TR method play a role here. For clarity, color saturation is increased and the range is decreased compared to other contour plots. The lossless DSA operator is used. Clarification of these plots is given in Section 4.1.2.

We observe that computing (4.17) with double-precision floating-point numbers sometimes leads to $|\lambda_d| = 1 + \varepsilon > 1$, even though $\mathrm{Re}\{\lambda_c\} < 0$. The mapping corresponding to the BE method

$$\lambda_d = \frac{\frac{1}{\Delta t}}{\frac{1}{\Delta t} - \lambda_c}\,, \tag{4.18}$$

has not been observed to yield $|\lambda_d| > 1$. The region of absolute stability of the TR method is the left half-plane [42]. For the BE method, it is the complement of the disk of radius 1 and center at 1, granting it the L-stable property. It is therefore more suited for the modeling of stiff ODEs with eigenvalues very close to the imaginary axis. Furthermore, L-stability damps out the well-known spurious oscillations occurring in the Crank-Nicolson scheme [51, 52].

Consider, as an intermediate step, situation b where the VCCSs do *not* feed into the computational domain, i.e., they are inactive. We can predict the stability of this scheme when interfacial voltages are chosen as V_P and V_Q. This follows from Theorem 2 of [40] when the supply rate and storage function of the SS system is included, as shown in Appendix C. As previously explained, the spectral radius of the SS scheme with the BE method is never greater than one. Therefore, we expect the full system to be stable if the Courant limit is not violated. This is clearly the case, as shown in Figure 4.3(a). When the TR method is used, the SS system occasionally has a spectral radius larger than one to within machine precision. This influences ξ values of the total scheme, but now uniformly for all N_λ and α_{Courant} that do not break the Courant limit. Similar results hold when the sampling choice or evaluation points are different.

Let us now consider the case where the VCCSs do feed into the computational domain. The proof provided in Appendix C does not hold anymore. The interconnecting topology is different as the input of the TL2 subsystem now includes the output of the SS system. These appear

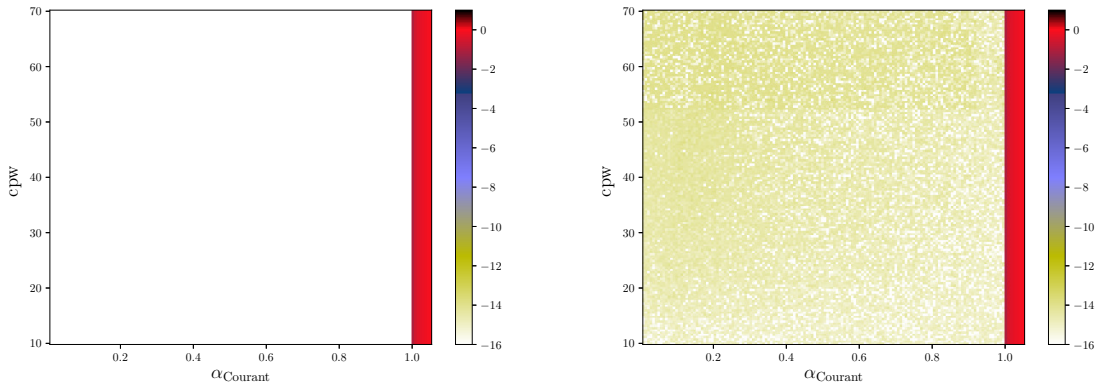

(a) With the BE method.

(b) With the TR method.

Figure 4.3: Stability analysis of the lossless full system. The VCCSs do not feed into the computational domain. The analysis is incomplete. First, evaluation points m and m are used. Second, the VCCSs voltages are sampled on locations $z = P\Delta z$ and $z = Q\Delta z$. The lossless DSA operator is used. Clarification of these plots is given in Section 4.1.2.

in the form of VCCSs terms in the leapfrog FDTD update equations. Such interconnections do not fall under the definition used in [40]. The total system is not necessarily passive[4]. Deriving strict bounds on free parameters to ensure passivity remains an open question. We now continue with observing the stability for different free choices. This is shown in Figure 4.4. The experimentally observed growth rate of $V^m_{R_b,b}$ closely matches those predicted by (4.6) when $\log(\xi) > -6$. The number of steps N required to notice significant growth for $-6 > \log(\xi) > -16$ is too large to compute in a reasonable amount of time. Unsurprisingly, violating the Courant limit $\alpha_{\text{Courant}} > 1$ immediately causes highly unstable simulations. The BE method shows larger regions with improved stability compared to the TR method. The latter generally has a region of limited stability for low time steps. For the former, an intricate pattern is seen when the VCCSs voltages are averaged over the interface, as shown in Figure 4.4(a). For sufficiently high time steps, stability can change from practically stable to unstable when α_{Courant} or N_λ change by less approximately 0.05%, respectively. Specific values of Δz values cause the stability to break down. Moreover, using a differently vector fitted DSA operator[5] did not reproduce the results. Machine precision errors and the inexact length $d \approx k\Delta z$, with k an integer, are believed to play an important role in the stability of some schemes. The first is motivated by the discussion of the stability when the VCCSs do not feed into the computational domain. In addition, switching from double-precision floating-point numbers in the implementation to single-precision caused a different irregular pattern of $\xi > 0$ occurring. The second is a conjecture founded on the different stabilities observed when Δz. Furthermore, the length of the central medium is not well resolved for low N_λ. The error $|d - k\Delta z|/d$ can be $\pm 6.3\%$ when $N_\lambda = 10$. If these reasons are correct, the derivation of strict bounds on stability is elusive as taking these into account is

[4]To illustrate this, consider the cascade connection of two passive subsystems. The total system is not necessarily passive [53].

[5]The number of poles was increased from 16 to 23. The eigenvalue with the highest real part decreased from -1.21×10^{-6} to -7.14×10^{-9}.

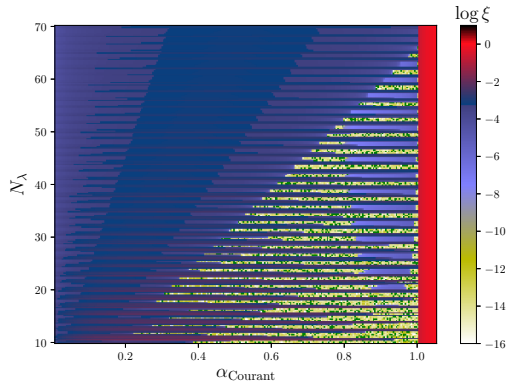

(a) The VCCSs voltages are sampled by averaging over the interface. The evaluation points m and m are used with the BE method.

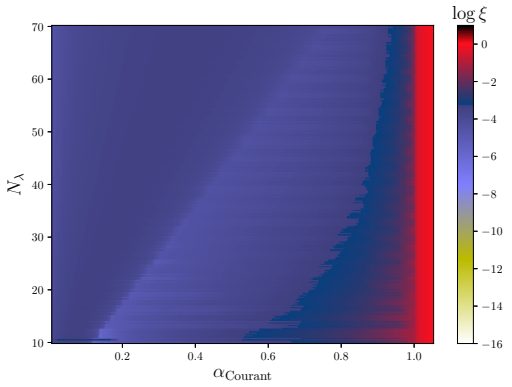

(b) The VCCSs voltages are sampled on $z = P\Delta z$ and $z = Q\Delta z$. The evaluation points m and m are used with the BE method.

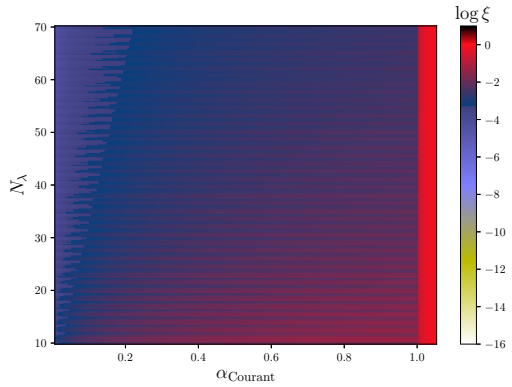

(c) The VCCSs voltages are sampled by averaging over the interface. The evaluation points m and m are used with the TR method.

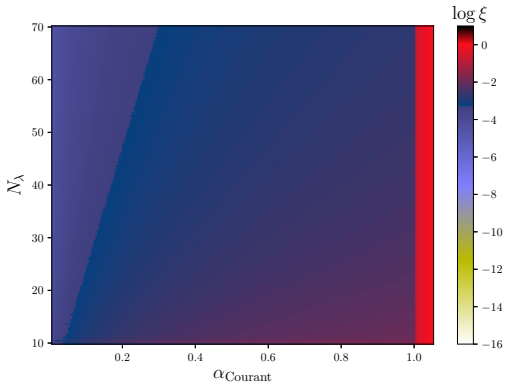

(d) The VCCSs voltages are sampled on $z = P\Delta z$ and $z = Q\Delta z$. The evaluation points m and m are used with the TR method.

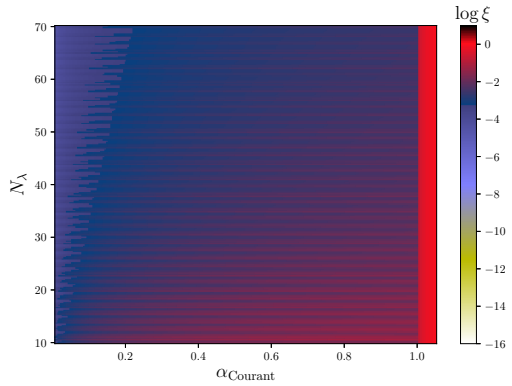

(e) The VCCSs voltages are sampled by averaging over the interface. The evaluation points m and $m + 1/2$ are used with the TR method.

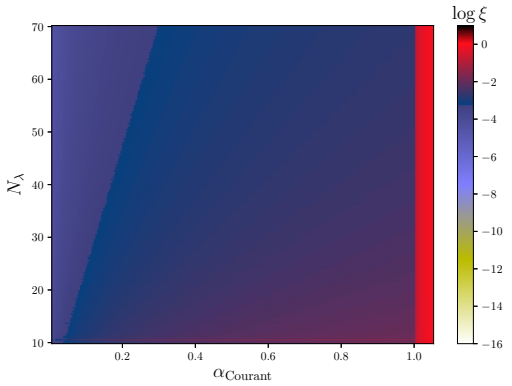

(f) The VCCSs voltages are sampled on $z = P\Delta z$ and $z = Q\Delta z$. The evaluation points m and $m + 1/2$ are used with the TR method.

Figure 4.4: A complete stability analysis of the lossless full system. The VCCSs do feed into the computational domain. The lossless DSA operator is used. Clarification of these plots is given in Section 4.1.2.

not trivial.

We now study the accuracy of our implementations in the time domain. This is the most natural domain to express accuracy in as FDTD is first and foremost a time domain method. Analyzing the accuracy of the full system as function of α_{Courant} and N_λ is difficult because stability is not always guaranteed. Therefore, only the influence of frequency on the SRMSE between situation a and b is examined. This is done for a practically or limited stable combination of α_{Courant} and N_λ. Gaussian pulses modulated at a frequency f_c and shifted in time by 5σ are used as generator sources:

$$e_g(t) = \sin\left(2\pi f_c(t-5\sigma)\right) \exp\left(-\frac{(t-5\sigma)^2}{2\sigma^2}\right), \tag{4.19}$$

where σ is chosen as $5 \times 10^{-9}\,\text{s}^{-1}$. As a result, 99.7% of the spectral content is contained within the bandwidth $[f_c \pm 95.5\,\text{MHz}]$. This small bandwidth allows us to study the accuracy of the model at f_c. This modulation frequency f_c is varied from near DC to 7.5 GHz. Two sources of error are present: from the FDTD subsystem and from the SS subsystem. The first has its dispersion error minimized for α_{Courant} just below 1. Second-order accuracy in space causes increasing N_λ to improve accuracy. The error introduced by the SS approach is visually compared with the error that naturally occurs as a result of the FDTD scheme. The latter is computed using a reference simulation. The true electromagnetic response is well approximated when $N_\lambda = 200$. The error with the simulation at lower N_λ changes negligibly, i.e., convergence is reached.

The accuracy of one particular set of choices is studied. First, the VCCSs voltages are sampled by averaging over the interface. Second, the evaluation points m and m are used. Finally, the BE method is used to approximate the derivative operator. These were chosen as the region of practical stability is the most flexible compared to the other choices. Both situations are computed with $\alpha_{\text{Courant}} = 0.99$ and $N_\lambda = 64$. Here, simulating situation b is practically stable while the error with the reference is the smallest possible. Furthermore, the discretized length $k\Delta z$ is only 0.7% larger than d as a result of the high N_λ. The SRMSEs of situation a with both the reference and situation b are shown as function of modulation frequency in Figure 4.5. We start by discussing frequencies lower than approximately 5 GHz. The error is at most 4.7%. This is a reasonably good result, as can be seen when plotting the signals of both situations in Figure 4.6(b) at $f_c = 3.5\,\text{GHz}$. The accuracy becomes much better when approaching DC. Here, the small errors that remain from an already highly resolved FDTD simulation are similar to the errors introduced by the SS scheme. The SRMSE decreases near DC similarly as the errors introduced by VF decrease near DC. This suggests that, for low frequencies, the residual error is mostly due to the imperfect vector fitting. At $f_c = 10\,\text{MHz}$, the result is very good, as can be appreciated in Figure 4.6(a). When the modulation frequency is above 5 GHz, the accuracy rapidly deteriorates. The accuracy at $f_c = 6.5\,\text{GHz}$ is unacceptably low, as seen in Figure 4.6(c). The break down of accuracy beyond 5 GHz is unexpected. Below 7 GHz, the FRE in the VF procedure is similar to the FRE for frequencies below 5 GHz. Negligible energy is present at

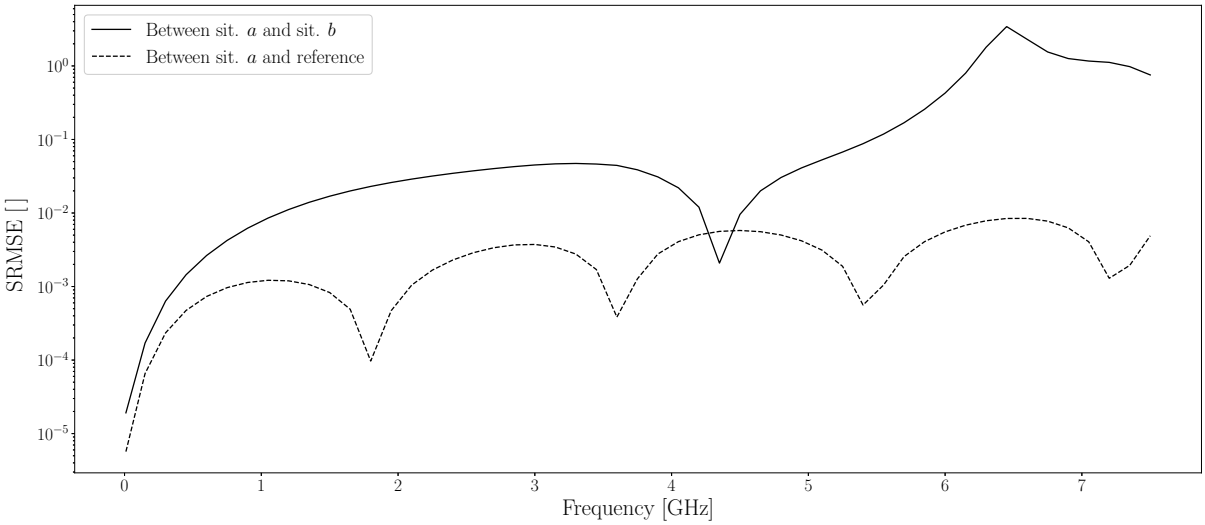

Figure 4.5: SRMSEs of different time domain signals computed with a source (detailed in (4.19)) of varying modulation frequency f_c. Situation (sit.) a and b have free parameters $\alpha_{\text{Courant}} = 0.99$ and $N_\lambda = 64$. The reference simulation of situation a has parameters $\alpha_{\text{Courant}} = 0.99$ and $N_\lambda = 200$. The dashed line essentially represent residual error present as a result of FDTD. The full line represents the error induced by our implementation. The VCCSs voltages are sampled by averaging over the interface. The evaluation points m and m are used with the BE method. The lossless DSA operator is used.

frequencies beyond 7 GHz because the BW of the modulated Gaussian pulse is too small.
Now that the accuracy has been studied in the time domain, we conclude the analysis with a derived result in the frequency domain. The source (4.19) is used with $\sigma = 1 \times 10^{-10}\,\text{s}^{-1}$. As a consequence, 99.7% of the spectral content is contained within the bandwidth $[f_c \pm 4.8\,\text{GHz}]$. Choosing $f_c = 3\,\text{GHz}$, the source covers the full BW of interest [0,7.5 GHz]. A well-defined transfer function can now be computed in the BW, as is usual in FDTD post-processing [27]. Here we divide spectral content of the recorder voltage over the spectral content of the generator source $\hat{e}_g(\omega)$. The results for both situations are shown in Figure 4.7. The simulations, including the reference simulation of situation a, were performed with the same parameters and choices as for the time domain analysis. The NRMSE from DC to 5.5 GHz is 1.64%. The NRMSE from DC to 0.5 GHz is 0.52%. The accuracy is unacceptably low after approximately 5.5 GHz. While a time domain accuracy analysis is more interpretable, their results are qualitatively identical to those of the frequency domain. Therefore, we will perform frequency domain analyses in the following sections. The reader is referred to Figure 4.6 to obtain a clear depiction of the error at a certain frequency.

4.3 Lossy Leapfrog

Introducing small losses will ease the passivity of a combined scheme with macromodels [11]. Hence, the accuracy in the VF procedure is improved and larger regions of stability are expected.

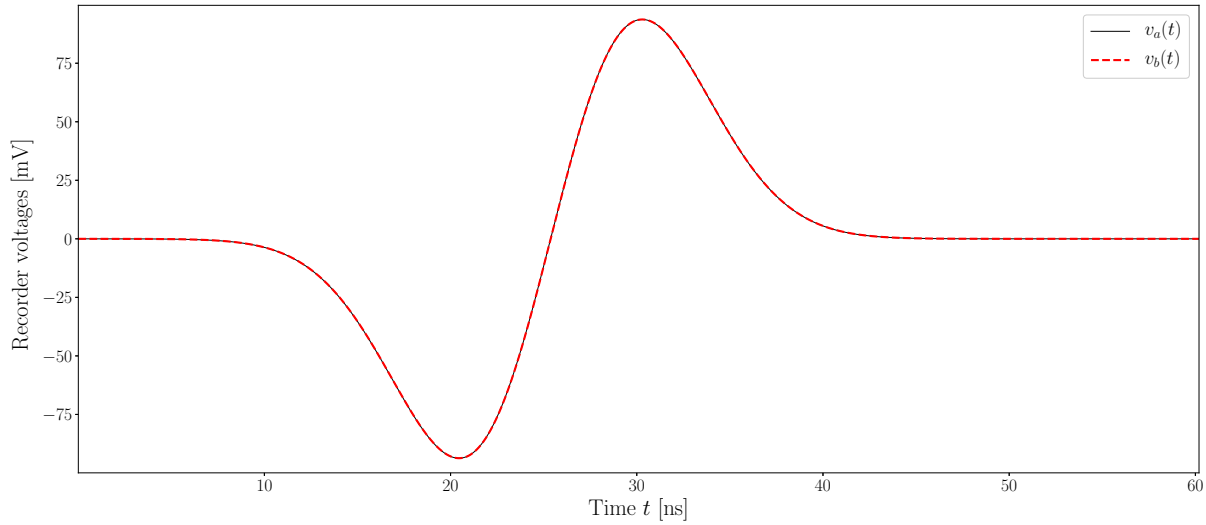

(a) At $f_c = 10\,\text{MHz}$.

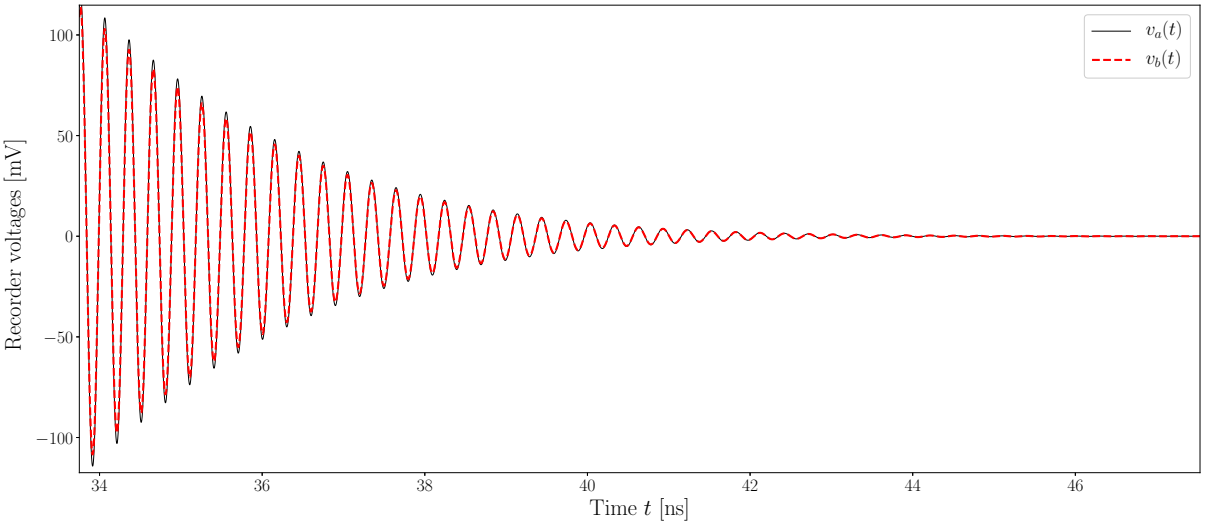

(b) At $f_c = 3.5\,\text{GHz}$. Only the wake of the pulse is shown for clarity.

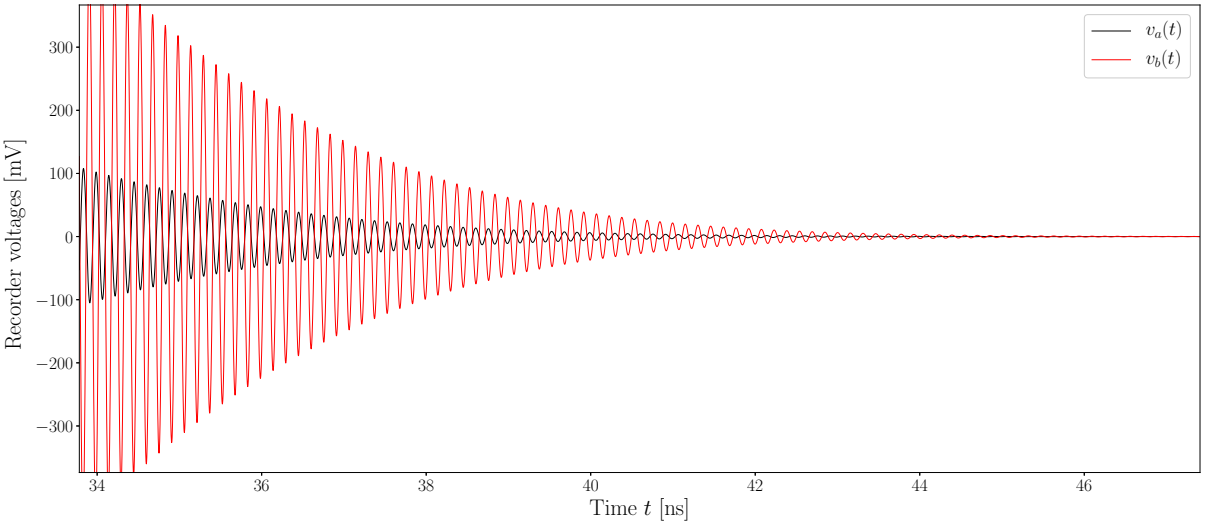

(c) At $f_c = 6.5\,\text{GHz}$. Only the wake of the pulse is shown for clarity.

Figure 4.6: Responses (4.11) in situation a and b of Gaussian pulses modulated at different frequencies f_c as detailed in (4.19). The corresponding SRMSEs are seen in Figure 4.5.

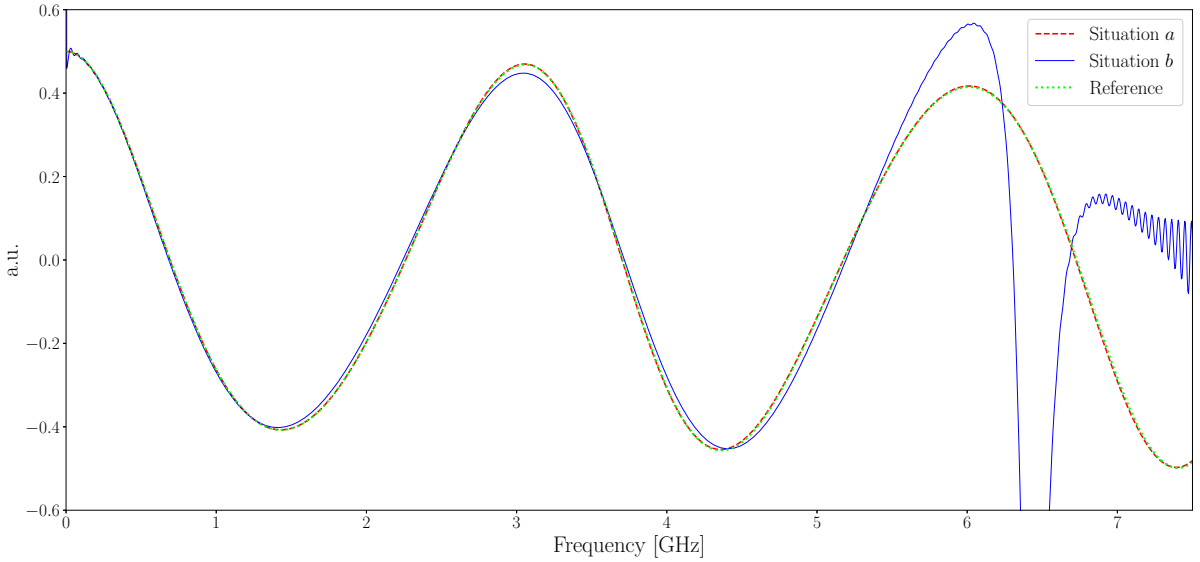

Figure 4.7: Transfer functions from simulations of both situations. The spectral content of the recorder voltage is divided by the spectral content of the source (detailed in (4.19)), which is nonzero in the BW shown. Situation a and b have free parameters $\alpha_{\text{Courant}} = 0.99$ and $N_\lambda = 64$. The reference simulation of situation a has parameters $\alpha_{\text{Courant}} = 0.99$ and $N_\lambda = 200$. The VCCSs voltages are sampled by averaging over the interface. The evaluation points m and m are used with the BE method. The lossless DSA operator is used.

The attenuation factor a in a coaxial line [23] is

$$a = \frac{R_s}{2Z_{\omega'} \ln \frac{b}{a}} \left(\frac{1}{a} + \frac{1}{b} \right) + \frac{\sigma Z_{\omega'}}{2}, \tag{4.20}$$

where $R_s = 1/(\sigma\delta)$ and $Z_{\omega'}$ is the characteristic impedance at angular frequency ω'. The first term dominates over the second term. If, e.g., $\omega' = 2\pi \cdot 4.571\,\text{GHz}$, and assuming no reflections occur, the signal is attenuated by a factor of $\exp(-2\,\text{cm}/3.85\,\text{cm}) \approx 0.60$ after a distance of 2 cm. Losses are noticeable because this is the length of the central transmission line.

The lossy DSA operator is not passive. As expected, it is then not possible to apply VF while enforcing passivity. The error introduced by VF is reduced for the lossy SA operator of situation a, as shown in Figure 4.8(a). This is because the resonance peak does not go to infinity, decreasing the dynamic range. The FRE is less than 0.3%. The condition number of $\mathbf{A}$ is 11.13, much lower than was the case for the lossless DSA. However, the fitting of the lossless SA operator of situation b suffers from the same problems as the lossless DSA operator. This is seen in Figure 4.8(b).

Also as expected, using the previous schemes from the lossless case with two fitted SA operators yields much larger regions of unstable simulations. However, the evaluation points m and m do not require the knowledge of $\boldsymbol{V}_s^{m+1/2}$. Two additional schemes were derived in Section 3.3.3 based on an approximation in time of the VCCSs currents (henceforth called *approximated schemes*). The sampling choice multiplies the available choices to eight. When the TR method

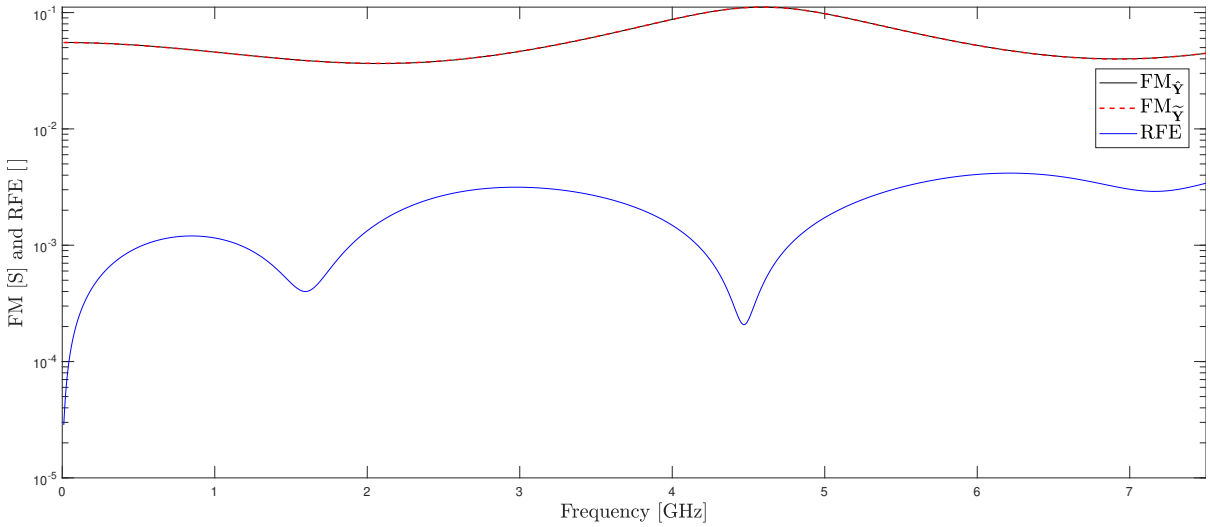

(a) For situation a.

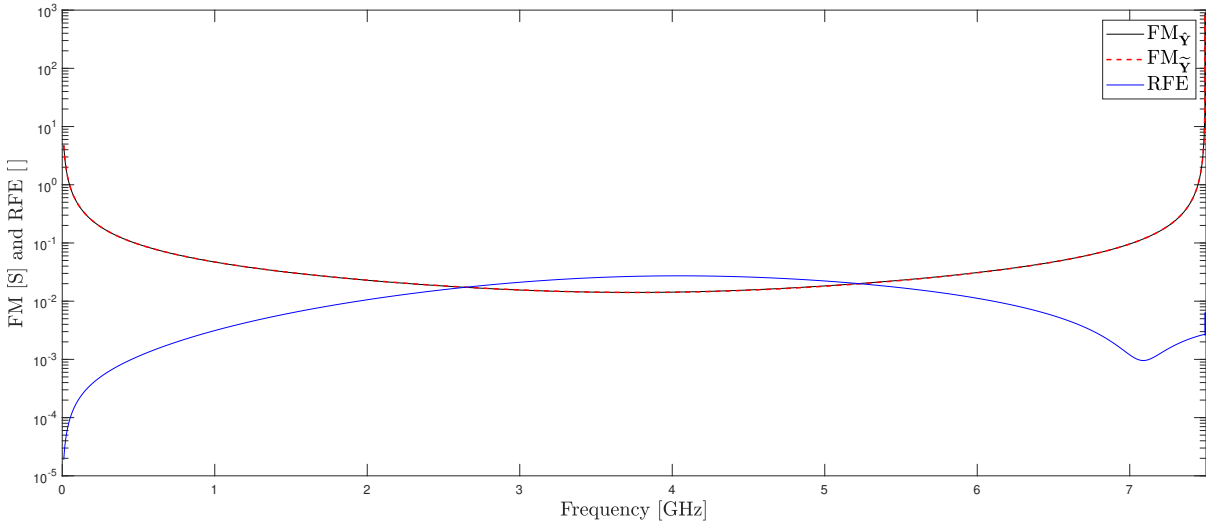

(b) For situation b.

Figure 4.8: These plots each show an analytical SA operator, its vector fitted counterparts and the error between them. The non-dispersive approximation is used to parametrize the lossy SA operator of situation a. Only the fitted range is shown, after which the accuracy becomes poor. The definition of the FM and FRE metrics are explained in Section 4.1.4.

is used with the approximated schemes, almost identical regions are observed as in the lossless case. When the TR method is used with no approximated schemes, fully unstable results are observed. For the sake of brevity, we will not plot these. When the BE method is used, we obtain Figure 4.9. Averaging VCCSs voltages over the interface yields limited to unstable simulations. When the VCCSs voltages are sampled on the integer positions, regions of practical stability are found. With no approximated scheme, this region is small and granulated. With the approximated scheme, a very large region of practical or limited stability is seen. This observation was the reason for us to introduce this new scheme. Specific N_λ values also cause changes in stability, but to a small extent. The Courant limit appears to be more strict and slightly dependent on N_λ.

We now proceed with the accuracy of the non-dispersive lossy model. The most flexibility is offered when the VCCSs voltages are sampled on $z = P\Delta z$ and $z = Q\Delta z$. The other schemes are not studied here. Figure 4.10 is obtained with the same method as in the lossless case. The analysis for the approximated scheme and the non-approximated scheme need to employ identical choices and free parameters to facilitate a good comparison. α_{Courant} and N_λ are chosen such that we have a practically stable simulation, e.g., $\alpha_{\text{Courant}} = 0.8$ and $N_\lambda = 22.5$. The error introduced by FDTD is negligible, as is clear when comparing with the reference at $\alpha_{\text{Courant}} = 0.99$ and $N_\lambda = 200$. The accuracy without the approximated scheme is good. The NRMSE from DC to 5.5 GHz is 2.57%, a higher figure than in the lossless case. This is despite a FRE of the SA operator of situation b which is significantly improved at these frequencies compared to the lossless case. The NRMSE from DC to 0.5 GHz is 0.35%. Therefore, the improved FRE at low frequencies does translate into a more accurate simulation at low frequencies. As could be expected by the use of an approximation, the accuracy is significantly lower when the approximated scheme is used. The NRMSE from DC to 5.5 GHz is 12.14%. In conclusion, the approximated schemes have an improved stability at the cost of a lower accuracy in this particular experiment.

Finding stable regions without the approximation is not always guaranteed. This is the case in the next implementation we present, which is of interest to prove our method's ability to abstract the skin effect. Here, the conductivity of the core from $5.9 \times 10^7\,\mathrm{S\,m^{-1}}$ to $5.9 \times 10^5\,\mathrm{S\,m^{-1}}$. A smaller conductivity increases the losses R_s and thus decreases the length over which the signal attenuates in the central transmission line. Consider the same exercise we did at the start of this section. The signal is now attenuated by a factor of $\exp(-2\,\mathrm{cm}/0.386\,\mathrm{cm}) \approx 5.64 \times 10^{-3}$ after a distance of 2 cm. Therefore, this forms a good analogue of the skin effect that appears in full-wave simulations, but in the longitudinal direction. The longitudinal skin depth is reduced by a factor of 10 because the dominant losses R_s scale as $1/\sqrt{\sigma}$. This is chosen to study the ability of VF and our schemes to model realistically small skin depths compared to simulation components. There may also be a practical use in this academic exercise. In fact, the order of magnitude of this lower conductivity corresponds to, e.g., Carbon Nanotubes (CNTs) composites used in state-of-the-art TSVs [54, 55]. The new SA operator of situation a is vector fitted, while situation b remains lossless. The operator is also not very dynamic, such that the results are similar to the previous SA operator of situation a. The VF error and condition number are

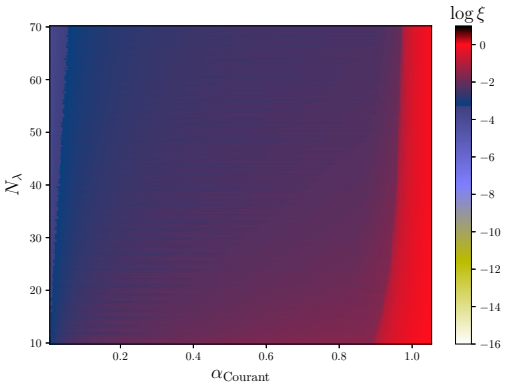

(a) The VCCSs voltages are sampled by averaging over the interface. The evaluation points m and m are used with the BE method are used

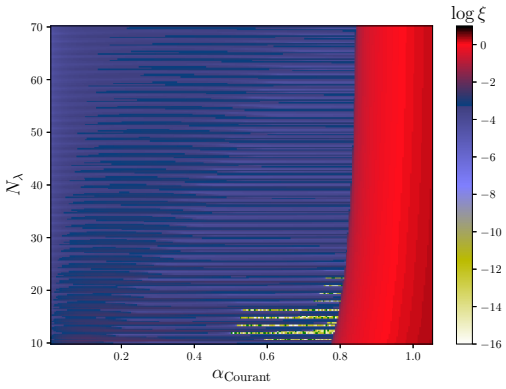

(b) The VCCSs voltages are sampled on $z = P\Delta z$ and $z = Q\Delta z$. The evaluation points m and m are used with the BE method are used.

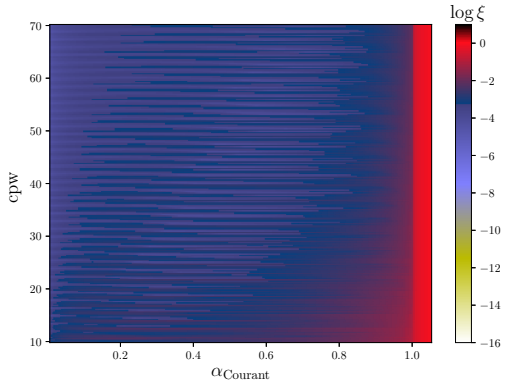

(c) The VCCSs voltages are sampled by averaging over the interface. The scheme of Section 3.3.3 with the BE method is used.

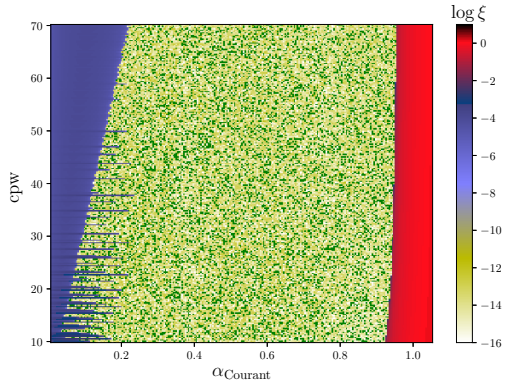

(d) The VCCSs voltages are sampled on $z = P\Delta z$ and $z = Q\Delta z$. The scheme of Section 3.3.3 with the BE method is used.

Figure 4.9: An incomplete stability analysis of the lossy full system. The lossy non-dispersive SA operator of situation a is used. A change in column is a change in how the VCCSs votages are sampled. A change in row is a change in whether or not the approximation of Section 3.3.3 is used. Clarification of these plots is given in Section 4.1.2.

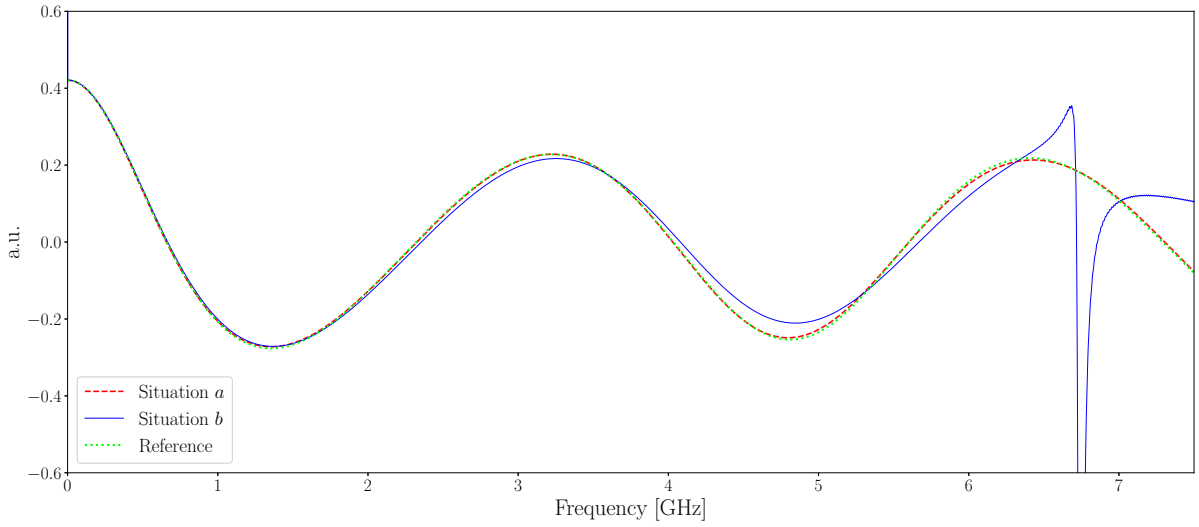

(a) Without the approximated scheme from Section 3.3.3.

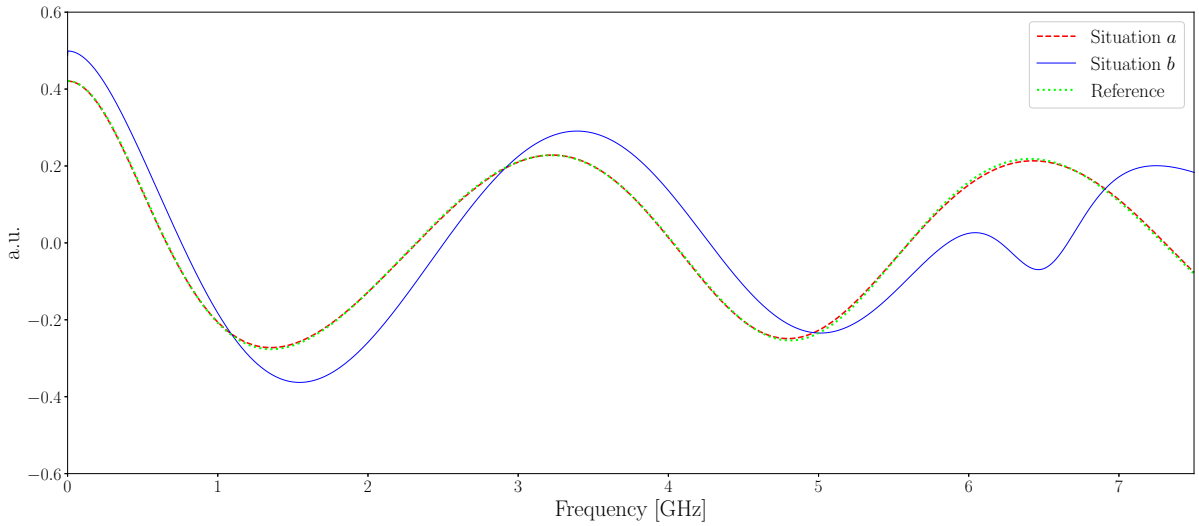

(b) With the approximated scheme from Section 3.3.3.

Figure 4.10: Transfer functions from simulations of both situations with and without the approximated scheme from Section 3.3.3. The spectral content of the recorder voltage is divided by the spectral content of the source (detailed in (4.19)), which is nonzero in the BW shown. Situation a and b have free parameters $\alpha_{\text{Courant}} = 0.8$ and $N_\lambda = 22.5$. The reference simulation of situation a has parameters $\alpha_{\text{Courant}} = 0.99$ and $N_\lambda = 200$. The VCCSs voltages are sampled on $z = P\Delta z$ and $z = Q\Delta z$. The evaluation points m and m are used with the BE method. The lossy non-dispersive SA operator of situation a is used.

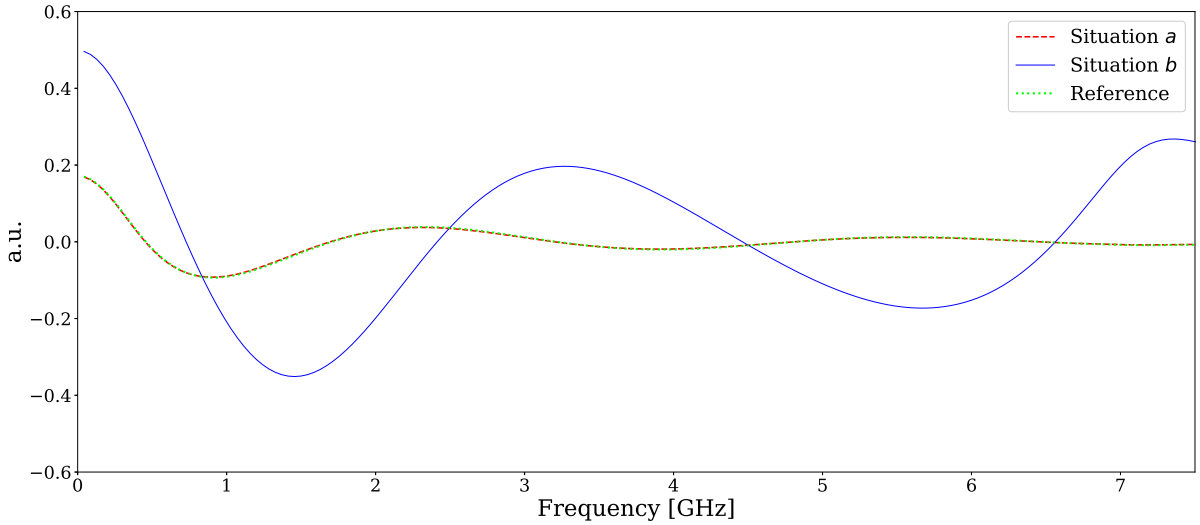

.

Figure 4.11: Transfer functions from simulations of both situations. The spectral content of the recorder voltage is divided by the spectral content of the source (detailed in (4.19)), which is nonzero in the BW shown. Situation a and b have free parameters $\alpha_{\text{Courant}} = 0.8$ and $N_\lambda = 22.5$. The reference simulation of situation a has parameters $\alpha_{\text{Courant}} = 0.99$ and $N_\lambda = 200$. The VCCSs voltages are sampled on $z = P\Delta z$ and $z = Q\Delta z$. The evaluation points m and m are used with the BE method. The lossy non-dispersive SA operator of situation a is used but with a lower conductivity of $5.9 \times 10^5\,\mathrm{S\,m^{-1}}$

slightly better. When the approximated schemes are used, the plots in the stability analyses are also highly similar to Figure 4.9(c) and (d). For the sake of brevity, we will not plot the error of VF or the plot the stability as a function of the free parameters. Instead, we immediately provide the accuracy of this approach. The same parameters are used as above. This is shown in Figure 4.11. The approximated scheme causes the accuracy to be unacceptably low. Therefore, obtaining a stable and accurate simulation is not possible for this example.

Clearly, the approximated schemes are not a good solutions due to the lower accuracy. The lossy implementation did not better the stability problems, which we expected to vanish upon introducing losses. However, the SA operator corresponding to situation b still models a lossless situations. A reasonable hypothesis is that eigenvalues on the unit circle of this system could cause the full system to become unstable. Therefore, we can expect an implementation where both situations are lossy to be much more stable. However, abstraction of one material to another is necessary for the existence of (differential) SA operators. The lossy central transmission line must have different material parameters in the two situations. Consider situation a where the conductivity of the core is reduced to $5.9 \times 10^5\,\mathrm{S\,m^{-1}}$. The central transmission line of Situation b has the same core conductivity as before, $5.9 \times 10^7\,\mathrm{S\,m^{-1}}$. Until this point, ξ was always approximately 0 for the SS subsystem. We now see that $\xi < 0$ for all schemes and for all possible choices. This is what we expect when both SA operators are lossy. Surprisingly, the full scheme is never stable, as shown in Figure 4.12. None of the choices fall in the category of

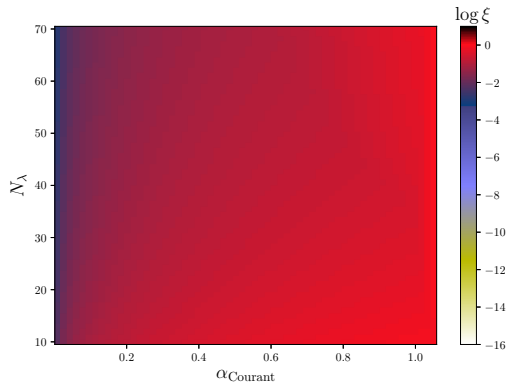

(a) The VCCSs voltages are sampled by averaging over the interface. The BE method is used.

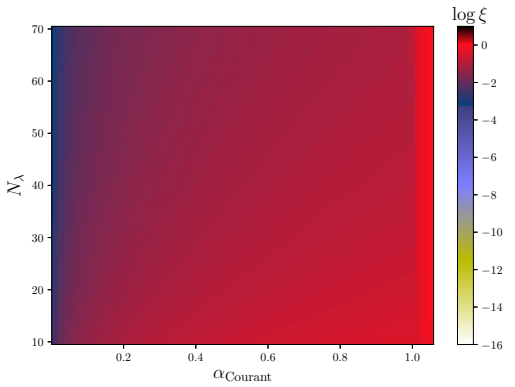

(b) The VCCSs voltages are sampled on $z = P\Delta z$ and $z = Q\Delta z$. The BE method is used.

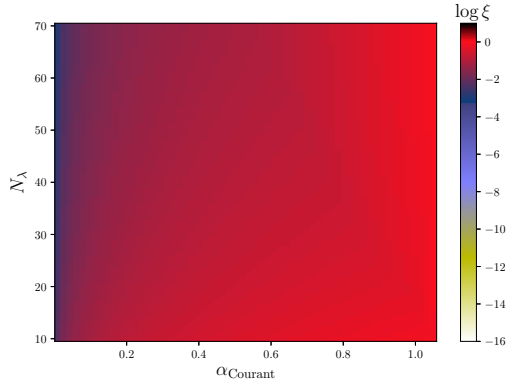

(c) The VCCSs voltages are sampled by averaging over the interface. The TR method is used.

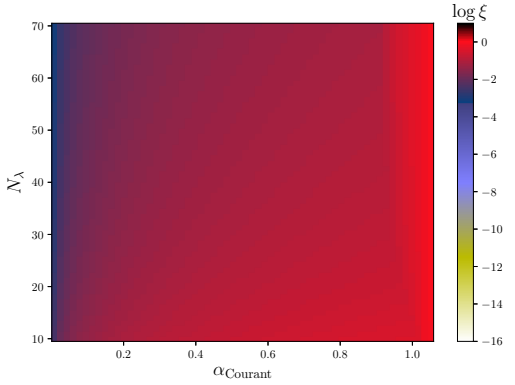

(d) The VCCSs voltages are sampled on $z = P\Delta z$ and $z = Q\Delta z$. The TR method is used.

Figure 4.12: A complete stability analysis of the full system when both situations are lossy. The standard lossy non-dispersive SA operator is used for situation a. The SA operator with a lower conductivity is used for situation b. The evaluation points m and m are always used. Clarification of these plots is given in Section 4.1.2.

either limited or practical stability for any of the free parameters. It appears that the coupling of the SS scheme with the FDTD scheme causes eigenvalues of the SS scheme to move outside the unit circle regardless of their position when analyzing the SS subsystem. We cannot give an explanation for this observation. In conclusion, we have set out in this paragraph to improve the conditional stability, but instead observed a stability that is unconditionally unstable.

Finally, we provide results of a dispersive model. Situation a is chosen as lossy and dispersive. Situation b is chosen lossless as in 4.2. Performing VF was difficult as the fit was more difficult, in particular near DC. The condition number is 1.46×10^9 and the error is higher than any other fit. This is shown in Figure 4.13. The stability analysis of the full scheme is shown in Figure 4.14 for the four available choices. As expected when no approximated schemes are used, we find large regions of unstable simulations. A Courant-like stability criterion appears

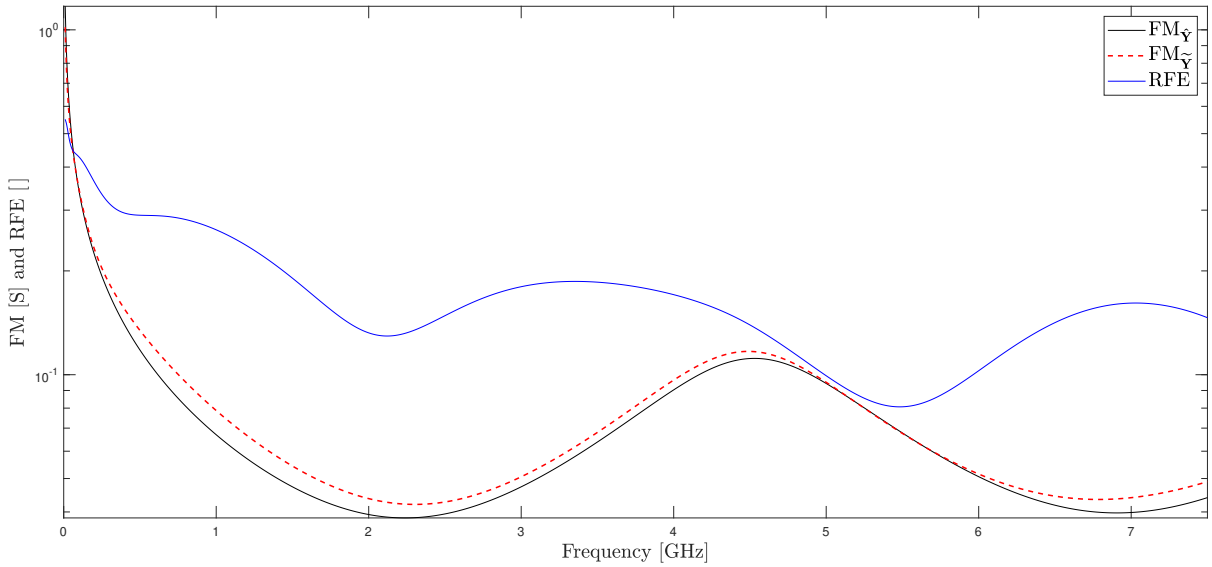

Figure 4.13: This plot shows the analytical lossy dispersive SA operator, its vector fitted counterpart and the error between them. Only the fitted range is shown, after which the accuracy becomes poor. The definition of the FM and FRE metrics are explained in Section 4.1.4.

at $\alpha_{\text{Courant}} \approx 0.2$. For small time steps, all choices have a narrow region of limited stability. Low values of α_{Courant}, ideally smaller than approximately 0.01 are required for limited stability. The number of time steps is significantly higher for these values of α_{Courant}. Therefore the ξ_{max} value in (4.6) is is more stringent. As a result, no signal can be obtained without becoming noticeably unstable before tapering to zero.

4.4 Lossless FCI-FDTD

Throughout this chapter we noticed that the stability of the various schemes is compromised. More specifically, there is a low flexibility in the available free choices and parameters as regions of stability are small. One stability bound has remained constant throughout all the observations: the Courant limit must be upheld. The implicit FCI-FDTD method was designed to circumvent this limit while remaining accurate. This is why we introduced the SS-FCI-FDTD method, to hopefully harness this larger flexibility in the free parameter α_{Courant}. We limited ourselves to only one choice in Section 3.4.2. It uses the DSA operator when both situation a and b are lossless, as in Section 4.2. A stability analysis of this one scheme is shown in Figure 4.15. The region of practical stability is the largest among all results studied in this chapter. Limited stability is sometimes observed for $\alpha_{\text{Courant}} < 1$. For large time steps, a sharply defined unstable region is seen.

We now examine the accuracy of the SS-FCI-FDTD scheme. The large amount of flexibility facilitates an easy analysis as a function of α_{Courant}. We vary α_{Courant} from 1 to 5 for all simulations. Transfer functions for each of these are shown in Figure 4.16. Situation a is computed

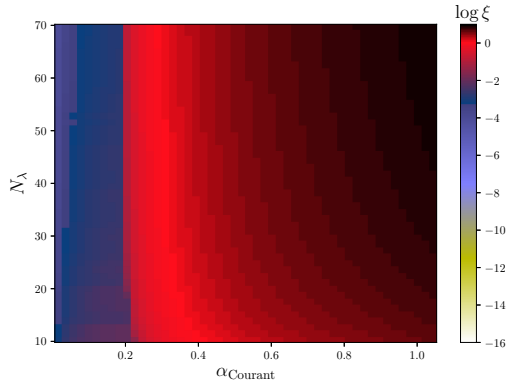

(a) The VCCSs voltages are sampled by averaging over the interface. The BE method is used.

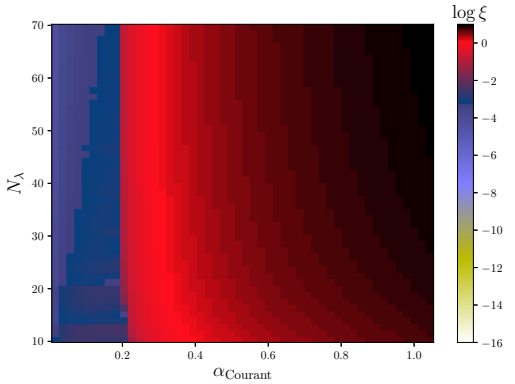

(b) The VCCSs voltages are sampled on $z = P\Delta z$ and $z = Q\Delta z$. The BE method is used.

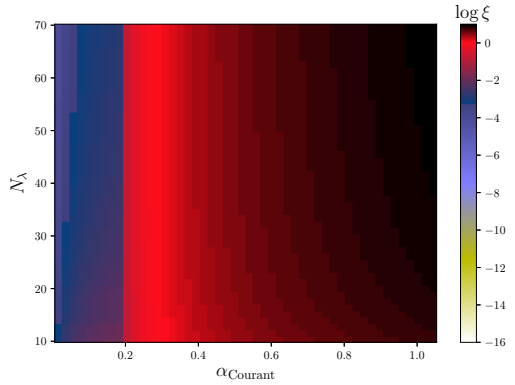

(c) The VCCSs voltages are sampled by averaging over the interface. The TR method is used.

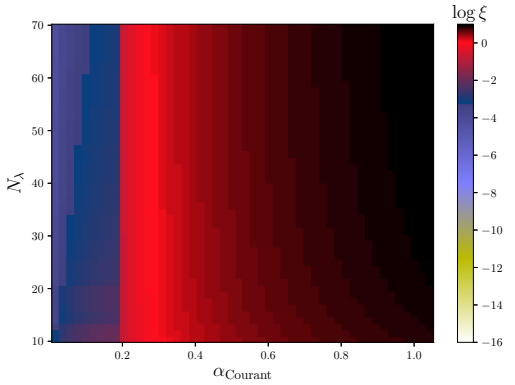

(d) The VCCSs voltages are sampled on $z = P\Delta z$ and $z = Q\Delta z$. The TR method is used.

Figure 4.14: A complete stability analysis of the full dispersive lossy system. The lossy dispersive SA operator is used for situation a. The lossless SA operator is used for situation b. The evaluation points m and m are always used. Clarification of these plots is given in Section 4.1.2.

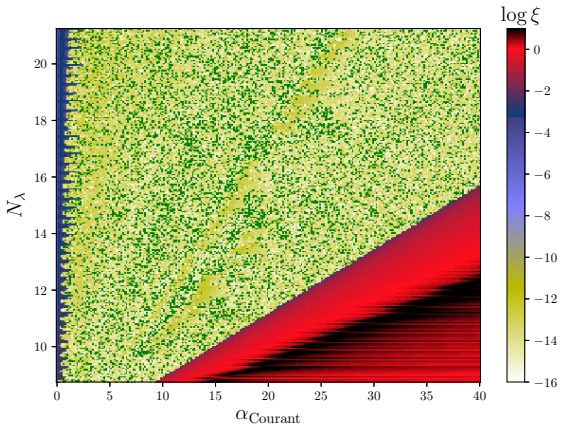

Figure 4.15: A stability analysis for the lossless SS-FCI-FDTD full system.

with $N_\lambda = 64$. The reference of this situation is simulated with $N_\lambda = 200$. Both are computed with standard FCI-FDTD. The latter has converged sufficiently such that the error with situation a is negligible. Situation b is also simulated with $N_\lambda = 64$.

For brevity the variation in α_{Courant} is reduced to only 2 simulations, for a value of 1 and 5. The accuracy progressively worsens. This is a feature from FCI-FDTD, where larger time steps will always come at the cost of accuracy. However, in SS-FCI-FDTD, this influence is amplified, as can be concluded when observing the error of the reference to situation a. For $\alpha_{\text{Courant}} = 1$, the NRMSE from DC to 5.5 GHz is 1.35%. The NRMSE from DC to 0.5 GHz is 0.15%. These represent the highest degree of accuracy among all results studied in this chapter. As has always been the case, the accuracy is poor after approximately 5.5 GHz. While good results are still found for $\alpha_{\text{Courant}} = 5$, increasing this to, e.g., $\alpha_{\text{Courant}} = 10$ quickly leads to unacceptably low accuracies. A more in-depth analysis of accuracy as function α_{Courant} and N_λ could be done when disregarding the unstable region. This is a good place to start with future work, along with exploring new choices in the SS-FCI-FDTD method.

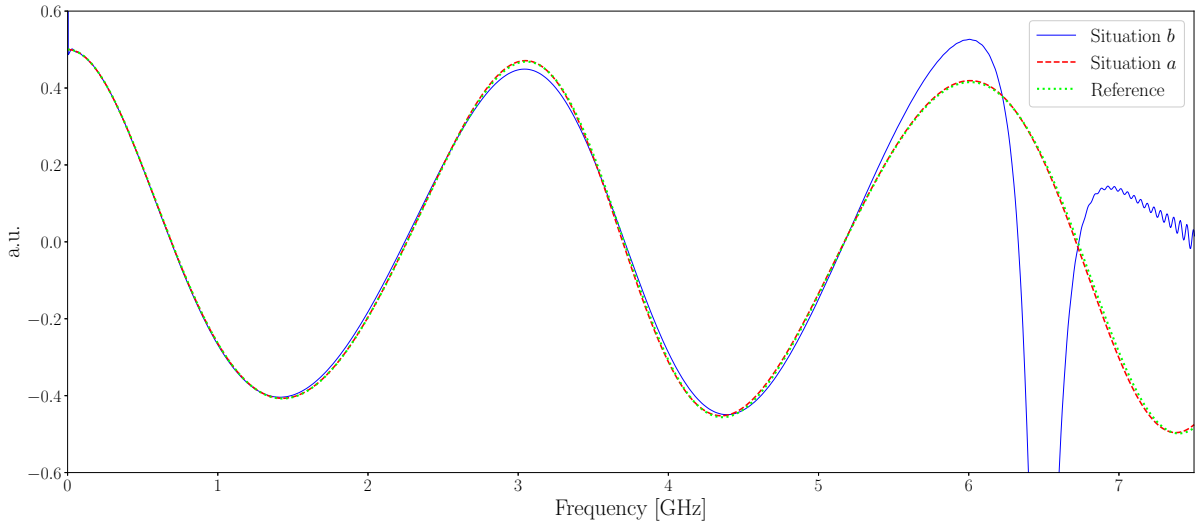

(a) With $\alpha_{\text{Courant}} = 1$.

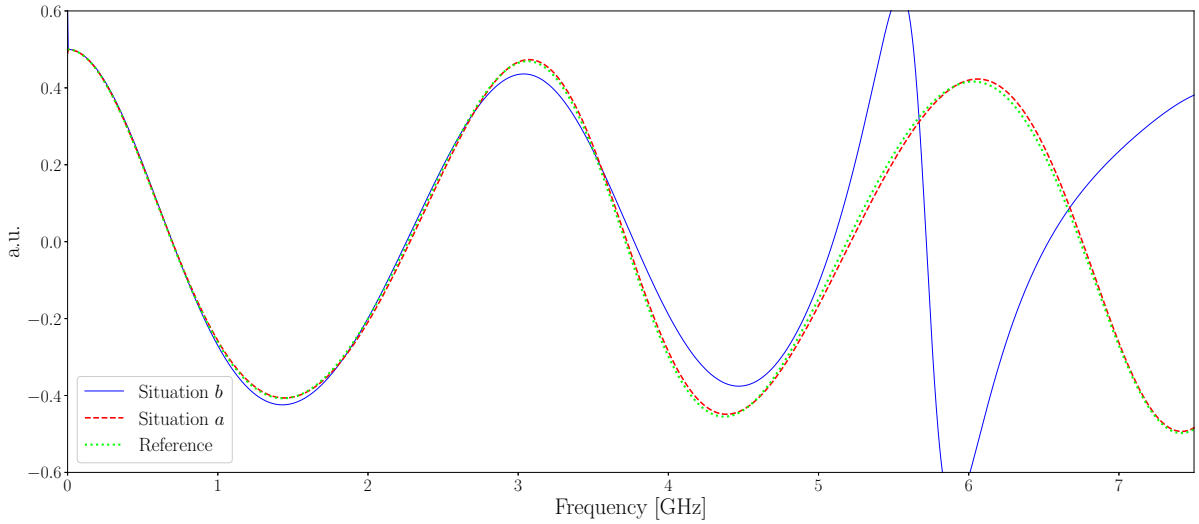

(b) With $\alpha_{\text{Courant}} = 5$.

Figure 4.16: Transfer functions from simulations of both situations when the SS-FCI-FDTD method is employed (detailed in Section 3.4.2 with its unique set of choices). The spectral content of the recorder voltage is divided by the spectral content of the source (detailed in (4.19)), which is nonzero in the BW shown. Situation a and b have $N_\lambda = 64$. The reference simulation of situation a has $N_\lambda = 200$. The free parameter α_{Courant} is varied for all simulations. The lossless DSA operator is used.

Chapter 5

Conclusions and Future Work

5.1 Conclusions

In this thesis, VF was used to convert fitted (differential) SA operators to a SS model. Subsequently, the model was discretized and interfaced with FDTD or FCI-FDTD. Hence, an alternative simulation is obtained that replaces the material in a region of space while preserving its response. This replacement circumvents the simulation of well-developed skin effects. Therefore, broadband modeling of good conductors becomes possible, in theory without any drawbacks. This is important for, e.g., SI and EMC applications as it can be applied in the time domain. Voltage controlled surface currents are easily added to commercial ECAD codes. Thus, designers can much more efficiently optimize and validate state-of-the-art ICs. The idea was explored with three distinct implementations on a series connection of transmission lines with VCCSs.

In the first implementation, the transmission lines were assumed lossless and computed with leapfrog FDTD. Combined numerical schemes were derived to fit into leapfrog FDTD, whose favorable explicit nature was preserved. Also, a number of choices were left free, resulting in a large set of available schemes. A subset of these were treated in Chapter 4. The lossless case causes eigenvalues of the SS scheme to either be on the unit circle when the BE method is used or potentially outside when the TR method is used. This was explained by machine precision errors, who also affect the stability of the full scheme. As a result, the bounds on regions of stability were of a complex nature. The patterns varied by α_{Courant}, N_λ, the free choices and the operator used. We then examined the error of our schemes for a specific stable simulation. In general, good to very good accuracies were found in the frequency and time domain. However, the accuracy deteriorates at frequencies approximately 25% lower than the maximum fitted frequency of VF, which we did not expect.

In the second implementation, lossy transmission lines, inspired from a realistic coaxial TSV, were computed with leapfrog FDTD. Introducing small losses was expected to attenuate instabilities and ease the VF procedure. However, the DSA operator had to be interchanged with two SA operators for each situation, as passivity could not be enforced. As a consequence, the

number of available choices is reduced. Unfortunately, the stability was not improved. When simulations were stable, similar accuracies were observed. However, stable configurations were rare and sometimes impossible to find. We resorted to an approximated scheme that alleviated instability at the cost of a substantial decrease in accuracy. Remarkably, it appears that the stability problems are caused by the coupling with FDTD, regardless of the eigenvalues of the SA operators.

In the third implementation, again lossless transmission lines were used. The SS model was incorporated into the implicit FCI-FDTD method, which is known to provide greater flexibility in α_{Courant}. While more choices are possible, only one numerical scheme is provided in this thesis. This combined SS-FCI-FDTD scheme was easily derived due to the implicit time stepping. The best results among all tested methods in Chapter 4 were found with this method in terms of stability and accuracy.

5.2 Future Work

First, the most natural continuation of this work is probably the derivation of more advanced SS-FCI-FDTD numerical schemes. For example, one could add passive SA operators to study the lossy systems, possibly for different free choices. We expect such a scheme to be both stable, accurate and useful for practical applications. As discussed in Chapter 4, replacing a well-developed skin effect or dispersive material is of practical importance. The latter could open the way to simulate in the time domain any physical system that is defined in the frequency domain. If successful, the method also bears its fruits in, e.g., the multiphysics literature.

Second, while the above path is of interest to the engineer, taking a step back could increase our understanding of the most complex and unexpected results that have been discussed. Thereto, theorems need to be rigorously proven a priori instead of conjectured a posteriori. Most importantly, this could simplify analyzing relevant results if, e.g., taking a certain free choice is always superior.

Finally, the idea can be applied to more than one dimension. In this case, new but similar derivations are required that incorporate the SS schemes into Maxwell's laws of electromagnetism.

Appendix A

Passivity of SA Operators

The FET is applied to a one-port connected to a lossy transmission line. The load acts as region II and is characterized by a passive complex impedance Z_1. In situation b, this is changed to the characteristic impedance of the transmission line with complex impedance Z_0, as shown in Figure A.1. Node $\mathcal{L}$ is akin to node $\mathcal{P}$ in Figure 3.1.

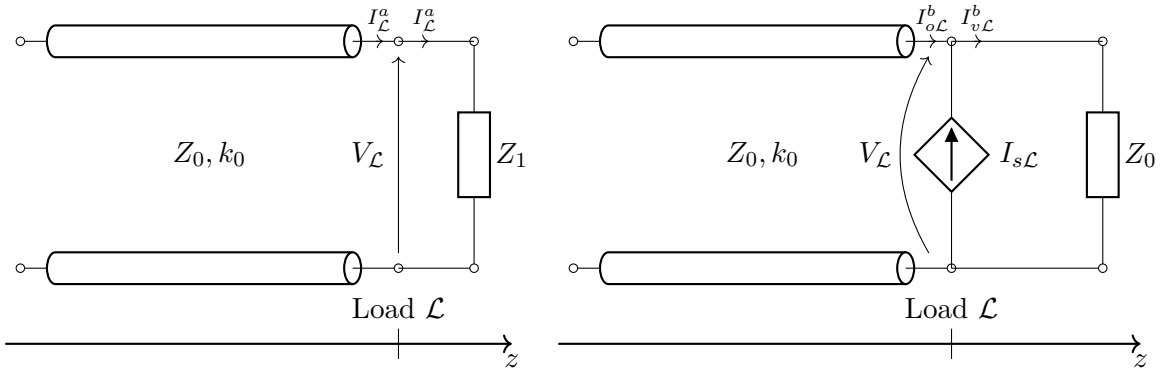

(a) Situation a.

(b) Situation b.

Figure A.1: Situations of the FET applied to a one-port network connected to a lossy transmission line. The FET substitutes the complex impedance Z_1 of the one-port to the characteristic impedance Z_0 of the transmission line. It illustrates a non-passive DSA operator.

We immediately find that

$$\begin{aligned} I^a_{\mathcal{L}} &= Y^a V_{\mathcal{L}} = \frac{1}{Z_1} V_{\mathcal{L}} \quad , \quad \mathrm{Re}\{Y^a\} > 0\,; \\ I^b_{v\mathcal{L}} &= Y^b V_{\mathcal{L}} = \frac{1}{Z_0} V_{\mathcal{L}} \quad , \quad \mathrm{Re}\{Y^b\} > 0\,. \end{aligned} \tag{A.1}$$

In these equations, the conditions on Y^a and Y^b originate from the physics of a passive complex impedance. The DSA operator can now be constructed as before from KCL:

$$I_{s\mathcal{L}} = I^b_{v\mathcal{L}} - I^b_{o\mathcal{L}} = I^b_{v\mathcal{L}} - I^a_{\mathcal{L}} = \underbrace{\left(Y^b - Y^a\right)}_{Y} V_{\mathcal{L}}\,. \tag{A.2}$$

We now conclude that

$$\begin{aligned} \mathrm{Re}\{Y\} &= \mathrm{Re}\{\frac{1}{Z_0} - \frac{1}{Z_1}\} \\ &= \frac{\mathrm{Re}\{Z_0\}}{|Z_0|^2} - \frac{\mathrm{Re}\{Z_1\}}{|Z_1|^2} \,. \end{aligned} \tag{A.3}$$

Clearly, this last expression is not always positive.

Appendix B

SS Discretization Schemes

The evaluations points in the following section titles refer to the first and second equation of (3.24). These are repeated for convenience:

$$\begin{aligned} \frac{\mathrm{d}}{\mathrm{d}t}\boldsymbol{X}(t) &= \mathbf{A}\boldsymbol{X}(t) + \mathbf{B}\boldsymbol{V}_s(t)\,, \\ \boldsymbol{I}_s(t) &= \mathbf{C}\boldsymbol{X}(t) + \mathbf{D}\boldsymbol{V}(t)\,. \end{aligned} \tag{B.1}$$

The discretization of the SS variables in time is implied from the indices used in each scheme. All final pairs of numeric equations in this appendix are updated in the order in which they are written.

B.1 Evaluation Points m and m

B.1.1 With the TR Method

The SS scheme is discretized as

$$\begin{aligned} \frac{\boldsymbol{X}^{m+\frac{1}{2}} - \boldsymbol{X}^{m-\frac{1}{2}}}{\Delta t} &= \mathbf{A}\frac{\boldsymbol{X}^{m+\frac{1}{2}} + \boldsymbol{X}^{m-\frac{1}{2}}}{2} + \mathbf{B}\boldsymbol{V}_s^m\,, \\ \frac{\boldsymbol{I}_s^{m+\frac{1}{2}} + \boldsymbol{I}_s^{m-\frac{1}{2}}}{2} &= \mathbf{C}\frac{\boldsymbol{X}^{m+\frac{1}{2}} + \boldsymbol{X}^{m-\frac{1}{2}}}{2} + \mathbf{D}\boldsymbol{V}_s^m\,. \end{aligned} \tag{B.2}$$

The explicit form is

$$\begin{aligned} \boldsymbol{X}^{m+\frac{1}{2}} &= \left(\frac{\mathbb{I}_{n_x}}{\Delta t} - \frac{\mathbf{A}}{2}\right)^{-1}\left(\frac{\mathbb{I}_{n_x}}{\Delta t} + \frac{\mathbf{A}}{2}\right)\boldsymbol{X}^{m-\frac{1}{2}} + \mathbf{B}\boldsymbol{V}_s^m\,, \\ \boldsymbol{I}_s^{m+\frac{1}{2}} &= \mathbf{C}\boldsymbol{X}^{m+\frac{1}{2}} + \mathbf{C}\boldsymbol{X}^{m-\frac{1}{2}} + 2\mathbf{D}\boldsymbol{V}_s^m - \boldsymbol{I}_s^{m-\frac{1}{2}}\,, \end{aligned} \tag{B.3}$$

B.1.2 With the BE Method

The SS scheme is discretized as

$$\begin{aligned} \frac{\boldsymbol{X}^m - \boldsymbol{X}^{m-1}}{\Delta t} &= \mathbf{A}\boldsymbol{X}^m + \mathbf{B}\boldsymbol{V}_s^m\,, \\ \frac{\boldsymbol{I}_s^{m+\frac{1}{2}} + \boldsymbol{I}_s^{m-\frac{1}{2}}}{2} &= \mathbf{C}\boldsymbol{X}^m + \mathbf{D}\boldsymbol{V}_s^m\,. \end{aligned} \tag{B.4}$$

The explicit form is

$$\begin{aligned} \boldsymbol{X}^{m} &= \left(\frac{\mathbb{I}_{n_x}}{\Delta t} - \mathbf{A}\right)^{-1} \frac{1}{\Delta t}\boldsymbol{X}^{m-1} + \mathbf{B}\boldsymbol{V}_s^{m}\,, \\ \boldsymbol{I}_s^{m+\frac{1}{2}} &= 2\mathbf{C}\boldsymbol{X}^{m} + 2\mathbf{D}\boldsymbol{V}_s^{m} - \boldsymbol{I}_s^{m-\frac{1}{2}}\,. \end{aligned} \tag{B.5}$$

B.2 Evaluation Points m and $m + 1/2$

B.2.1 With the TR Method

The SS scheme is discretized as

$$\begin{aligned} \frac{\boldsymbol{X}^{m+\frac{1}{2}} - \boldsymbol{X}^{m-\frac{1}{2}}}{\Delta t} &= \mathbf{A}\frac{\boldsymbol{X}^{m+\frac{1}{2}} + \boldsymbol{X}^{m-\frac{1}{2}}}{2} + \mathbf{B}\boldsymbol{V}_s^{m}\,, \\ \boldsymbol{I}_s^{m+\frac{1}{2}} &= \mathbf{C}\boldsymbol{X}^{m+\frac{1}{2}} + \mathbf{D}\frac{\boldsymbol{V}_s^{m+1} + \boldsymbol{V}_s^{m}}{2}\,. \end{aligned} \tag{B.6}$$

The explicit form is

$$\begin{aligned} \boldsymbol{X}^{m+\frac{1}{2}} &= \left(\frac{\mathbb{I}_{n_x}}{\Delta t} - \frac{\mathbf{A}}{2}\right)^{-1} \left(\frac{\mathbb{I}_{n_x}}{\Delta t} + \frac{\mathbf{A}}{2}\right) \boldsymbol{X}^{m-\frac{1}{2}} + \mathbf{B}\boldsymbol{V}_s^{m}\,, \\ \boldsymbol{I}_s^{m+\frac{1}{2}} &= \left(\mathbb{I}_2 - \frac{\mathcal{C}}{4}\mathbf{D}\boldsymbol{\alpha}_{C,s}\right)^{-1} \left[\mathbf{C}\boldsymbol{X}^{m+\frac{1}{2}} + \frac{1}{2}\mathbf{D}\boldsymbol{V}_s^{m+1,\mathrm{yee}} + \frac{1}{2}\mathbf{D}\boldsymbol{V}_s^{m}\right]\,. \end{aligned} \tag{B.7}$$

B.2.2 With the BE Method

Without using extrapolation methods, it is not possible to construct a viable scheme under these specifications.

B.3 Evaluation Points $m + 1/2$ and m

B.3.1 With the TR Method

The SS scheme is discretized as

$$\begin{aligned} \frac{\boldsymbol{X}^{m+1} - \boldsymbol{X}^{m}}{\Delta t} &= \mathbf{A}\frac{\boldsymbol{X}^{m+1} + \boldsymbol{X}^{m}}{2} + \mathbf{B}\frac{\boldsymbol{V}_s^{m+1} + \boldsymbol{V}_s^{m}}{2}\,, \\ \frac{\boldsymbol{I}_s^{m+\frac{1}{2}} + \boldsymbol{I}_s^{m-\frac{1}{2}}}{2} &= \mathbf{C}\boldsymbol{X}^{m} + \mathbf{D}\boldsymbol{V}_s^{m}\,. \end{aligned} \tag{B.8}$$

This can be simplified to

$$\begin{aligned} \left(\frac{\mathbb{I}_{n_x}}{\Delta t} - \frac{\mathbf{A}}{2}\right) \boldsymbol{X}^{m+1} - \frac{\mathcal{C}}{4}\mathbf{B}\boldsymbol{\alpha}_{C,s}\boldsymbol{I}_s^{m+\frac{1}{2}} &= \left(\frac{\mathbb{I}_{n_x}}{\Delta t} + \frac{\mathbf{A}}{2}\right) \boldsymbol{X}^{m} + \frac{1}{2}\mathbf{B}\boldsymbol{V}_s^{m} + \frac{1}{2}\mathbf{B}\boldsymbol{V}_s^{m+1,\mathrm{yee}}\,, \\ \boldsymbol{I}_s^{m+\frac{1}{2}} &= 2\mathbf{C}\boldsymbol{X}^{m} + 2\mathbf{D}\boldsymbol{V}_s^{m} - \boldsymbol{I}_s^{m-\frac{1}{2}}\,. \end{aligned} \tag{B.9}$$

Collecting the SS variables $\boldsymbol{X}_s^{m+1}$ and $\boldsymbol{I}_s^{m+1/2}$ in one vector, we can construct the following block matrix system

$$\begin{bmatrix} \frac{\mathbb{I}_{n_x}}{\Delta t} - \frac{\mathbf{A}}{2} & -\frac{\mathcal{C}}{4}\mathbf{B}\boldsymbol{\alpha}_{C,s} \\ & \mathbb{I}_2 \end{bmatrix} \begin{bmatrix} \boldsymbol{X}_s^{m+1} \\ \boldsymbol{I}_s^{m+\frac{1}{2}} \end{bmatrix} = \begin{bmatrix} \frac{\mathbb{I}_{n_x}}{\Delta t} + \frac{\mathbf{A}}{2} & \\ 2\mathbf{C} & -\mathbb{I}_2 \end{bmatrix} \begin{bmatrix} \boldsymbol{X}_s^{m} \\ \boldsymbol{I}_s^{m-\frac{1}{2}} \end{bmatrix} + \begin{bmatrix} \frac{1}{2}\mathbf{B}\boldsymbol{V}_s^{m} + \frac{1}{2}\mathbf{B}\boldsymbol{V}_s^{m+1,\text{yee}} \\ 2\mathbf{D}\boldsymbol{V}_s^{m} \end{bmatrix}. \tag{B.10}$$

If the left-hand side matrix can be inverted, the output SS variable $\boldsymbol{I}_s^{m+1/2}$ is obtained.

B.3.2 With the BE Method

The SS scheme is discretized as

$$\begin{aligned} \frac{\boldsymbol{X}^{m+\frac{1}{2}} - \boldsymbol{X}^{m-\frac{1}{2}}}{\Delta t} &= \mathbf{A}\boldsymbol{X}^{m+\frac{1}{2}} + \mathbf{B}\frac{\boldsymbol{V}_s^{m+1} + \boldsymbol{V}_s^{m}}{2}, \\ \frac{\boldsymbol{I}_s^{m+\frac{1}{2}} + \boldsymbol{I}_s^{m-\frac{1}{2}}}{2} &= \mathbf{C}\frac{\boldsymbol{X}^{m+\frac{1}{2}} + \boldsymbol{X}^{m-\frac{1}{2}}}{2} + \mathbf{D}\boldsymbol{V}_s^{m}. \end{aligned} \tag{B.11}$$

This can be simplified to

$$\begin{aligned} \left(\frac{\mathbb{I}_{n_x}}{\Delta t} - \mathbf{A}\right)\boldsymbol{X}^{m+\frac{1}{2}} - \frac{\mathcal{C}}{4}\mathbf{B}\boldsymbol{\alpha}_{C,s}\boldsymbol{I}_s^{m+\frac{1}{2}} &= \frac{1}{\Delta t}\boldsymbol{X}^{m-\frac{1}{2}} + \frac{1}{2}\mathbf{B}\boldsymbol{V}_s^{m} + \frac{1}{2}\mathbf{B}\boldsymbol{V}_s^{m+1,\text{yee}}, \\ \boldsymbol{I}_s^{m+\frac{1}{2}} - \mathbf{C}\boldsymbol{X}^{m+\frac{1}{2}} &= \mathbf{C}\boldsymbol{X}^{m-\frac{1}{2}} + 2\mathbf{D}\boldsymbol{V}_s^{m} - \boldsymbol{I}_s^{m-\frac{1}{2}}. \end{aligned} \tag{B.12}$$

Collecting the SS variables $\boldsymbol{X}_s^{m+\frac{1}{2}}$ and $\boldsymbol{I}_s^{m+1/2}$ in one vector, we can construct the following block matrix system

$$\begin{bmatrix} \frac{\mathbb{I}_{n_x}}{\Delta t} - \mathbf{A} & -\frac{\mathcal{C}}{4}\mathbf{B}\boldsymbol{\alpha}_{C,s} \\ -\mathbf{C} & \mathbb{I}_2 \end{bmatrix} \begin{bmatrix} \boldsymbol{X}_s^{m+\frac{1}{2}} \\ \boldsymbol{I}_s^{m+\frac{1}{2}} \end{bmatrix} = \begin{bmatrix} \frac{\mathbb{I}_{n_x}}{\Delta t} & \\ \mathbf{C} & -\mathbb{I}_2 \end{bmatrix} \begin{bmatrix} \boldsymbol{X}_s^{m-\frac{1}{2}} \\ \boldsymbol{I}_s^{m-\frac{1}{2}} \end{bmatrix} + \begin{bmatrix} \frac{1}{2}\mathbf{B}\boldsymbol{V}_s^{m} + \frac{1}{2}\mathbf{B}\boldsymbol{V}_s^{m+1,\text{yee}} \\ 2\mathbf{D}\boldsymbol{V}_s^{m} \end{bmatrix}. \tag{B.13}$$

If the left-hand side matrix can be inverted, the output SS variable $\boldsymbol{I}_s^{m+1/2}$ is obtained.

B.4 Evaluation Points $m+1/2$ and $m+1/2$

B.4.1 With the TR Method

The SS scheme is discretized as

$$\begin{aligned} \frac{\boldsymbol{X}^{m+1} - \boldsymbol{X}^{m}}{\Delta t} &= \mathbf{A}\frac{\boldsymbol{X}^{m+1} + \boldsymbol{X}^{m}}{2} + \mathbf{B}\frac{\boldsymbol{V}_s^{m+1} + \boldsymbol{V}_s^{m}}{2}, \\ \boldsymbol{I}_s^{m+\frac{1}{2}} &= \mathbf{C}\frac{\boldsymbol{X}^{m+1} + \boldsymbol{X}^{m}}{2} + \mathbf{D}\frac{\boldsymbol{V}_s^{m+1} + \boldsymbol{V}_s^{m}}{2}. \end{aligned} \tag{B.14}$$

This can be simplified to

$$\begin{aligned} \left(\frac{\mathbb{I}_{n_x}}{\Delta t} - \frac{\mathbf{A}}{2}\right)\boldsymbol{X}^{m+1} - \frac{\mathcal{C}}{4}\mathbf{B}\boldsymbol{\alpha}_{C,s}\boldsymbol{I}_s^{m+\frac{1}{2}} &= \left(\frac{\mathbb{I}_{n_x}}{\Delta t} + \frac{\mathbf{A}}{2}\right)\boldsymbol{X}^{m} + \frac{1}{2}\mathbf{B}\boldsymbol{V}_s^{m} + \frac{1}{2}\mathbf{B}\boldsymbol{V}_s^{m+1,\text{yee}}, \\ \left(\mathbb{I}_2 - \frac{\mathcal{C}}{4}\mathbf{D}\boldsymbol{\alpha}_{C,s}\right)\boldsymbol{I}_s^{m+\frac{1}{2}} - \frac{1}{2}\mathbf{C}\boldsymbol{X}^{m+1} &= \frac{1}{2}\mathbf{C}\boldsymbol{X}^{m} + \frac{1}{2}\mathbf{D}\boldsymbol{V}_s^{m} + \frac{1}{2}\mathbf{D}\boldsymbol{V}_s^{m+1,\text{yee}}. \end{aligned} \tag{B.15}$$

Collecting the SS variables $\boldsymbol{X}_s^{m+1}$ and $\boldsymbol{I}_s^{m+1/2}$ in one vector, we can construct the following block matrix system

$$\begin{bmatrix} \frac{\mathbb{I}_{n_x}}{\Delta t} - \frac{\mathbf{A}}{2} & -\frac{\mathcal{C}}{4}\mathbf{B}\boldsymbol{\alpha}_{C,s} \\ -\frac{1}{2}\mathbf{C} & \mathbb{I}_2 - \frac{\mathcal{C}}{4}\mathbf{D}\boldsymbol{\alpha}_{C,s} \end{bmatrix} \begin{bmatrix} \boldsymbol{X}_s^{m+1} \\ \boldsymbol{I}_s^{m+\frac{1}{2}} \end{bmatrix} = \begin{bmatrix} \frac{\mathbb{I}_{n_x}}{\Delta t} + \frac{\mathbf{A}}{2} & \\ \frac{1}{2}\mathbf{C} & -\mathbb{I}_2 \end{bmatrix} \begin{bmatrix} \boldsymbol{X}_s^{m} \\ \boldsymbol{I}_s^{m-\frac{1}{2}} \end{bmatrix} + \begin{bmatrix} \frac{1}{2}\mathbf{B}\boldsymbol{V}_s^{m} + \frac{1}{2}\mathbf{B}\boldsymbol{V}_s^{m+1,\text{yee}} \\ \frac{1}{2}\mathbf{D}\boldsymbol{V}_s^{m} + \frac{1}{2}\mathbf{D}\boldsymbol{V}_s^{m+1,\text{yee}} \end{bmatrix}. \tag{B.16}$$

If the left-hand side matrix can be inverted, the output SS variable $\boldsymbol{I}_s^{m+1/2}$ is obtained.

B.4.2 With the BE Method

The SS scheme is discretized as

$$\begin{aligned} \frac{\boldsymbol{X}^{m+1/2}-\boldsymbol{X}^{m-\frac{1}{2}}}{\Delta t} &= \mathbf{A}\boldsymbol{X}^{m+1/2}+\mathbf{B}\frac{\boldsymbol{V}_s^{m+1}+\boldsymbol{V}_s^{m}}{2}\,, \\ \boldsymbol{I}_s^{m+\frac{1}{2}} &= \mathbf{C}\boldsymbol{X}^{m+1/2}+\mathbf{D}\frac{\boldsymbol{V}_s^{m+1}+\boldsymbol{V}_s^{m}}{2}\,. \end{aligned} \tag{B.17}$$

This can be simplified to

$$\begin{aligned} \left(\frac{\mathbb{I}_{n_x}}{\Delta t}-\mathbf{A}\right)\boldsymbol{X}^{m+1/2}-\frac{\mathcal{C}}{4}\mathbf{B}\boldsymbol{\alpha}_{C,s}\boldsymbol{I}_s^{m+\frac{1}{2}} &= \frac{1}{\Delta t}\boldsymbol{X}^{m-\frac{1}{2}}+\frac{1}{2}\mathbf{B}\boldsymbol{V}_s^{m}+\frac{1}{2}\mathbf{B}\boldsymbol{V}_s^{m+1,\mathrm{yee}}\,, \\ \mathbb{I}_2-\frac{\mathcal{C}}{4}\mathbf{D}\boldsymbol{\alpha}_{C,s}\boldsymbol{I}_s^{m+\frac{1}{2}}-\mathbf{C}\boldsymbol{X}^{m+\frac{1}{2}} &= \frac{1}{2}\mathbf{D}\boldsymbol{V}_s^{m}+\frac{1}{2}\mathbf{D}\boldsymbol{V}_s^{m+1,\mathrm{yee}}\,. \end{aligned} \tag{B.18}$$

Collecting the SS variables $\boldsymbol{X}_s^{m+1/2}$ and $\boldsymbol{I}_s^{m+1/2}$ in one vector, we can construct the following block matrix system

$$\begin{bmatrix} \frac{\mathbb{I}_{n_x}}{\Delta t}-\mathbf{A} & -\frac{\mathcal{C}}{4}\mathbf{B}\boldsymbol{\alpha}_{C,s} \\ -\mathbf{C} & \mathbb{I}_2-\frac{\mathcal{C}}{4}\mathbf{D}\boldsymbol{\alpha}_{C,s} \end{bmatrix}\begin{bmatrix} \boldsymbol{X}_s^{m+\frac{1}{2}} \\ \boldsymbol{I}_s^{m+\frac{1}{2}} \end{bmatrix} = \begin{bmatrix} \frac{\mathbb{I}_{n_x}}{\Delta t} & \\ & \end{bmatrix}\begin{bmatrix} \boldsymbol{X}_s^{m-\frac{1}{2}} \\ \boldsymbol{I}_s^{m-\frac{1}{2}} \end{bmatrix}+\begin{bmatrix} \frac{1}{2}\mathbf{B}\boldsymbol{V}_s^{m}+\frac{1}{2}\mathbf{B}\boldsymbol{V}_s^{m+1,\mathrm{yee}} \\ \frac{1}{2}\mathbf{D}\boldsymbol{V}_s^{m}+\frac{1}{2}\mathbf{D}\boldsymbol{V}_s^{m+1,\mathrm{yee}} \end{bmatrix}. \tag{B.19}$$

If the left-hand side matrix can be inverted, the output SS variable $\boldsymbol{I}_s^{m+1/2}$ is obtained.

Appendix C

Passivity Proof for Inactive VCCSs

The modular approach of Zhang, Bekmambetova and Triverio provides a way to formally prove the stability of the combined scheme when the VCCSs do not feed into the computational domain [40]. The left, central and right transmission lines represent passive subsystems and are denoted TL1, TL2 and TL3, respectively. When the BE method is chosen, the SS scheme, simply denoted as SS, is also a passive subsystem. By reciprocity, we may choose the hanging variables of these systems on integer locations instead of half-integer locations:

$$\begin{aligned} u_{1,A}^m &= V_0 \\ u_{1,P}^m &= u_{2,P}^m = u_{\mathrm{SS},P}^m = V_P \\ u_{1,Q}^m &= u_{2,Q}^m = u_{\mathrm{SS},Q}^m = V_Q \\ u_{3,C}^m &= V_N \end{aligned} \tag{C.1}$$

Using the notation defined in [40, App. A], we similarly construct the interconnection of our subsystems in Figure C.1. The proof can be extended to include the SS system. The supply rate of the total system is

$$s\left(\mathbf{y}^{m-\frac{1}{2}}, \mathbf{u}^m\right) = s_{1,A}\left(y_{1,A}^{m-\frac{1}{2}}, u_{1,A}^m\right) + s_{3,C}\left(y_{2,C}^{m-\frac{1}{2}}, u_{2,C}^m\right). \tag{C.2}$$

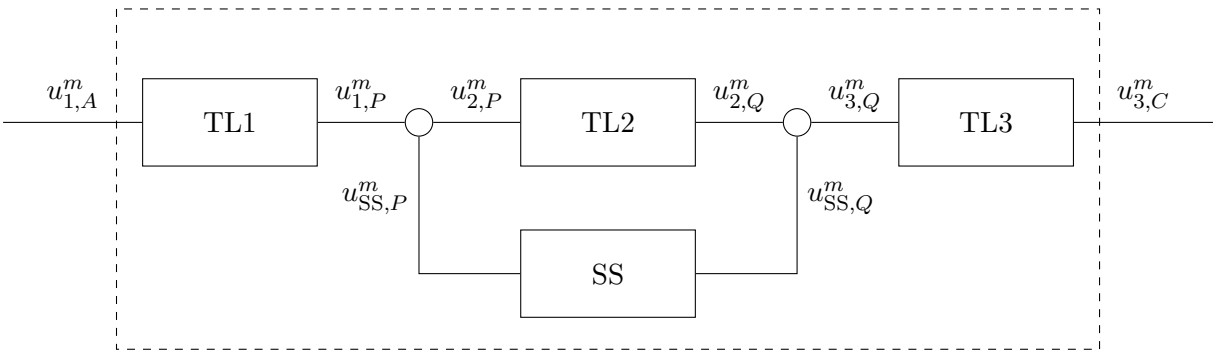

Figure C.1: The interconnection of different subsystems.

The storage function of the total system is the sum of the storage functions of the subsystems, including the one for the SS system. Addition of the dissipation inequalities of each subsystem yields:

$$\begin{aligned}
&\mathcal{E}\left(\mathbf{x}^{n+1}\right) - \mathcal{E}\left(\mathbf{x}^{n}\right) \leq s_1\left(\mathbf{y}_1^{m-\frac{1}{2}}, \mathbf{u}_1^m\right) + s_2\left(\mathbf{y}_2^{m-\frac{1}{2}}, \mathbf{u}_2^m\right) + s_3\left(\mathbf{y}_3^{m-\frac{1}{2}}, \mathbf{u}_3^m\right) + s_{\mathrm{SS}}\left(\mathbf{y}_{\mathrm{SS}}^{m-\frac{1}{2}}, \mathbf{u}_{\mathrm{SS}}^m\right) \\
&= s_{1,A}\left(y_{1,A}^{m-\frac{1}{2}}, u_{1,A}^m\right) + s_{3,C}\left(y_{3,C}^{m-\frac{1}{2}}, u_{3,C}^m\right) + \underbrace{s_{1,P}\left(y_{1,P}^{m-\frac{1}{2}}, u_{1,P}^m\right) + s_{2,P}\left(y_{2,P}^{m-\frac{1}{2}}, u_{2,P}^m\right)}_{0} \\
&+ \underbrace{s_{2,Q}\left(y_{2,Q}^{m-\frac{1}{2}}, u_{2,Q}^m\right) + s_{3,Q}\left(y_{3,Q}^{m-\frac{1}{2}}, u_{3,Q}^m\right)}_{0} + s_{\mathrm{SS},P}\left(y_{\mathrm{SS},P}^{m-\frac{1}{2}}, u_{\mathrm{SS},P}^m\right) + s_{\mathrm{SS},Q}\left(y_{\mathrm{SS},Q}^{m-\frac{1}{2}}, u_{\mathrm{SS},Q}^m\right),
\end{aligned} \tag{C.3}$$

where the FDTD-like supply-rates result in the cancellation of four terms. The dissipation inequality of the total system is retrieved if

$$s_{\mathrm{SS},P}\left(y_{\mathrm{SS},P}^{m-\frac{1}{2}}, u_{\mathrm{SS},P}^m\right) + s_{\mathrm{SS},Q}\left(y_{\mathrm{SS},Q}^{m-\frac{1}{2}}, u_{\mathrm{SS},Q}^m\right) = 0\,. \tag{C.4}$$

If we observe that the SS scheme has all its discrete eigenvalues inside the unit disk, the system is stable. As a consequence it is also passive, such that (C.4) is true.

Bibliography

[1] *Semiconductor Market Size, Share & COVID-19 Impact Analysis, By Components (Memory Devices, Logic Devices, Analog IC, MPU, Discrete Power Devices, MCU, Sensors and Others), By Application (Networking & Communications, Data Processing, Industrial, Consumer Electronics, Automotive, Government) and Regional Forecast, 2021-2028.* Accessed on June 2021, [Online], Available: `www.fortunebusinessinsights.com/semiconductor-market-102365`. 2021.

[2] Martijn Huynen. "A 3-D Differential Surface Admittance Operator for the Broadband Modeling of Lossy Conductors". PhD thesis. Ghent University, 2019, p. 180.

[3] G. Antonini, A. Orlandi, and C.R. Paul. "Internal impedance of conductors of rectangular cross section". In: *IEEE Transactions on Microwave Theory and Techniques* 47.7 (1999), pp. 979–985. DOI: `10.1109/22.775429`.

[4] E.K. Miller A.J. Poggio. "Integral Equation Solutions of Three-dimensional Scattering Problems". In: (1973). Chap. 4, R. Mittra, ed., Pergamon Press, Oxford.

[5] Beghein, Yves and Cools, Kristof and De Zutter, Daniël. "A higher order space-time Galerkin discretization for the time domain PMCHWT equation". eng. In: *Proceedings of the 29th Annual Review of Progress in Applied Computational Electromagnetics*. Monterey, California, USA: Applied Computational Electromagnetics Society (ACES), 2013, 274–279.

[6] P. C. Wang and M. S. Tong. "Transient analysis for electromagnetic scattering by dielectric objects based on PMCHWT equations". In: *2016 Progress in Electromagnetic Research Symposium (PIERS)*. 2016, pp. 3204–3207. DOI: `10.1109/PIERS.2016.7735259`.

[7] Wouter Tierens and Daniël De Zutter. "An unconditionally stable time-domain discretization on cartesian meshes for the simulation of nonuniform magnetized cold plasma". In: *Journal of Computational Physics* 231.15 (2012), pp. 5144–5156. ISSN: 10902716. DOI: `10.1016/j.jcp.2012.04.028`. URL: `http://dx.doi.org/10.1016/j.jcp.2012.04.028`.

[8] Arne Van Londersele. "Novel Finite-Difference Time-Domain Techniques to Model Multiscale Electromagnetic Problems". PhD thesis. Ghent University, 2018, p. 194.

[9] Arne Van Londersele, Daniël De Zutter, and Dries Vande Ginste. "A New Hybrid Implicit–Explicit FDTD Method for Local Subgridding in Multiscale 2-D TE Scattering Problems". In: *IEEE Transactions on Antennas and Propagation* 64.8 (2016), pp. 3509–3520. DOI: 10.1109/TAP.2016.2576477.

[10] A.C. Cangellaris and Li Zhao. "Rapid FDTD simulation without time stepping". In: *IEEE Microwave and Guided Wave Letters* 9.1 (1999), pp. 4–6. DOI: 10.1109/75.752106.

[11] B. Denecker et al. "Generation of FDTD subcell equations by means of reduced order modeling". In: *IEEE Transactions on Antennas and Propagation* 51.8 (2003), pp. 1806–1817. DOI: 10.1109/TSP.2003.815439.

[12] L. Kulas and M. Mrozowski. "Reduced order models of refined Yee's cells". In: *IEEE Microwave and Wireless Components Letters* 13.4 (2003), pp. 164–166. DOI: 10.1109/LMWC.2003.811068.

[13] Daniël De Zutter and Luc Knockaert. "Skin effect modeling based on a differential surface admittance operator". In: *IEEE Transactions on Microwave Theory and Techniques* 53.8 (2005), pp. 2526–2538. DOI: 10.1109/TMTT.2005.852766.

[14] Constantine A. Balanis. *Advanced engineering electromagnetics*. 2nd ed. John Wiley & Sons, 2012.

[15] A. E. H. Love. "The integration of the equations of propagation of electric waves". In: Roy. Soc. Lond., 1901, 68:19–21.

[16] Enrica Martini, Giacomo Carli, and Stefano Maci. "An Equivalence Theorem Based on the Use of Electric Currents Radiating in Free Space". In: *IEEE Antennas and Wireless Propagation Letters* 7 (2008), pp. 421–424. DOI: 10.1109/LAWP.2008.2001764.

[17] R. F. Harrington. *Time Harmonic Electromagnetics*. Electrical and Electronic Engineering Series. New York: Mc- Graw-Hill, 1961.

[18] I. V. Lindell. *Methods for Electromagnetic Field Analysis*. Oxford Engineering Science Series. Oxford: Clarendon Press, 1992.

[19] S.R. Rengarajan and Y. Rahmat-Samii. "The field equivalence principle: illustration of the establishment of the non-intuitive null fields". In: *IEEE Antennas and Propagation Magazine* 42.4 (2000), pp. 122–128. DOI: 10.1109/74.868058.

[20] A. Glisson. "An integral equation for electromagnetic scattering from homogeneous dielectric bodies". In: *IEEE Transactions on Antennas and Propagation* 32.2 (1984), pp. 173–175. DOI: 10.1109/TAP.1984.1143279.

[21] A. Rubio Bretones, R. Mittra, and R. Gómez Martín. "A Hybrid Technique Combining the Method of Moments in the Time Domain and FDTD". In: *IEEE Microwave and Guided Wave Letters* 8.8 (1998), pp. 281–283. ISSN: 10518207. DOI: 10.1109/75.704414.

[22] Hendrik Rogier, Frank Olyslager, and Daniël De Zutter. "A New Hybrid FDTD-BIE Approach to Model Electromagnetic Scattering Problems". In: *IEEE Microwave and Guided Wave Letters* 8.3 (1998), pp. 138–140. ISSN: 10518207. DOI: 10.1109/75.661141.

[23] C. R. Paul. *Analysis of Multiconductor Transmission Lines, 2E (Wiley Series in Microwave Optical Engineering)*. 2nd ed. Wiley Series in Microwave Optical Engineering. Wiley-IEEE Press, 2007.

[24] Zheng Xu and Jian-Qiang Lu. "Three-Dimensional Coaxial Through-Silicon-Via (TSV) Design". In: *IEEE Electron Device Letters* 33.10 (2012), pp. 1441–1443. DOI: 10.1109/LED.2012.2207703.

[25] N Nahman and D Holt. "Transient analysis of coaxial cables using the skin effect approximation A+ B$\sqrt{\{s\}}$". In: *IEEE Transactions on Circuit Theory* 19.5 (1972), pp. 443–451.

[26] Kane Yee. "Numerical solution of initial boundary value problems involving Maxwell's equations in isotropic media". In: *IEEE Transactions on Antennas and Propagation* 14.3 (1966), pp. 302–307. DOI: 10.1109/TAP.1966.1138693.

[27] Susan C. Hagness Allen Taflove. *Computational Electrodynamics: The Finite-Difference Time-Domain Method, Third Edition*. 3rd ed. Artech House, Inc., 2005.

[28] Stephen Gedney. *Introduction to the Finite-Difference Time-Domain (FDTD) Method for Electromagnetics*. 2011.

[29] K.L. Shlager and J.B. Schneider. "Comparison of the dispersion properties of higher order FDTD schemes and equivalent-sized MRTD schemes". In: *IEEE Transactions on Antennas and Propagation* 52.4 (2004), pp. 1095–1104. DOI: 10.1109/TAP.2004.825811.

[30] K. Chamberlin and L. Gordon. "Modeling good conductors using the finite-difference, time-domain technique". In: *IEEE Transactions on Electromagnetic Compatibility* 37.2 (1995), pp. 210–216. DOI: 10.1109/15.385885.

[31] R. Courant, K. Friedrichs, and H. Lewy. "On the Partial Difference Equations of Mathematical Physics". In: *IBM Journal of Research and Development* 11.2 (1967), pp. 215–234. DOI: 10.1147/rd.112.0215.

[32] M.S. Min and C.H. Teng. "The Instability of the Yee Scheme for the "Magic Time Step"". In: *Journal of Computational Physics* 166.2 (2001), pp. 418–424. ISSN: 0021-9991. DOI: https://doi.org/10.1006/jcph.2000.6650.

[33] B. Gustavsen and A. Semlyen. "Rational approximation of frequency domain responses by vector fitting". In: *IEEE Transactions on Power Delivery* 14.3 (1999), pp. 1052–1061. DOI: 10.1109/61.772353.

[34] B. Gustavsen. "Improving the pole relocating properties of vector fitting". In: *IEEE Transactions on Power Delivery* 21.3 (2006), pp. 1587–1592. DOI: 10.1109/TPWRD.2005.860281.

[35] Dirk Deschrijver et al. "Macromodeling of Multiport Systems Using a Fast Implementation of the Vector Fitting Method". In: *IEEE Microwave and Wireless Components Letters* 18.6 (2008), pp. 383–385. DOI: 10.1109/LMWC.2008.922585.

[36] Adam Semlyen and Bjørn Gustavsen. "A Half-Size Singularity Test Matrix for Fast and Reliable Passivity Assessment of Rational Models". In: *IEEE Transactions on Power Delivery* 24.1 (2009), pp. 345–351. DOI: 10.1109/TPWRD.2008.923406.

[37] Bjørn Gustavsen. "Fast Passivity Enforcement for Pole-Residue Models by Perturbation of Residue Matrix Eigenvalues". In: *IEEE Transactions on Power Delivery* 23.4 (2008), pp. 2278–2285. DOI: 10.1109/TPWRD.2008.919027.

[38] Stefano Grivet-Talocia and Bjørn Gustavsen. *Passive Macromodeling: Theory and Applications*. Jan. 2016. DOI: 10.1002/9781119140931.

[39] Piero Triverio et al. "Stability, Causality, and Passivity in Electrical Interconnect Models". In: *IEEE Transactions on Advanced Packaging* 30.4 (2007), pp. 795–808. DOI: 10.1109/TADVP.2007.901567.

[40] Xinyue Zhang, Fadime Bekmambetova, and Piero Triverio. "A Stable FDTD Method With Embedded Reduced-Order Models". In: *IEEE Transactions on Antennas and Propagation* 66.2 (2018), pp. 827–837. DOI: 10.1109/TAP.2017.2784414.

[41] L. Kulas and M. Mrozowski. "Stability of the FDTD scheme containing macromodels". In: *IEEE Microwave and Wireless Components Letters* 14.10 (2004), pp. 484–486. DOI: 10.1109/LMWC.2004.834572.

[42] J. C. Butcher. "Numerical Methods for Differential Equations and Applications". In: John Wiley Sons, Ltd, 2008.

[43] Luebbers R.J Kunz K.S. *The Finite Difference Time Domain Method for Electromagnetism*. CRC-Press, 1993.

[44] Ryan A. Chilton and Robert Lee. "The discrete origin of FETD-Newmark late time instability, and a correction scheme". In: *Journal of Computational Physics* 224.2 (2007), pp. 1293–1306. ISSN: 0021-9991. DOI: https://doi.org/10.1016/j.jcp.2006.11.021. URL: https://www.sciencedirect.com/science/article/pii/S0021999106005870.

[45] Sandra Costanzo et al. "Benzocyclobutene as Substrate Material for Planar Millimeter-Wave Structures: Dielectric Characterization and Application". In: *Journal of infrared, millimeter and terahertz waves* 31 (Jan. 2010), pp. 66–77. DOI: 10.1007/s10762-009-9552-0.

[46] Etienne Perret et al. "Complex permittivity characterization of benzocyclobutene for terahertz applications". In: *Microelectronic Engineering* 85 (Nov. 2008), pp. 2276–2281. DOI: 10.1016/j.mee.2008.07.008.

[47] Shumin Wang and F.L. Teixeira. "Some remarks on the stability of time-domain electromagnetic simulations". In: *IEEE Transactions on Antennas and Propagation* 52.3 (2004), pp. 895–898. DOI: 10.1109/TAP.2004.825486.

[48] Shumin Wang. "Improved-accuracy algorithms for time-domain finite methods in electromagnetics". PhD thesis. 2003. URL: http://rave.ohiolink.edu/etdc/view?acc_num=osu1061225243.

[49] K. Chemmangat et al. "Scalable models of microwave system responses using sequential sampling on unstructured grids". In: *International Journal of Numerical Modelling-electronic Networks Devices and Fields* 27 (2014), pp. 122–137.

[50] Piero Triverio. *Vector Fitting*. 2019. arXiv: 1908.08977 [physics.comp-ph].

[51] J. Crank and P. Nicolson. "A practical method for numerical evaluation of solutions of partial differential equations of the heat-conduction type". In: *Mathematical Proceedings of the Cambridge Philosophical Society* 43.1 (1947), 50–67. DOI: 10.1017/S0305004100023197.

[52] D. Britz, O. østerby, and J. Strutwolf. "Damping of Crank–Nicolson error oscillations". In: *Computational Biology and Chemistry* 27.3 (2003). Computers and Chemistry, pp. 253–263. ISSN: 1476-9271. DOI: https://doi.org/10.1016/S0097-8485(02)00075-X. URL: https://www.sciencedirect.com/science/article/pii/S009784850200075X.

[53] Murat Arcak and Eduardo Sontag. "Diagonal stability of a class of cyclic systems and its connection with the secant criterion". In: *Automatica* 42 (Sept. 2006), pp. 1531–1537. DOI: 10.1016/j.automatica.2006.04.009.

[54] Komal Sable and Manodipan Sahoo. "Electrical and Thermal Analysis of Cu-CNT Composite TSV and GNR Interconnects". In: *2020 International Symposium on Devices, Circuits and Systems (ISDCS)*. 2020, pp. 1–6. DOI: 10.1109/ISDCS49393.2020.9262991.

[55] Boris Vaisband et al. "Electrical and Thermal Models of CNT TSV and Graphite Interface". In: *IEEE Transactions on Electron Devices* 65.5 (2018), pp. 1880–1886. DOI: 10.1109/TED.2018.2812761.